SPECTROSCOPY STUDIES OF HOST-GUEST INTERACTIONS IN COORDINATION NETWORKS AND SUPRAMOLECULAR COMPOUNDS

By

Yuan Chen

A dissertation submitted to the

Graduate School-Newark

Rutgers, the State University of New Jersey

In partial fulfillment of the requirements

For the degree of

Doctor of Philosophy

Graduate Program in Chemistry

Written under the direction of

Professor Jenny Lockard

And approved by

_____

_____

_____

_____

Newark, New Jersey

October, 2015

ABSTRACT OF THE DISSERTATION

SPECTROSCOPY STUDIES OF HOST-GUEST INTERACTION IN COORDINATION NETWORKS AND SUPRAMOLECULAR COMPOUNDS

by YUAN CHEN

Dissertation Director:

Dr. Jenny Lockard

After decades of development, host-guest chemistry has become a highly multidisplinary field, spanning areas of chemistry to material science. The construction of host molecules and materials for housing specific guest species often involves a complicated combination of subtle electronic and structural interactions. The number of interacting sites and type of non-covalent forces that are involved in the host-guest interaction determine the stability of a complex. Thus, a comprehensive understanding of the binding behavior and structure-property relationship is as crucial as the design and synthesis of host materials. Conventional characterization methods of crystalline solid state materials such as single crystal XRD are key but have their limitations. In this case, accurate and structurally sensitive characterization methods are highly demanded.

In this dissertation, Raman and X-ray absorption spectroscopy techniques are employed to complement conventional characterization methods, FT-IR, UV and XRD, to help identify the structural change and host-guest interactions on various systems in their solid form, including metal-organic frameworks and macrocycle complexes. The results of these investigations revealed unique information to help understand host-guest interactions in these systems and may help the further improvement of their applications.

Chapter 1: An overview of the research background is introduced. The overview will start from a general introduction of host-guest systems, followed by a summary of methods used for probing the structural changes and host-guest interactions. Detailed descriptions of the specific classes of these systems are covered in the remaining part of the chapter, namely metal-organic frameworks and cucurbit[n]uril.

Chapter 2: A flexible metal organic framework (MOF) comprised of Co(II) ions and 4,4'-oxybis(benzoic acid) linkers undergoes substantial structure rearrangements upon removal of the metal coordinated water molecules upon activation. Two complementary structurally sensitive methods, X-ray absorption and Raman spectroscopy, are used to build a composite picture of the MOF activation process by revealing the specific local structural changes about both the Co sites and the organic linkers that are not apparent through standard powder X-ray diffraction studies.

Chapter 3: The activation and CO_2 gas adsorption processes in the *rht*-type metal-organic framework, $[Cu_3(TDPAT)(H_2O)_3]\cdot 10H_2O\cdot 5DMA$ (TDPAT=2,4,6-tris(3,5-dicarboxylphenylamino)-1,3,5-triazine) were investigated on the molecular level using several spectroscopic characterization methods. The remarkable selectivity of this

framework for CO_2 is attributed to the high density of coordinatively unsaturated metal nodes and amine linker functionality that both serve as gas binding sites. Spectroscopic evidence for these binding interactions as well as the concomitant electronic and molecular level structural changes of the host framework and CO_2 guest is derived from a combination of *in situ* UV-vis diffuse reflectance, X-ray absorption and Raman spectroscopy studies. Results showed that the activation process produced subtle structural rearrangements of the framework that may be influencing the binding interactions upon subsequent CO_2 adsorption.

Chapter 4: The activation and CO_2 gas adsorption processes of a series of MOFs, M_2(dobdc) (M=Mg, Co, Ni, Zn; dobdc= 2,5-dihydroxy-benzene dicarboxylic acid), were studied *in-situ* by Raman spectroscopy and diffuse reflectance spectroscopy. The high density of open metal sites lining the pore wall internal surfaces gives extraordinary gas storage capacity and selectivity to these frameworks, especially under low pressure. The fact that a considerable capacity gap exists among these iso-structural frameworks remains puzzling. In this chapter, a careful examination of *in-situ* Raman and diffuse reflectance spectra reveals that other than the well known factor of binding affinity, the unique local and global structure change that each framework experiences upon activation (ie removal of labile metal-bound solvent molecules) may have a significant impact on the gas adsorption properties as well.

Chapter 5: A complex formed between cucurbit[7]uril (CB7) and ferrocene (Fc) is investigated in the solid state using Raman spectroscopy. The Raman spectra are compared with those of the CB7 host and Fc guest reference molecules, revealing

significant frequency shifts of some vibrational modes upon complexation. These changes expose the structural and electronic interactions between the host and guest components and provide evidence that the ferrocene moiety resides within the cucurbituril cavity in the solid state environment.

Dedicated to my family

For your selfless love

ACKNOWLEDGEMENT

I would like to extend my sincerest gratitude to my advisor, professor Lockard, for her conscientious support and encouragement. Her guidance was a great treasure in the past five years and will be more valuable in the future.

I would like to thank the members of my committee, Professor Li, Professor Galoppini and Professor Piotrowiak for their precious advice and great patience during my study.

I would like to thank my collaborators, Professor Galoppini, Professor Li, as well as their students: Agnieszka Klimczak, Jingming Zhang and Hao Wang. Without them, most parts of my dissertation would not be done.

I would like to thank all the Chemistry Department faculty members, especially Professor Lalancette, Professor Husky, Professor Pavanello, Professor Mendelsohn, Professor He and Professor Pietrangelo, I bothered them so many times which more than I can count.

I would like to thank my fellow doctoral students and postdoctorals, most of whom helped me here and there, now and then. And more important, all of you make me feel that I'm not alone during my life in Rutgers.

I would like to thank all the staff members who made all the efforts so I can sail through my daily work and life.

You are all great people.

Chapter 2 of this dissertation is a version of the manuscript as it appears in *J. Phys. Chem. C*, 2013, **117**, 20068-20077. Copyright 2013 American Chemistry Society.

Chapter 3 of this dissertation is reproduced from *J. Mater. Chem. A*, 2015, **3**, 4945-4953 with the permission from the Royal Society of Chemistry.

Chapter 5 of this dissertation is reproduced from *RSC Adv.*, 2013, **3**, 1354-1358 with permission from the Royal Society of Chemistry.

TABLE OF CONTENTS

LIST OF ABBREATIONS

MOF	Metal-Organic Framework
CB[n]	Cucurbit[n]uril
Fc	Ferrocene
TDPAT	2,4,6-tris(3,5-dicarboxylphenylamino)-1,3,5-triazine
H_2oba	4,4’-oxybis(benzoic acid)
dobdc	2,5-dioxido-1,4-benzenedicarboxylate
XRD	X-ray diffraction
XAS	X-ray absorption
XANES	X-ray absorption near edge structure
EXAFS	extended X-ray absorption fine structure
UV-vis	Ultraviolet-Visible
DR	Diffuse reflectance
FT-IR/ATR	Fourier transform infrared spectroscopy/ Attenuated total reflectance
TGA	Thermogravimetric analysis
DC	Direct current
RT	Room Temperature

LIST OF TABLES

LIST OF FIGURES

Chapter 1. Introduction

Host-guest chemistry in porous materials and supramolecular compounds is the core concept behind their functionality for adsorption-based applications or molecular encapsulation. It is generally considered as the interactions between a larger molecule or molecular framework with sizeable cavity or porous framework (host) and a smaller molecule or ion (guest) to produce a larger complex or impregnated material. The main driving force of this interaction is not covalent bonds but weaker forces, such as, hydrogen bonding, π-π interaction, or van der Waals forces. [1]

Host-guest interactions play a central role in numerous areas of biology, chemistry and physics, from complicated enzyme and DNA systems [2] of life to selective sensing, [3] catalysis, [4, 5] and even advanced concept of molecular information storage [6, 7] and molecular machine. [8] The unique structure-property relationship brought by the intermolecular interactions has greatly extended the horizon of chemistry and lead to countless potential applications. The self-assembly reactions and the resulting properties of these host-guest systems are determined by the binding forces, binding sites and structure. Thus, identifying the binding sites and the way they are interacting is crucial in understanding the behavior of host-guest systems, and may also lead to rational design of new materials. There are various mature techniques, including FT-IR, UV/Vis, NMR and X-ray diffraction that can help researchers to understand the electronic and structural ramifications of these interactions. Under some circumstances, these conventional techniques alone fail to reveal important information about the host-guest interaction as described below. In this dissertation, Raman and X-ray absorption spectroscopy, along

with the conventional characterization technologies are employed to obtain a more complete view of the interactions in some host-guest complexes.

The main focus of this dissertation is investigating activation-induced structural changes and framework-gas interaction in metal-organic frameworks (MOFs) by spectroscopy methods. Three different MOF-related projects will be introduced from Chapter 2 to Chapter 4. In Chapter 5, we will show that these methods can also be used to study the host-guest interactions involved in supramolecular complexes through the example of a ferrocene-cucurbit[7]uril complex.

1.1 Electronic and Structurally sensitive spectroscopy techniques

While the more conventional characterization methods mentioned above are widely used and provide solid evidence about the structural information and nature of host-guest interaction, each one has its own limitations. SXRD is only applicable when the materials retain their crystallinity after the guest inclusion treatment, and PXRD can only provide very limited information about the binding site. NMR is less applicable in many cases for probing host-guest interactions in solid state materials since solid state NMR usually requires specific sample formats that are less amenable to *in situ* measurements. In terms of IR, the heavily overlapped peaks and relative low resolution of conventional FTIR spectrometers make subtle changes difficult to recognize. Thus, other methods are needed to complement the traditional means of characterization to provide a more complete picture of these host-guest interactions. In this thesis, we specifically employed the following electronic and structurally sensitive spectroscopy techniques to help investigate the molecular level structure changes and host-guest interactions in several MOF systems and a CB[7]-ferrocene inclusion complex: Raman spectroscopy and X-ray absorption spectroscopy.

1.1.1 Raman spectroscopy

Both Raman and IR spectroscopy measure the vibrational modes of a given molecule or material. While IR directly probes the energy difference between two vibrational energy levels by absorbing the light with the same energy, Raman spectroscopy yields this information indirectly by measurement of inelastically scattered light. When the electric field (E) of incident monochromatic laser light interacts with

molecules with polarizability α, the resulting electric dipole moment P = αE deforms the molecules and force them to vibrate at characteristic frequency. As a result, these photons are scattered accompanied by changes of energy (Figure 1.1). If the scattered photons lose energy, the energy difference between the incident photons and scattered photons is called "stokes shift". If the scattered photons gain energy, the energy difference is called "anti-stokes shift". In a simple harmonic approximation, the frequency of a vibration, *v*, is proportional to $\sqrt{\frac{k}{\mu}}$, in which *k* is the force constant and μ is the reduced mass. For a given molecule, *k* is correlated to the equilibrium bond length R_e (Badger's rule), thus the change of Raman frequencies can be used to analyze the structural changes. Blue shift of a Raman mode indicates higher force constant/shorter bond and vice versa. Since the host-guest interactions are strongly affected by the structural features of both components, the molecular level structural information obtained by Raman spectroscopy can help build a clearer structure-property relationship of host-guest systems. Although the vibrational modes are much more complex due to mixing and coupling in larger systems, such as extended networks or supramolecular compounds, qualitative conclusions can still be drawn in our studies. Resonance Raman (RR) occurs when the excitation laser frequency coincides with the energy of a molecule's electronic excited states. Depending on the magnitude of the transition dipole moment associated with the electronic transition, the vibrational coordinates that involve significant excited state displacement can be enhanced by up to 3~5 orders of magnitude. While an intensity analysis can be used to elucidate excited state structure information, [9] RR is employed primarily as a signal enhancing mechanism in this work. Raman spectroscopy and IR are complementary to each other since their activity is determined by selection rules in which vibrational modes

with dipole moment change are IR active and vibrational modes with change of polarizability are Raman active. IR spectroscopy is generally more sensitive than Raman spectroscopy, but Raman has advantages of better resolution. A combination of Raman and IR can complement each other to generate a complete picture of the vibrational state of a given material.

Raman spectroscopy has become a crucial characterization method for many types of materials, [10-12] and also starts to show its value in MOF studies. [13, 14] Most of the reported studies however focus on using Raman to probe the existence of guest species. In our work, particularly on the MOF systems, more subtle changes of the framework itself along with the guest species are investigated to reveal the structural changes associated with guest binding interactions.

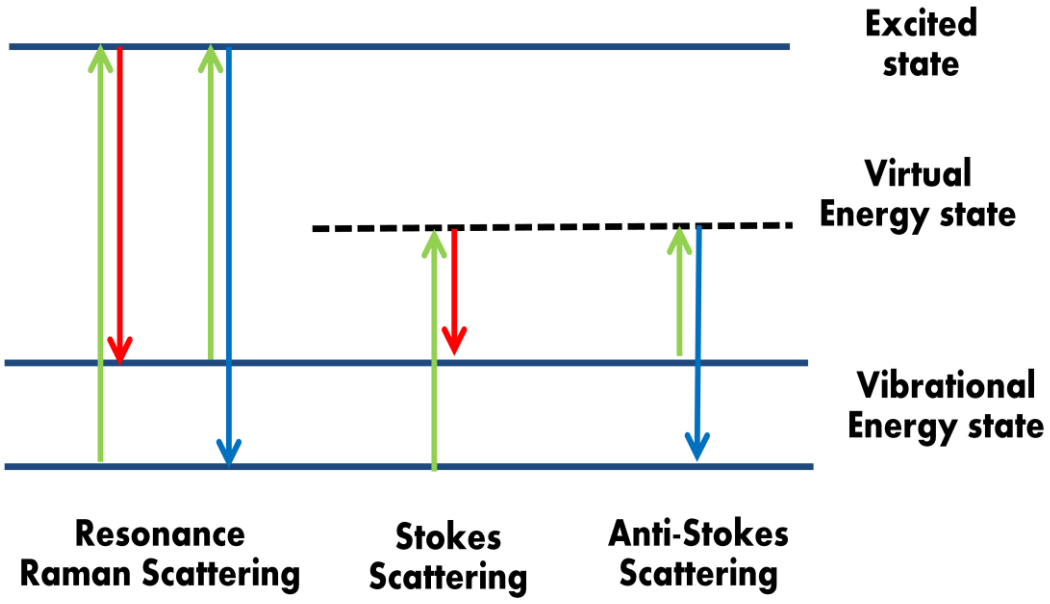

Figure 1.1 Illustration of Raman Scattering.

1.1.2 X-ray absorption spectroscopy

X-ray absorption occurs when the X-ray photon is absorbed by the core electron of an atom (Figure 1.2). [15] Since the core electrons have distinguishable core-level binding energy in different elements, X-ray absorption spectroscopy (XAS) is an element specific technology. A XAS spectrum usually contains two parts, the X-ray absorption near edge spectrum (XANES) and extended X-ray absorption fine structure (EXAFS). Each part reveals different type of information: The XANES region contains information on the absorbing element oxidation state and coordination geometry. EXAFS is the result of interference between the photo-electron and back scattered electrons from the neighboring atoms, thus, it can be used to determine the distance, type and number of surrounding atoms by fitting the following equation:

$$\chi(k) = \sum_j \frac{N_j f_j(k) e^{-2k^2\sigma_j^2}}{kR_j^2} \sin\left[2kR_j + \delta_j(k)\right]$$

Where $f(k)$ and $\delta(k)$ are scattering properties of the atoms neighboring the excited atom, N is the number of neighboring atoms, R is the distance to the neighboring atom, and σ^2 is the disorder in the neighbor distance. From the equation, N, R and σ^2 can be determined by the scattering amplitude $f(k)$ and phase-shift $\delta(k)$, which comes from the experimental data. Analysis of both parts provides a convenient way to obtain the local atomic environment information, especially when the information cannot be obtained through XRD characterization. XAS has shown to be an important characteristic technique in metalloproteins, mixed oxides, ternary and quaternary semiconductor solid solutions. [16] Recently, XAS has gradually attracted attention in the studies of structural

information in MOF materials and some pioneer works have been reported [17-20]. In chapter 2 and 3, we will extend the application of XAS to more systems and show the advantages and limitations of XAS in MOF research.

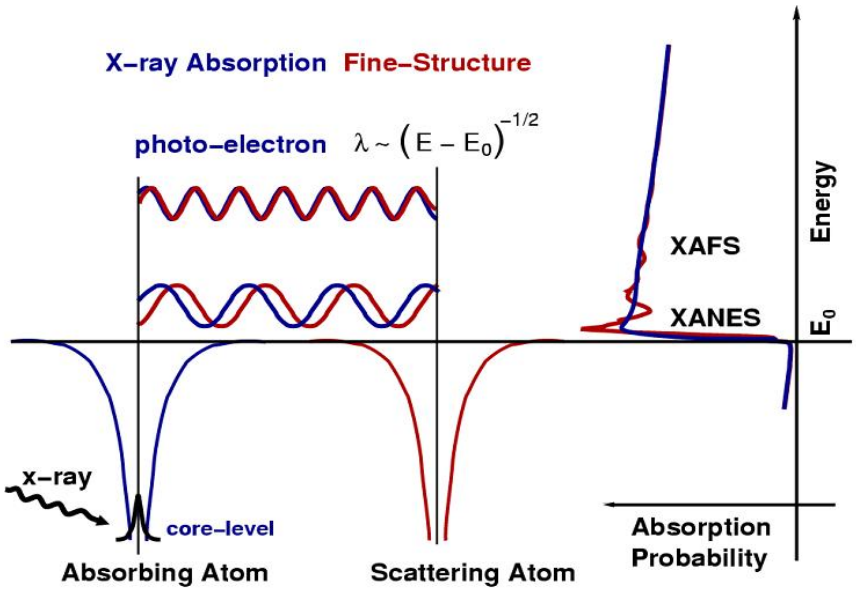

Figure 1.2 Illustration of X-ray absorption process. Reprinted with permission from *Fundamental of XAFS*, University of Chicago, Chicago. Copy right 2004, Matthew Newville.

1.2 Metal-Organic Frameworks

The majority of this thesis will focus on the spectroscopic studies of host-guest interactions in Metal-Organic Framework (MOF) materials. MOFs are comprised of metal ions and organic linkers that self assemble through coordination bonds to form crystalline materials. Due to the strong coordination bonds, many MOFs have a robust framework that can retain their structure after the removal of guest molecules. This permanent porosity allows the inclusion of other guest molecules, leading to various adsorption-based functionality and applications.

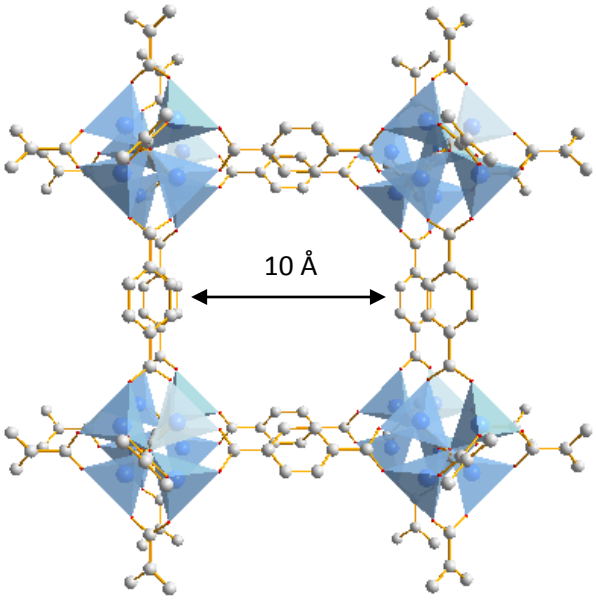

Figure 1.3 MOF-5 framework. Zn4(O) sub units are represented as blue tetrahedrn. Zn (blue), oxygen (red), carbon (grey)

In 1999, Yaghi and coworker reported the first robust and highly porous MOF: MOF-5 (Figure 1.2). [21] With an octahedral zinc(II)oxo metal node and terephthalate linkers, MOF-5 forms a cubic shape framework. MOF-5 achieves a porosity of 61% of

the total volume and a BET surface area of 2320 m^2/g, which is higher than most other porous materials. [22] The same group then used a method called isoreticular expansion to further increase MOF surface areas, leading to the reports of MOF-177 in 2004 [23] and MOF-210 in 2010, [24] with reported surface areas of 3780 m^2/g and 6240 m^2/g, respectively. Isoreticular MOFs (IRMOFs) are great examples to show the tunability of MOF structures. By simply increasing the length of the linker molecule, MOFs with different pore size but same topology can be obtained. Modification of the linker shape or functionality can lead to a tremendous number of structures and functions. More than 20,000 different frameworks have been reported in the past 15 years, and this number is still increasing. The versatile structural and chemical tunability of MOFs has attracted tremendous interest in the past decade due to their potential application in gas storage [25-27] and separation [28-32], catalysis [33-35] and sensing. [36-38] In the following sections, we will discuss these features in detail.

1.2.1 Structure Features

The functionality of frameworks is crucial for optimization of the host-guest interaction. In this section, we describe some important pore surface properties, including the pore shape and shape, open metal sites and functional groups.

1.2.1.1 Pore size and shape

The shape and size of pores in MOFs play important roles when considering their use in catalysis and gas adsorption applications. The high surface area of MOF materials allows efficient packing of small guest molecules in the pores. For non-polar gases, like hydrogen and nitrogen, the functionality of organic linkers is not the driving force for

encapsulation. The most import factor is the pore size and surface area. The mechanism is similar in the case of methane storage. The capacity of methane storage is proportional to the pore volume of a MOF material. In the ultra low density MOF-210, [24] the uptake can reach up to 476 mg/g at 80 bar, which is almost twice as much as the capacity in a high pressure gas cylinder under the same pressure.

The molecular sieving effect caused by the pore size and shape is also crucial for the separation of molecules. MOFs with small pore apertures can block larger guest molecules, but allow the adsorption of the smaller ones. Ma and coworkers reported the selective adsorption of H_2 over N_2 in PCN-13 [39] and PCN-17. [40] In MIL-96, the selective adsorption of CO_2 over CH_4 is also observed based on this sieving effect. [41] Both separations are important industrial processes for purification of natural gas or H_2 for fuel cell applications.

The variety of pore sizes and shapes also offer advantages when considering MOFs as catalytic hosts. The frameworks with larger pore openings allow much easier diffusion of incoming reactants or outgoing products. [42] Rational design of specific structures give MOFs the ability to fill the gap between zeolite materials and mesoporous supports [34], since the zeolites usually have limited cavity size for many reactants and mesoporous silicates have too large void space to retain the confinement effects.

1.2.1.2 Functionalization of internal surface

Although the pore size and shape determines what guest molecules can access the inside of MOFs, the chemical properties of the internal pore surface are more important when specific host-guest interactions are responsible for selective adsorption behavior.

The interaction can be related to polarity, quadrupole moment and H-bonding depending on the chemical functionality of the pore surface. [2]

One MOF application that commonly exploits differences in guest molecule binding is selective gas absorption. The green house gas generated from fossil fuel combustion has become one of the most important environmental challenges we are facing. Effective separation and storage of CO_2 from the emitted gas is an urgent problem waiting to be solved. The post-combustion flue gas from fossil-fuel power station is a mixture of N_2, water vapor, CO_2, NO_x and SO_x. All these emitted gases have very similar molecular diameters, which makes them difficult to separate by size effect. The separation has to rely on creating an internal environment which has different affinity to each component in the flue gas. Compared to the main component N_2, CO_2 has significantly higher polarizability (CO_2, 26.3×10^{-25} cm^{-3} versus N_2, 17.6×10^{-25} cm^{-3}) and quadrupole moment (CO_2, 13.4×10^{-40} $C \bullet m^2$; N_2, 4.7×10^{-40} $C \bullet m^2$). [29] Modification of the pore surface to a more polar environment can greatly enhance the selectivity of CO_2 over N_2.

There are two typical strategies to enhance CO_2 capture performance, including polarizing organic functionalization and/or incorporating open metal sites in the frameworks. As part of the first approach, nitrogen or oxygen containing basic groups have been widely adopted for improving CO_2 adsorption. The dispersion and electrostatic forces resulting from the interaction of the quadrupole moment of CO_2 with dipoles of heteroatom creates higher affinity between CO_2 and the decorated pore surface. An amine functionalized MOF-5 adsorbs 10% CO_2 under ambient pressure with 20% less surface

area. [43] The same enhancement has been shown in many other MOFs functionalized with strongly polarizing groups MOFs compared to their parent materials. [44-46]

The other well studied strategy for enhancing MOF CO_2 adsorption is the use of open metal sites in the frameworks. In some MOFs, one or more coordination site of the metal center is not coordinated to the linker but to rather labile solvent molecules. An open site can be created by removal of coordinated solvent molecule under vacuum and elevated temperature. The CO_2 capacity of a MOF with high density of open metal sites will be much higher than conventional CO_2 adsorption materials. [39] M/DOBDC, a family of frameworks consist of various metal ions and 2,5-dioxido-1,4-benzenedicarboxylate linker, represents some of the best performing MOFs utilizing open metal site. The binding sites rich pore environment of M/DOBDC frameworks gives them a high CO_2 capacity which can reach up to 26 wt % under atmospheric pressure. [47]

In another work, Ryotaro *et al* reported selective adsorption of one non-polar gas, acetylene over another, carbon dioxide based on H-bonding between C_2H_2 and non-coordinated oxygen from the linker. [27] These examples showed how the chemical tunability of MOFs provides numerous possibilities for designing new functional materials.

1.2.1.3 Framework flexibility

While most MOFs are stable, rigid structures, there are flexible MOFs that can respond to pressure, temperature or/and guest molecules.[48-56] Since considerable flexibility can be hardly found in other porous hosts materials, this unique potential feature of MOFs can be exploited for many applications. In one of the most intensively

studied flexible framework series, called MIL-53, comprised of terephthalate linkers and metal nodes such as Al^{3+} or Fe^{3+}, [49] the structure can switch between narrow and wide pore form in response of temperature or guest changes. In MIL-53, the hydrated form is slightly distorted due to the hydrogen-bonding between guest H_2O molecules and the oxygen atoms from the carboxylate groups and axial coordinated hydroxyl groups. The structure can expand upon H_2O removal and or temperature change, a phenomenon is called framework "breathing". The MIL-53 family shows dramatically different breathing behavior for different metal centers, whereas the Cr^{3+} version change between an orthorhombic large pore and a monoclinic narrow pore, while the dehydrated Fe^{3+} version has a *C2/c* symmetry. Consequently, the frameworks show different guest adsorption behavior due to the pore size differences. [50] Another interesting feature of flexible MOFs is the "gate opening" effect. A good example is the MOF reported by Joobeom Seo and coworkers in 2009, [51] in which the pore is blocked by long hydroxyethoxy groups on the linker. The linker can be pushed to rotate by increasing pressure and reveal the pore for guest inclusion.

The host-guest interactions in these systems are fairly complicated since their structure become less well-defined due to the rearrangement of framework. So far, the rearrangement mechanism is not completely clear because the single crystal studies are usually limited to the as-synthesized form while the guest removed MOFs commonly lose some degree of their long range order. More in-depth studies are still needed.

1.2.2 Characterization of MOFs

The most informative way to obtain structural information on MOFs is single crystal XRD. The structure of the frameworks can be refined from the diffraction data if a single crystal of the framework is obtained. Some recent studies on the activation and gas adsorption in MOF materials [57-59] have shown that XRD is an extremely valuable tool for the determination of MOF structures. SXRD studies however are not always possible due to the often times non-trivial work of growing good quality single crystals. Moreover, when single crystals are obtained, they can easily loose long range order during further treatment (such as thermal activation process). The disorder of guest molecules can also significantly affect the quality of refinement. Powder X-ray diffraction (PXRD) gives valuable but more indirect information about the crystal lattice parameters with fewer sample requirements. In the study of gas adsorption in MIL-53 Cr, the flexible framework exhibits a breathing behavior with a significant change in the unit cell which is monitored by in-situ PXRD. [60] The shift of low angle peaks indicates an expansion of the pore dimension from the evacuated form to the guest included form.

IR spectroscopy also plays an important role in the study of MOF materials since it can provide valuable information about the vibrational energy changes that can be associated with host-guest interactions. For example, IR can be used to identify the binding site of CO_2 in MOFs, when CO_2 is adsorbed on a open metal site by a M^{n+} – O=C=O adduct, the IR active asymmetric stretching (ν_3, 2349 cm^{-1}) and bending (ν_2, 667 cm^{-1}) modes of CO_2 are expected to change due the electron donating nature of this interaction and break of the CO_2 symmetry. The shift of both modes has been proven as an effective indicator of CO_2 binding in multiple studies. [13, 32, 59, 61, 62] While the CO_2 is

interacting with the functional groups attached to the internal surface, IR is sensitive enough to distinguish the strong zwitterionic carbamates type of interaction, [45] electron donor-acceptor complex [63] and polarization effect [64] between the functional groups and CO_2.

1.3 Host-guest complex based on Cucurbit[n]uril

1.3.1 Cucurbituril Homologues: Structures and Properties

The final chapter of this thesis involves a spectroscopic investigation of the host-guest interactions behind the formation of a supramolecular complex based on Cucurbit[*n*]urils (CB[*n*]), which constitute a family of macrocyclic compounds in which *n* glycoluril units are linked by methylene bridges (Figure 1.1). The first member of these compounds was discovered by Behrend et al in 1905 [65], but the chemical composition was not identified until 1981, [10] when Mock and coworkers determined the structure of a CB[6] calcium bisulfate complex by X-ray diffraction. In 2000, the other members of the CB[n] family were isolated and identified by Kim and coworkers [11]. Since then, the CB[n] series has joined the ranks of other heavily researched host molecules, such as crown ethers, [68] cyclodextrins [69] and calixarenes.[70]

As shown in Figure 1.1, CB[n] has a hydrophobic cavity that is surrounded by a rim of polar carbonyl groups. The carbonyl groups at the portals of CB[n]s provide binding sites for charge-dipole interaction and hydrogen bonding, as well as a coordination site for metal ions. Beside these similarities, the distinguishable differences in the cavity and portal sizes give them abilities to recognize various guest molecules [71]. Smaller members like CB[6] tend to form stable complexes with small species like ammonium

ions, while CB[7] can encapsulate bigger guests, such as ferrocene, adamantanamine or methyl viologen dication (MV^{2+}) in a 1:1 ratio. CB[n] with more than seven glycoluril units can even encapsulate more than 2 molecules. For example, 2, 6-dihydroxynathphalene (HN) can form a 1:1:1 charge-transfer (CT) complex with MV^{2+} and CB[8]. This CT interaction between HN and MV^{2+} is largely enhanced in CB[8] due to the close contact in the cavity of CB[8] [72].

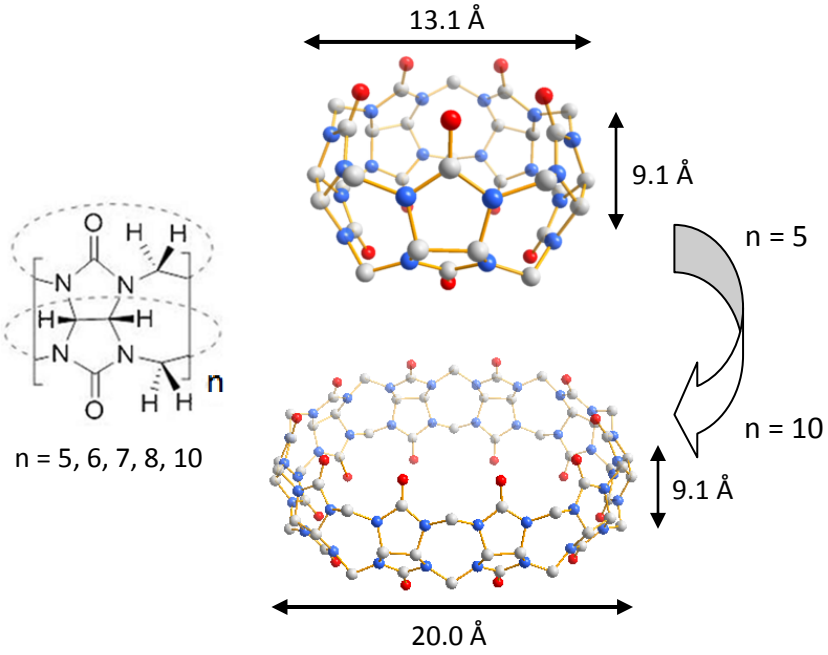

Figure 1.4 Structures of CB[n]. The atoms are carbon (gray), nitrogen (blue) and oxygen (red)

The unique features of each CB[n] host offer various potential applications. Because of the ability to stabilize two different guest molecules in certain orientations, some reactions can occur in larger CB[n] hosts with high stereoselectivity. [73-75] Kim and some other groups also reported several examples of molecular machines and switches

based on CB[6] and CB[8] complexes. [76, 77] Recently, some studies show that CB[n] can form stable charge transfer complexes with dye molecules and anchor them on nano metal oxides or quantum dots. [78-80] These devices may lead to improvement of light harvesting ability to help design better photo-voltaic devices.

1.3.2 Characterization of Cucurbit[n]uril

Single crystal X-ray diffraction (XRD) and nuclear magnetic resonance (NMR) spectroscopy are the two most commonly used characteristion methods in CB[n] studies. The first accurate crystal structure obtained for this class of supramolecular systems was that of a CB[6]-calcium complex isolated and characterized by Mock *et al*. [10] Over a decade later, the remaining homologues of CB[n] (n = 5,7,8 and 10) and some associated complex were reported by Kim [67] and Isaacs [81]. ^{1}H NMR is especially useful to distinguish the homologues of CB[n]. The protons on the methylene groups have distinctive chemical shifts that increase progressively with more glycoluril units while the methylene and methane carbons down shift. Furthermore, the encapsulated species and their reaction products can also be readily identified from the chemical shift, relative intensities and spin-spin couplings. [73]

Another frequently used technique is infrared spectroscopy which probes the vibrational energy levels associated with the bonding interactions in molecules and materials. The existence of peaks at characteristic frequencies can help identify the interacting species and the frequency shift of characteristic peaks reveals the changes of bond strength and polarization. Thus, IR is a widely used tool when probing the encapsulation of guest molecules in host molecules such as CB[n]s, as well as the interaction of CB[n]s to other materials. [67, 82, 83]

While most of the characterizations of CB[n] inclusion complexes are conducted in solution form or by single crystals, practical applications will most likely require solid state material or immobilized material on solid surfaces. [71] In these cases, the characterization methods are limited, especially if the complexes are not in single crystal form. Other techniques are required to analyze the structural changes and host-guest interaction of inclusion complexes in non-crystalline solid state formats. This will be the focus of the Raman spectroscopy studies described in Chapter 5.

1.4 Reference

1 E. P. Kyba, R. C. Helgeson, K. Madan, G. W. Gokel, T. L. Tarnowski, S. S. Moore, D. J. Cram, *J. Am. Chem. Soc*., 1977, **99(8)**, 2564-2571

2 J. W. Steed, J. L. Atwood, *Supramolecular Chemistry*, John Wiley & Sons, Inc, 2th edition, 2009

3 D. Astruc, E. Boisselier, C. Ornelas, *Chem. Rev.*, 2010, **110**, 1857-1959

4 M. Raynal, P. Ballester, A. Vidal-Ferran, P. W. N. M. van Leeuwen, *Chem. Soc. Rev.*, 2014, **43**, 1660-1733

5 M. Raynal, P. Ballester, A. Vidal-Ferran, P. W. N. M. van Leeuwen, *Chem. Soc. Rev.*, 2014, **43**, 1734-1787

6 J. -M. Lehn, *Angew. Chem. Int. Ed.*, 1990, **29**, 1304-1319

7 J. -M. Lehn, *Chem. Soc. Rev.*, 2007, **36**, 151-160

8 V. Balzani, A. Credi, F. M. Raymo, F. Stoddart, *Angew. Chem. Int. Ed*., 2000, **39**, 3348-3391

9 D. H. Volman, G. S. Hammond, D. C. Neckers, J. I. Zink, K.-S. Kim Shin, *Adv. Photochem.*, 2007, **16**, 119-214

10 L. M. Malard, M. A. Pimenta, G. Dresselhaus, M. S. Dresselhaus, *Phys. Rep.*, 2009, **473**, 51-87

11 P. R. Carey, *J. Bio. Chem.*, 1999, **274**, 26625-26628

12 Z. Movasaghi, S. Rehman, I. U. Rehman, *Appl. Spectrosco. Rev.*, 2007, **42**, 493–541

13/70 N. Nijem, P. Thissen, Y. Yao, R. C. Longo, K. Roodenko, H. Wu, Y. Zhao, K. Cho, J. Li, D. C.Langreth, Y. J. Chabal, *J. Am. Chem. Soc*., 2011, **133**, 12849–12857

14 L. Valenzano, J. G. Vitillo, S. Chavan, B. Civalleri, F. Bonino, S. Bordiga, C. Lamberti, *Catal. Today*, 2012, **182**, 67-79

15 M. Newville, *Rev. Mineral. Geochem.*, 2014, **78**, 33-74

16 S. Bordiga, F. Bonino, k. P. Lillerud, C. Lamberti, *Chem. Soc. Rev.*, 2010, **39**, 4885–4927

17 G. de Combarieu, S. Hamelet, F. Millange, M. Morcrete, J.-M. Tarascon, G. Férey, R. I. Walton, *Electrochem. Commun.*, 2009, **11**, 1881-1884

18 S. Chavan, F. Bonino, J. G. Vitillo, E. Groppo, C. Lamberti, P. D. C. Dietzel, A. Zecchina, S. Bordiga, *Phys.Chem.Chem.Phys.*, 2009, **11**, 9811–9822

19 F. Bonino, S. Chavan, J. G. Vitillo, E. Groppo, G. Agostini, C. Lamberti, P. D. C. Dietzel, C. Prestipino, S. Bordiga, *Chem. Mater.*, 2008, **20**, 4957–4968

20 W. S. Drisdell, R. Poloni, T. M. McDonald, J. R. Long, B. Smit, J. B. Neaton, D. Prendergast, J. B. Kortright, *J. Am. Chem. Soc.*, 2013, **135**, 18183−18190

21 H. Li, M. Eddaoudi, M. O'Keeffe, O. M. Yaghi, *Nature*, 1999, **402**, 276-279

22 H. Furukawa, O. M. Yaghi, *J. Am. Chem. Soc.*, 2009, **131**, 8875-8883

23 H. K. Chae, D. Y. Siberio-Pérez, J. Kim, Y. B. Go, M. Eddaoudi, A. J. Matzger, M. O'Keeffe, O. M. Yaghi, *Nature*, 2004, **427**, 523-527

24 H. Furukawa, N. Ko, Y. B. Go, N. Aratani, S. B. Choi, E. Choi, A. Ö. Yazaydin, R. Q. Snurr, M. O'Keefe, J. Kim, O. M. Yaghi, *Science*, 2010, **329**, 424-428

25 J. L. C. Rowsell, A. R. Millward, K. S. Park, O. M. Yaghi, *J. Am. Chem. Soc.*, 2004, **126**, 5666-5667

26 D. G. Samsonenko, H. Kim, Y. Sun, G. -H. Kim, H. -S. Lee, K. Kim, *Chem. Asian J.*, 2007, **2**, 484 – 488

27 R. Matsuda, R. Kitaura, S. Kitagawa, Y. Kubota, R. V. Belosludov, T. C. Kobayashi, H. Sakamoto, T. Chiba, M. Takata, Y. Kawazoe, Y. Mita, *Nature*, 2005, **436**, 238-241

28 J.R. Li, R. J. Kuppler, H. C. Zhou, *Chem. Soc. Rev.*, 2009, **38**, 1477–1504

29 D. M. D'Alessandro, B. Smit, J. R. Long, *Angew. Chem. Int. Ed.*, 2010, **49**, 6058–6082

30 S. Ma, X. S. Wang, D. Yuan, H. C. Zhou, *Angew. Chem. Int. Ed.*, 2008, **47**, 4130-4133

31 M. Carboni, C. W. Abney, S. Liu, W. Lin, *Chem. Sci.*, 2013, **4**, 2396-2402

32 K. Sumida, D. L. Rogow, J. A. Mason, T. M. McDonald, E. D. Bloch, Z. R. Herm, T. -H. Bae, J. R. Long, *Chem. Rev.*, 2012, **112**, 724–781

33 J. Liu, L. Chen, H. Cui, J. Zhang, L. Zhang, C. -Y. Su, Chem. Soc. Rev.,2014,43, 6011—6061

34 D. Farrusseng, S. Aguado, C. Pinel, *Angew. Chem. Int. Ed.*, 2009, **48**, 7502 – 7513

35 A. Corma, H. García, F. X. Llabrés i Xamena, *Chem. Rev.*, 2010, **110**, 4606–4655

36 X. Zhu, H. Zheng, X. Wei, Z. Lin, L. Guo, B. Qiu, G. Chen., *Chem. Commun.*, 2013, **49**, 1276—1278

37 L. E. Kreno, Kirsty Leong, O. K. Farha, M. Allendorf, R. P. Van Duyne, J. T. Hupp, *Chem. Rev.*, 2012, **112**, 1105–1125

38 L. E. Kreno, K. Leong, O. K. Farha, M. Allendorf, R. P. Van Duyne, J. T. Hupp, *Chem. Rev.*, 2012, **112**, 1105–1125

39 S. Q. Ma, X. S. Wang, C. D. Collier, E. S. Manis and H.-C. Zhou, *Inorg. Chem.*, 2007, **46**, 8499–8501

40 S. Q. Ma, X. S. Wang, D. Q. Yuan and H.-C. Zhou, *Angew. Chem., Int. Ed.*, 2008, **47**, 4130–4133

41 T. Loiseau, L. Lecroq, C. Volkringer, J. Marrot, G. Férey, M. Haouas, F. Taulelle, S. Bourrelly, P. L. Llewellyn, M. Latroche, *J. Am. Chem. Soc.*, 2006, **128**, 10223–10230

42 P. Valvekens, F. Vermoortele, D. De Vos, *Catal. Sci. Technol.*, 2013, **3**, 1435—1445

43 A. R. Millward, O. M. Yaghi, *J. Am. Chem. Soc.*, 2005, **127**, 17998

44 B. Arstad, H. Fjellvag K. O. Kongshaug, O. Swang, R. Blom, *Adsorption*, 2008, **14**, 755-762

45 T. M. McDonald, D. M. D'Alessandro, R. Krishna, J. R. Long, *Chem. Sci.*, 2011, **2**, 2022-2028

46 H. Deng, C. J. Doonan, H. Furukawa, R. B. Ferriera, J. Towne, C. B, Knobler, B. Wang, O. M. Yaghi, *Science*, 2010, **327**, 846-850

47 S. R. Caskey, A. G. Wong-Foy, A. J. Matzger, *J. Am. Chem. Soc.*, 2008, **130**, 10870–10871

48 D. Bradshaw, J. B. Claridge, E. J. Cussen, T. J. Prior, M. J. Rosseinsky, *Acc. Chem. Res.*, 2005, **38**, 273-282

49 C. Serre, F. Millange, C. Thouvenot, M. Nogués, G. Marsolier, D. Louër, Gérard Férey, *J. Am. Chem. Soc.*, 2002, **124**, 13519-13526

50 T. Devic, F. Salles, S. Bourrelly, B. Moulin, G. Maurin, P Horcajada, C. Serre, A. Vimont, J. -C. Lavalley, H. Leclerc, G. Clet, M. Daturi, P. L. Llewellyn, Y. Filinchuk, G. Férey, *J. Mater. Chem.*, 2012, **22**, 10266-10273

51 J. Seo, R. Matsuda, H. Sakamoto, C. Bonneau, S. Kitagawa, *J. Am. Chem. Soc.*, 2009, **131**, 12792–12800

52 B. Chen, C. Liang, J. Yang, D. S. Contreras, Y. L. Clancy, E. B. Lobkovsky, O. M. Yaghi, S. Dai, *Angew. Chem.*, 2006, **118**, 1418 –1421

53 F. Millange, N. Guillou, R. I. Walton, J.-M. Grenèche, I. Margiolaki, G. Férey, *Chem. Commun.*, 2008, 4732–4734

54 C. Gücüyener, J. van den Bergh, J. Gascon, F. Kapteijn, *J. Am. Chem. Soc.*, 2010, **132**, 17704–17706

55 L. Chen, J. P. S. Mowat, D. Fairen-Jimenez, C. A. Morrison, S. P. Thompson, P. A. Wright, T. Düren, *J. Am. Chem. Soc.*, 2013, **135**, 15763−15773

56 D. N. Dybtsev, H. Chun, K. Kim, *Angew. Chem.*, 2004, **116**, 5143 –5146

57 P. D. C. Dietzel, Y. Morita, R. Blom, H. Fjellvåg, *Angew. Chem. Int. Ed.*, 2005, **44**, 6354–6358

58 P. D. C. Dietzel, B. Panella, M. Hirscher, R. Blom, H. Fjellvåg, *Chem. Commun.*, 2006, 959–961

59 P. D. C. Dietzel, R. E. Johnsen, H. Fjellvåg, S. Bordiga, E. Groppo, S. Chavan, R. Blom, *Chem. Commun.*, 2008, 5125–5127

60 C. Serre, S. Bourrelly, A. Vimont, Naseem A. Ramsahye,G. Maurin, P. L. Llewellyn, M. Daturi, Y. Filinchuk, O. Leynaud, P. Barnes, G. Férey, *Adv. Mater.*, 2007, **19**, 2246–2251

61 A. Vimont, J.-M. Goupil, J.-C. Lavalley, M. Daturi, S. Surblé, C. Serre, F. Millange, G. Férey, N. Audebrand, *J. Am. Chem. Soc.*, 2006, **128**, 3218-3227

62 L. Valenzano, B. Civalleri, S. Chavan, G. T. Palomino, C. O. Areán, S. Bordiga, *J. Phys. Chem. C*, 2010, **114**, 11185–11191

63 J. Gascon, U. Aktay, M. D. Hernandez-Alonso, G. P. M. van Klink, F. Kapteijn, *J. of Catal.*, 2009, **261**, 75–87

64 E. Stavitski, E. A. Pidko, S. Couck, T. Remy, E. J. M. Hensen, B. M. Weckhuysen, J. Denayer, J. Gascon, F. Kapteijn, *Langmuir*, 2011, **27**, 3970–3976

65 R. Behrend, E. Meyer, F. Rusche, J. Liebigs, *Ann. Chem.*, 1905, **339**, 1

66 W. A. Freeman, W. L. Mock, N. -Y. Shih, *J. Am. Chem. Soc.*, 1981, **103**, 7367-7368

67 J. Kim, I. -S. Jung, S. -Y. Kim, E. Lee, J. -K. Kang, S. Sakamoto, K. Yamaguchi, K. Kim, *J. Am. Chem. Soc.*, 2000, **122**, 540-541

68 J. S. Bradshaw, R. M. Izatt, *Acc. Chem. Res*.1997, **30**, 338-345

69 G. Crini, *Chem. Rev.*, 2014, **114**, 10940-10975

70 V. Böhmer, *Angew. Chem. Int. Ed*., 1995, **34**, 713-745

71 K. Kim, N. Selvapalam, Y. H. Ko, K. M. Park, D. Kim, J. Kim, *Chem. Soc. Rev.*, 2007, **36**, 267-279

72 J. W. Lee, S. Samal, N. Selvapalam, H. –J. Kim, K. Kim, *Acc. Chem. Res.* 2003, **36**, 621-630

73 S. Y. Jon, Y. H. Ko, S. H. Park, H.-J. Kim, K. Kim, *Chem. Commun.*, 2001, 1938-1939

74 M. Pattabiraman, A. Natarajan, R. Kaliappan, J. T. Mague, V. Ramamurthy, *Chem. Commun.*, 2005, 4542-4544

75 R. Wang, L. Yuan, D. H. Macartney, *J. Org. Chem.*, 2006, **71**,1237

76 W. S. Jeon, A. Y. Ziganshina, J. W. Lee, Y. H. Ko, J.-K. Kang, C. Lee and K. Kim, *Angew. Chem,. Int. Ed.*, 2003, **42**, 4097-4100.

77 K. Moon, J. Grindstaff, D. Sobransingh, A. E. Kaifer, *Angew. Chem., Int. Ed.*, 2004, **43**, 5496-5499

78 M. Freitag, E. Galoppini, *Langmuir*, 2010, **26(11)**, 8262-8269

79 L. Yuan, D. H. Macartney, *J. Phys. Chem. B*, 2007, 111, 6949-6954

80 M. L. Roldán, S. Sanchez-Cortes, J. V. García-Ramos, C. Domingo, *Phys. Chem. Chem. Phys.*, 2012, **14**, 4935–4941

81 S. Liu, P. Y. Zavalij, and L. Isaacs, *J. Am. Chem. Soc.*, 2005, **127**, 16798-16799

82 F. Benyettou, K. Nchimi-Nono, M. Jouiad, Y. Lalatonne, I. Milosevic, L. Motte, J. -C. Olsen, N. Saleh, A. Trabolsi, *Chem. Eur. J.*, 2015, 21, 4607-4613

83 S. Angelos, Y. -W. Yang, K. Patel, J. F. Stoddart, J. I. Zink, *Angew. Chem. Int. Ed.*, 2008, **47**, 2222-2226

Chapter 2. Monitoring the activation of a flexible coordination network using structurally sensitive spectroscopy techniques

2.1 Introduction

Open metal sites in the coordination network are advantageous for enabling metal participation in the gas molecule adsorption process or catalytic reactions with substrates contained within the pores. Several strategies have been employed to integrate unsaturated metal sites in porous materials, including the use of porphyrins as linkers in the framework that will subsequently bind metal ions but leave available axial coordination sites on the metal ions in the process.[1-3] Network flexibility is another variable in coordination network design that can influence its selectivity for a specific gas adsorption or catalytic process. The dynamic behavior of several flexible networks has been reported in which the pore shape and size adapts in response to guest inclusion such as gas adsorbates.[4, 5] Similarly, flexible structures that exhibit condensed phase guest-shape response behavior [6-11] have been reported and are suspected to play an important role in selective catalytic processes.

Coordination networks having both dynamic flexibility and available metal sites for adsorbed guest molecule interactions are particularly intriguing for optimizing the structure/function properties of these materials. In most networks reported with these properties, [12-15] the network metal sites are exposed through coordinated solvent removal by thermal activation and on account of their inherent flexibility, may be especially amenable to drastic local structure changes while retaining their overall crystallinity. Striking color transformations of the bulk materials are commonly encountered upon

activation, which is usually indicative of a change in metal coordination environment upon solvent removal. Despite these suspected coordination environment changes however, detailed quantitative information regarding the molecular-level structural differences between the solvated and desolvated forms of these frameworks are rarely revealed. This is most likely because material activation, while necessary to remove the coordinated solvent molecules from the networks, often results in partial loss of long-range order, rendering the traditional X-ray diffraction methods of characterization less effective for accurate structural determination. An in-depth understanding of the local structural changes that occur both around the metal and on the linker is vital however, as it may help elucidate the trends observed on the macroscale in terms of gas separation or catalytic activity especially since these adsorption based processes ultimately rely on the host-guest interactions within the activated framework on the molecular level.

To validate our methodology, we explore the local structure changes incurred upon activation of a flexible coordination network exhibiting catalytic behavior in this chapter. The framework is composed of Co(II) ions connected through oxygen bridged bis(benzoic acid) linker molecules to form a 2D layered network as shown in Figure 2.1. [16] $[Co(Hoba)_2(H_2O)_2]$ (H_2oba = 4,4'-oxybis(benzoic acid)), the as-synthesized material, contains two axially coordinated water molecules on each cobalt site that complete a near octahedral geometry. One carboxylic acid group of each ligand is deprotonated and forms bridging carboxylate bonds with two neighboring Co(II) ions. The other carboxylic acid remains protonated, forming hydrogen bonds with the adjacent $Co(Hoba)_2$ layer.

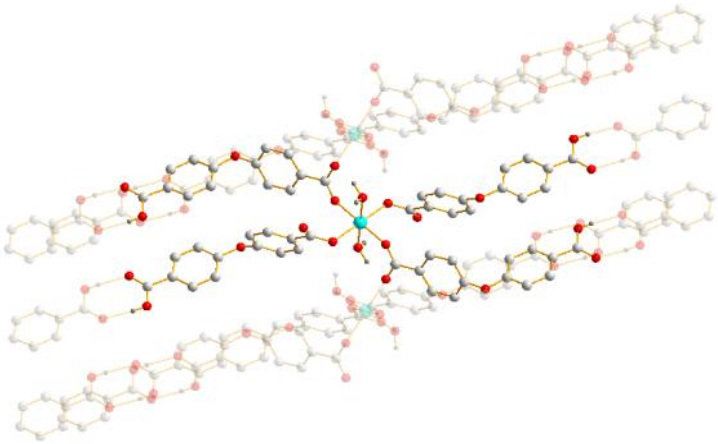

Figure 2.1 Structure of CoHoba. Co (aqua), O (red) C (grey).

TGA measurements of this material indicate a mass loss consistent with the removal of both coordinated water molecules within the activation temperature range of 110 to 160^{o}C, leaving 4-coordinate Co(II) sites. [16] Material activation is accompanied by a distinct color change from pink to blue, suggesting a tetrahedral environment for the 4-coordinate Co sites. When these labile metal bound waters are removed upon activation, open metal sites are potentially made available for subsequent host-guest interaction. In this case, this dehydrated material has been reported to catalyze olefin epoxidation reactions and with 96% conversion, the activated material outperforms the fully solvated material by more than 25% in terms of efficiency.[16] While it is clear from these results that the availability of the metal as Lewis acid sites for participation in the reaction is crucial for efficient performance, a detailed picture of the activated metal site, beyond that which can be inferred from color change alone, along with other coincident local structure changes in the most catalytically active form of the material, may ultimately

help elucidate the reaction mechanism. We illustrate how this information can be attained using multiple structurally sensitive spectroscopic techniques.

In this chapter, X-ray absorption spectroscopy (XAS) is employed along with Raman spectroscopy as complementary structurally sensitive techniques to build a composite picture of the local structure changes of CoHoba upon activation. XAS provides element specific electronic and structural information about the Co sites in this material, with insights on metal coordination geometry and oxidation state revealed through XANES measurements and short range distance information about the Co(II) ions provided by the analysis of the EXAFS region. The utility of this technique for characterizing coordination networks has only recently been recognized with several fundamental studies reporting new structural details on coordination networks and their adsorption processes.[17-22]

Several recent studies combining FTIR and Raman spectroscopy methods provide new structural insights on coordination networks and their adsorption behavior. [12, 23-29] These measurements primarily focused on the higher frequency vibrational modes pertaining to the linkers. In the present study, we use Raman spectroscopy to both support the coordination environment changes about the metal sites derived through EXAFS analysis and reveal the structural changes happening on Hoba linkers further away from the metal centers.

2.2 Results

2.2.1 XRD characterization

The characterization of CoHoba and activated CoHoba by PXRD confirms the retention of crystallinity while indicating long range structure changes that occur upon dehydration. As shown in Figure 2.2, the (00*l*) diffraction peaks shift to lower 2θ angles when the solvent is removed, indicating framework expansion along the crystallographic *c*-axis, i.e. increased separation distance between the layers of carboxylate-bridged Co(II) ions across the hydrogen bonds of the Hoba linker carboxylic acid groups.

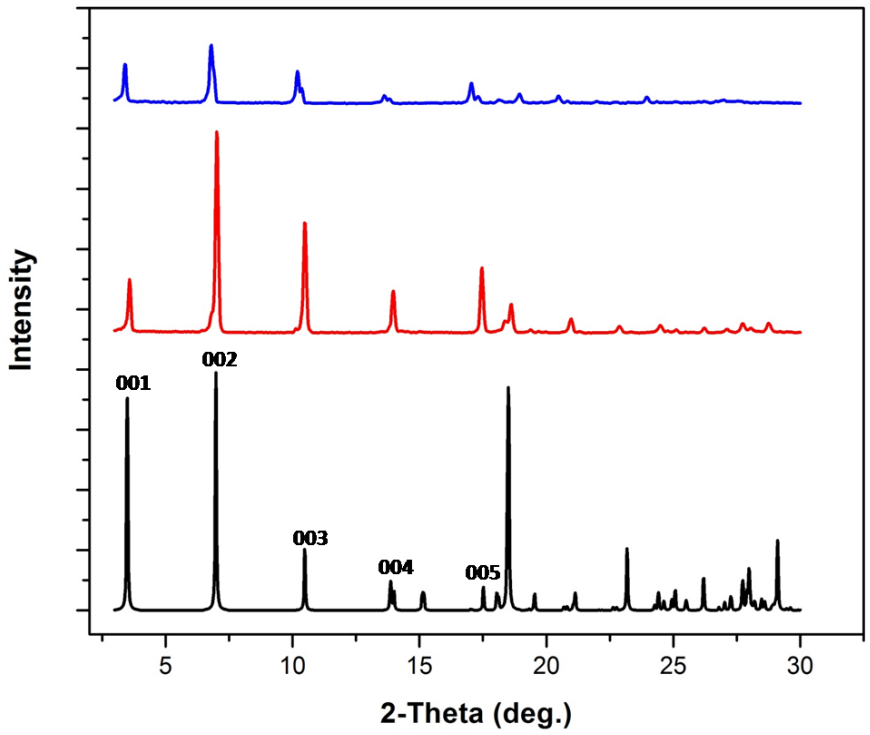

Figure 2.2 The PXRD patterns of the simulated (black), CoHoba (red), and activated CoHoba (blue) samples. The first five (00l) peaks are indicated in the simulated pattern.

2.2.2 X-Ray Absorption Spectroscopy.

The X-ray absorption spectrum of CoHoba was monitored before during and after heat activation of the material. The progression of spectra showing the changes upon heating is shown in Figure 2.3. The two averages of four scans obtained at room temperature, one before and one after activation, were used in the data analysis and fitting. The changes occurring in the XANES region upon activation are shown in Figure 2.4 while the EXAFS data and corresponding fits are presented in Figure 2.5 and 2.7. The parameter values obtained from the best fits are summarized in Tables 2.1 and 2.2. The fitting process is described in the later sections along with an analysis of these data in the context of providing specific structural details about the dehydrated metal sites.

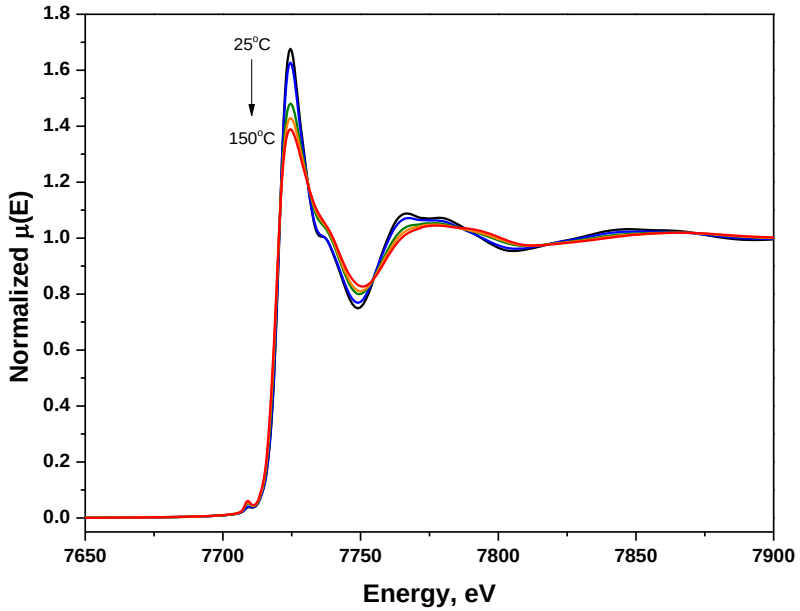

Figure 2.3 The progression of XAS spectra collected in situ upon heating the sample from ~25°C (black trace) to 150°C (red trace).

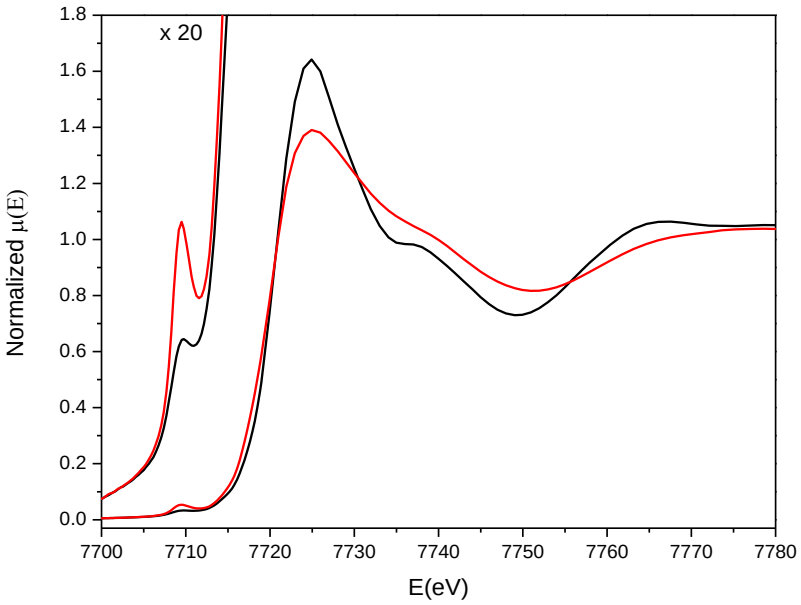

Figure 2.4 Cobalt K-edge XANES spectra of CoHoba (black) and activated CoHoba (red) with highlight of pre-edge feature (× 20 magnification) at 7709.5 eV.

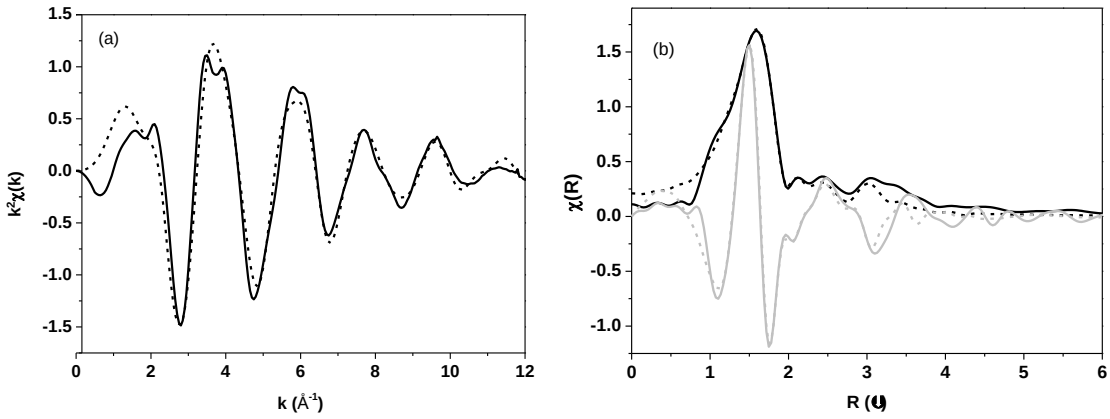

Figure 2.5 Experimental EXAFS spectrum of CoHoba (solid trace) overlaid with theoretical fit (dashed line) obtained using crystal structure model. Data plotted in (a) k and (b) R (magnitude in black and imaginary component in grey).

Table 2.1 Summary of EXAFS fitting parameters and distance information for as-synthesized CoHoba obtained from crystal structure.[a]

Sattering Path[b]	*distances from crystal structure*	R_{eff} *(EXAFS fit)*	*Degeneracy (N)*	σ^2
Co-Ow	2.07	2.06	2	0.007
Co-O2	2.11	2.10	4	0.007
Co-C7	3.10	3.08	4	0.009
Co-C7-O2	3.26	3.23	8	0.009
Co-O7	3.44	3.42	2	0.009
Co-O2-Ow	3.56	3.53	16	0.005
Co-O2-O6	3.56	3.54	8	0.005
Co-C1	3.86	3.83	4	0.008
Co-O7-O6	3.89	3.87	4	0.001
Co-O7-O21	3.91	3.88	4	0.001
Co-O1	3.93	3.91	2	0.003

[a] ΔE_o = -1.67 eV and S_o^2 = 0.87 used for each scattering path. R-factor = 0.006
[b] see Figure 2.6 for atom labeling information

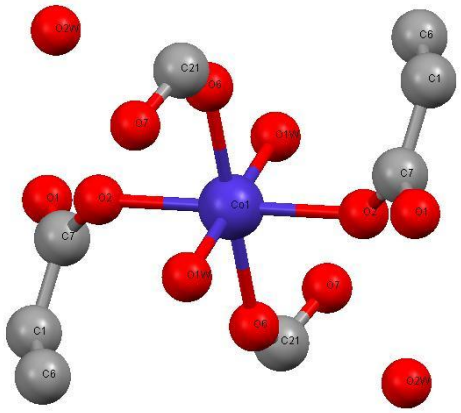

Figure 2.6 Model derived from crystal structure of as-synthesized CoHoba used in EXAFS fitting. Atom labels pertain to scattering paths listed in Table 2.1 with the following equivalencies: O6 = O2, C7 = C21.

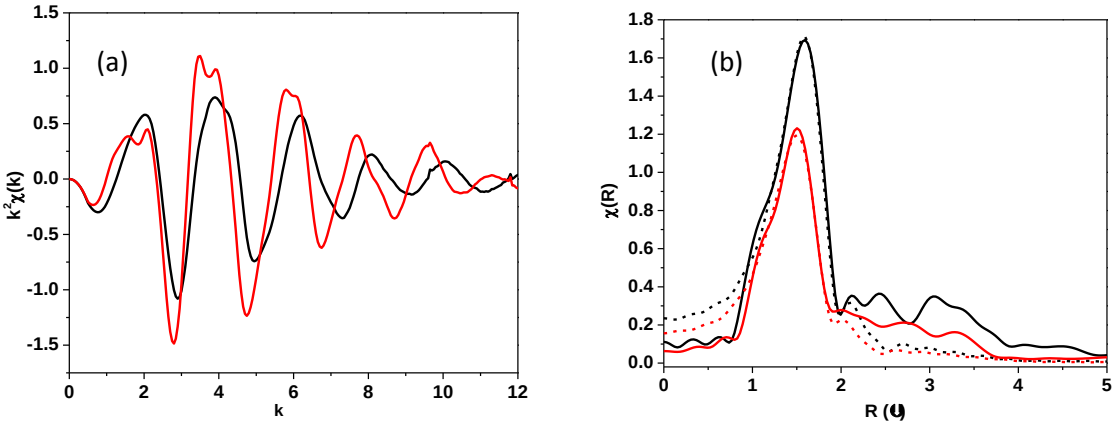

Figure 2.7 Comparison between EXAFS spectra of CoHoba and activated CoHoba in (a) k-space, (b) FT R-space (also includes the theoretical first shell fits) see text for details of fitting.

Table 2.2 Summary of the parameter values obtained from first shell EXAFS fits of CoHoba and activated CoHoba compared with crystal structure data.

Co-O Scattering Path	*N*	S_0^2	ΔE_0	R_{eff}	σ^2	*R-factor*
crystal structure [a]	6	-	-	2.09[b]	-	-
CoHoba	6	1.01	1.53 (1.005)	2.08(0.009)	0.007 (0.001)	0.001
Activated CoHoba	4.2	1.01	1.53	2.01 (0.005)	0.009 (0.001)	0.003

[a] [ref. 45] [b] average Co-O bond distance. Fitting errors shown in parentheses.

2.2.3 Raman spectroscopy

Raman data collected from CoHoba before and after dehydration are shown in Figure 2.8 and the observed vibrational frequencies along with corresponding mode assignments are summarized in Table 2.3. The assignments were made with the aid of both DFT calculations and the Raman measurements of several reference compounds, including CoHoba solvated with D_2O, and the protonated and deprotonated forms of the H_2oba linker alone. These reference spectra can be found in Figure 2.9. A summary of the DFT calculations is provided in Tables 2.4, 2.5 and 2.6.

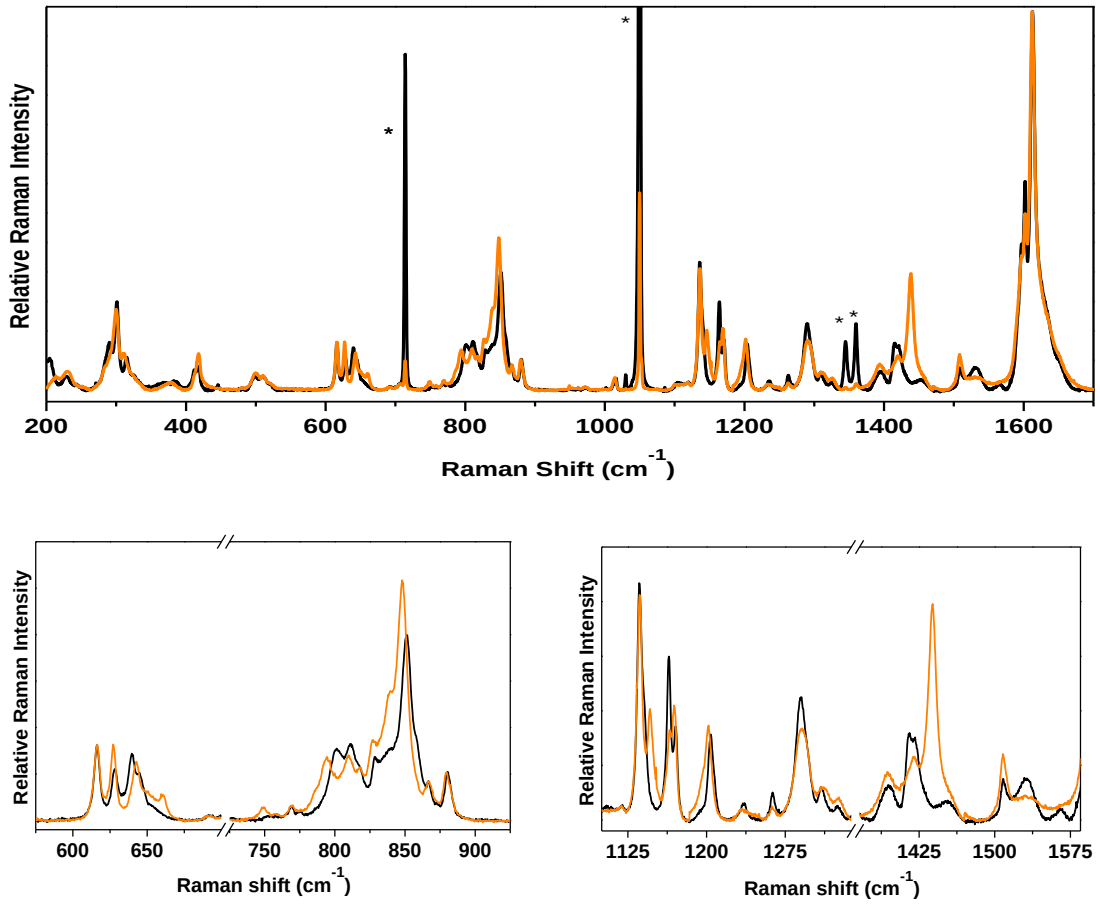

Figure 2.8 Raman spectra of CoHoba (Black) and activated CoHoba (Orange). (Top) Full spectral range, * KNO_3 internal standard peaks. (Bottom) Highlighted low and high frequency regions (see text for detailed analysis).

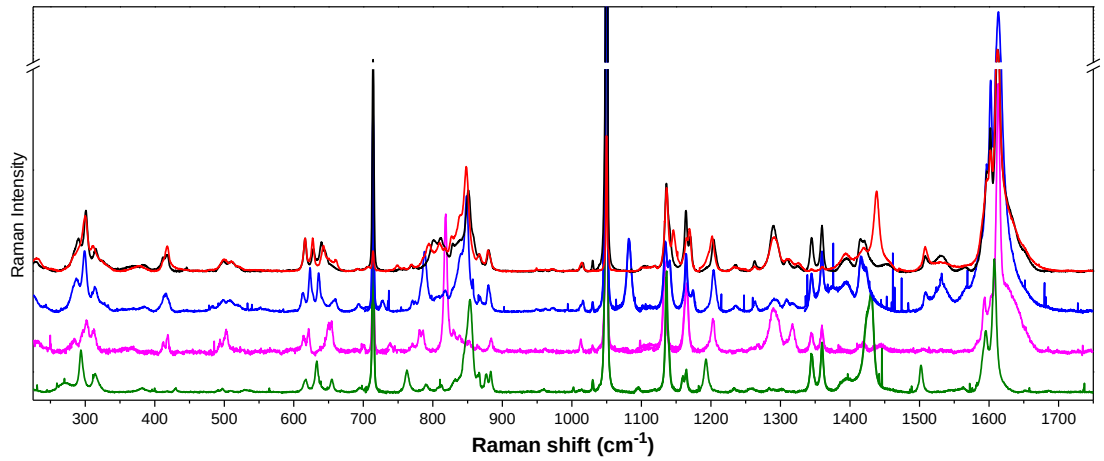

Figure 2.9 Raman spectra of Na_2oba (green), H_2oba (magenta) and D_2O@CoHoba (blue), CoHoba (black) and activated CoHoba (red).

Table 2.3 Observed Raman frequencies and corresponding vibrational mode assignments of CoHoba and activated CoHoba

CoHoba	Activated CoHoba	Vibrational Mode assignment
301	300	Phenyl ring tilt
418	417	δ Phenyl ring
499	499	β ($CC_{Ph}C_{COOH}$) + γ (CH)
616	616	δ Phenyl ring
628	627	δ Phenyl ring
640	643	δ Phenyl ring
645	660	ν (Co-O) linker
801, 811	792, 809	δ Phenyl ring + δ (COC) ether + γ $(CH)_{phenyl}$ + δ(OOH) H-bond
851	847	δ Phenyl ring + β (OCO) carboxylate
1135, ~1141sh	1136, 1146	β (CH)
1170, 1164	1169, 1165	β (CH)
1204	1200	ν_s (CO) ether
1290br	1290br	ν (OOH) H-bond
1416	1436	ν_s (CO) carboxylate
1508	1507	ν_{as} (CO) carboxylate
1532	-	β (HOH) coordinated water
1612	1611	ν $(CC)_{phenyl}$
~1630sh	~1630sh	ν (CO)carboxylic acid

[a] ν - stretching; ν_s - sym. stretching; ν_{as} - asym. stretching; β - in-plane-bending; γ - out-of-plane bending;; δ - deformation; sh – shoulder; br – broad; [b] Description includes dominant contributions to normal vibrational mode only.

Table 2.4 Experimental and calculated Raman active vibrational mode frequencies with descriptions of dominant components of the corresponding vibrational mode assignments for the 4,4'-oxybis(benzoic acid) reference molecule.

Experimental Frequency	Calc. Frequency	Vibrational assignment
303	298	Phenyl ring tilt
419	427	δ Phenyl ring
503	518	β ($CC_{Ph}C_{COOH}$) + γ (CH)
613	602	γ (OH)
621	628	γ (OH) + δ Phenyl ring
653	654	δ Phenyl ring
739	732	β (COC) + γ (CH) + δ Phenyl ring
781	784	β (COC) + δ Phenyl ring
819	828	ν_{sym} (CO) $_{ether}$ + β (COC) + δ Phenyl ring
840 br	846	γ $(CH)_{phenyl}$
1133	1190	β (CH)
1166	1221	β (CH) + γ (OH)
1203	1239	ν_{sym} (CO) $_{ether}$ + β (CH)
1290	-	ν $(H\ldots OH)_{carboxylic\ acid}$
1317	1397	β (OH) + ν_{sym} (C-OH)
1593	1637	ν $(CC)_{phenyl}$
-	1654	ν $(CC)_{phenyl}$
1613	1673	ν $(CC)_{phenyl}$
1635br	1820	ν_{sym} $(C=O)_{carboxylic\ acid}$

ν - stretching; ν_s - sym. stretching; ν_{as} - asym. stretching; β - in-plane-bending; γ - out-of-plane bending;; δ - deformation; sh – shoulder; br - broad

Table 2.5 Experimental and calculated Raman active vibrational mode frequencies with descriptions of dominant components of the corresponding vibrational mode assignments for the 4,4'-oxybis(benzoate) dianion reference molecule.

Experimental Frequency	Calc. Frequency	Vibrational assignment
295	304	Phenyl ring tilt
634	661	δ Phenyl ring
656	-	$\nu(Na^+O^-)^a$
763	761	β(OCO) + γ (CH) + δ Phenyl ring
790	790	β(COC) + γ (OCO) + δ Phenyl ring
853	838	β(OCO) + ν_{sym} $(CO)_{ether}$ + δ Phenyl ring
864sh	844	$\gamma(CH)_{phenyl}$
1136	1126	$\nu(CC)_{carboxylate}$ + β(CH)
1164	1175	β(CH)
1192	1205	ν_{sym} $(CO)_{ether}$ + β(CH)
1429	1364	ν_{sym} $(CO)_{carboxylate}$
1502	-	ν_{asym} $(CO)_{carboxylate}$
1593	1640	$\nu(CC)_{phenyl}$
1606	1653	$\nu(CC)_{phenyl}$

ν - stretching; ν_s - sym. stretching; ν_{as} - asym. stretching; β - in-plane-bending; γ - out-of-plane bending;; δ - deformation; sh – shoulder; br - broad

[a]Experimental data only; Na^+ counter ions most likely situated near oxygens of carboxylate groups

Table 2.6 Calculated Raman active vibrational mode frequencies with descriptions of dominant components of the corresponding vibrational mode assignments for the model system with coordination of Hoba to the Co metal.

Calc. Frequency	Vibrational assignment
320	Phenyl ring tilt
405	Phenyl ring tilt
426	δ Phenyl ring
490	δ Phenyl ring + β ($CC_{Ph}C_{COOH}$)
507	β ($CC_{Ph}C_{COOH}$)+ γ (OH) + δ Phenyl ring
556	ν_{asym} (CoO) + δ Phenyl ring+ γ(OH)
564	ν_{asym} (CoO) + δ Phenyl ring
679	ν_{sym} (CoO) + β $(COC)_{ether}$+ γ (OH) + δ Phenyl ring
718	γ (OH) + γ (CH) + β $(COC)_{ether}$
745	β $(OCO)_{COOH}$+ β $(COC)_{ether}$ + γ(CH)
818	β (OCO)+ β $(COC)_{ether}$ + δ Phenyl ring
848	γ $(CH)_{phenyl}$
881	β $(OCO)_{carboxylate}$ + ν_{asym} $(CO)_{ether}$ + δ Phenyl ring
898	γ $(CH)_{phenyl}$ + δ Phenyl breathing + β $(COC)_{carboxylate}$ + β $(OCO)_{carboxylate}$
1153	ν_{sym} $(CO)_{carboxylate}$ + δ Phenyl ring
1189	ν $(CO)_{ether}$ + β $(CH)^{b}$
1205	ν $(CO)_{ether}$ + β $(CH)^{a}$
1223	ν $(CO)_{ether}$ + β (COH) + ν(CC)^{b}
1338	ν $(CO)_{ether}$ + β $(CH)^{a}$
1469	ν $(CC)_{carboxylate}$ + ν_{sym} $(CO)_{carboxylate}$ + β(CH)^{a}
1571	ν $(CC)_{carboxylate}$ + ν $(CC)_{phenyl}$ + β $(CH)^{a}$
1650	ν $(CC)_{phenyl}$
1670	ν $(CC)_{phenyl}$
1833	ν $(C{=}O)_{carboxylic\ acid}$

ν - stretching; ν_s - sym. stretching; ν_{as} - asym. stretching; β - in-plane-bending; γ - out-of-plane bending;; δ - deformation; sh – shoulder; br - broad

[a] localized on phenyl group closest to Co(II)

[b] localized on phenyl group attached to the carboxylic acid group

2.2 DISCUSSION

2.2.1. X-ray absorption spectroscopy analysis

2.2.1.1 XANES analysis.

The differences observed in the XANES region before and after activation, as highlighted in Figure 2.4 are indicative of the local coordination geometry changes about the cobalt sites in CoHoba upon removal of these water molecules. The pre-edge feature at 7710 eV ascribed to the 1s to 3d bound state transition has low but measurable intensity in the spectrum of the hydrated material, CoHoba, in concert with a near octahedral coordination geometry.[30] This transition, despite being dipole forbidden is still observed due to both 3d + 4p mixing and quadrupolar coupling. The intensity of the 1s → 3d pre-edge feature increases significantly upon in situ monitoring of the dehydration process, which indicates a loss of centrosymmetry consistent with a distortion in coordination towards tetrahedral geometry. [31-33] The relative intensity of this peak has been used along with simplified angular overlap estimates to approximate the dihedral angle between the ligand-metal-ligand planes in a series of 4 coordinate copper complexes with known geometries ranging from square planar to tetrahedral.[34] That study, which aimed to quantify the level of tetrahedral distortion in 4 coordinate Cu(II) complexes based on the observed 1s → 3d relative intensity, predicts a nearly three-fold increase in the peak intensity upon changing the dihedral angle from 0^o to 90^o (i.e., D_{2h} to D_{2d} symmetry). While a direct comparison with these results is compromised by the different ligand field environment provided by the Hoba linker and change in coordination number in the case of CoHoba, the ~2.5 times relative intensity increase of

the 1s → 3d in XANES spectrum of the water free CoHoba, indicates a Co coordination is closer to the D_{2d} limit.

Moreover, the octahedral to tetrahedral geometry change is further supported by the lack of appearance of a resolved 1s → 4p transition shoulder feature on the rising edge, which is typically strong for square planar and weak for tetrahedral coordination. [31] The reduced "white line" intensity at 7725 eV is at least in part due to the lower cobalt coordination number of the dehydrated CoHoba (i.e. fewer scattering path contributions) although multiple scattering and other contributions to the intensity in this region complicate the interpretation and prevent a quantitative assessment of coordination number from XANES data alone.

By comparison, Cu K-edge XANES spectra of HKUST-1 before and after dehydration to remove the metal-bound water molecules shows a different set of changes in the edge region. [18] Notably, while the 1s → 3d pre-edge peak exhibits very little change, the resolved 1s →4p shoulder shows measurable enhancement. These changes are consistent with the more rigid paddle wheel SBU structure containing the Cu sites. In other words, unlike the flexible network of CoHoba, HKUST-1 does not experience a significant dihedral angle change between the two O-Cu-O planes and thereby retains a more square planar symmetry in the process. These correlations between XANES features and ligand field geometries of transition metal complexes have been well established in the literature with model complexes showing similar trends. [30-36]

2.3.1.2 EXAFS analysis

While the XANES region is sensitive to the local geometry, analysis of the EXAFS region provides accurate radial distance information about the cobalt sites, in

other words Co coordination number and bond lengths. The experimental EXAFS spectrum for the as-synthesized material, CoHoba is depicted in Figure 2.5 with the Fourier Transform $\chi(R)$ spectrum produced using a k-range of 2-12.0 $Å^{-1}$ and k-weight of 2. The calculated fit to these data over the R range 1–4 Å is generated using a model (Figure 2.6) based on the theoretical scattering paths derived from the reported single crystal data for CoHoba. [16] As the overlay in Figure 2.5b illustrates, the calculated $\chi(R)$ spectrum not only accurately reproduces the first peak at R=1.60 Å arising from the Co-O single scattering paths but also mimics the complicated amplitude pattern in the region beyond this first shell peak, which arises from multiple interfering longer distance single and multiple scattering paths. The fit was produced using fixed scattering path degeneracies derived from the model, and a symmetric expansion variable to allow the effective scattering path lengths to vary while maintaining their relative distances to one another. A summary of the parameter values obtained from the best fit is found in Table 2.1 along with the corresponding distances derived from the crystal structure. This comparison illustrates that the fit yields distance information with negligible deviation from the crystal structure.

After activation, the $\chi(k)$ data show a significant decrease in the amplitude and frequency of oscillations (Figure 2.7a). The corresponding $\chi(R)$ spectrum (Figure 2.7b) reflect lower scattering amplitudes and shorter scattering path distances across the measurable *R* range. These changes proved not to be merely a consequence of an elevated temperature effect as they persisted even after cooling the sample back to RT when the final data sets were collected for fitting. Given the complexity of the structure, and lack of crystallographic information on the activated CoHoba, the fitting model used for the

comparison of the pre- and post-dehydration EXAFS data was simplified by limiting it to one average first shell Co-O scattering path. Consequently, the *R*-range for these fits was restricted to 1-2.1 Å, which effectively encompasses only the first shell distance range. For the pre-activation EXAFS data, a fixed Co-O scattering path degeneracy of 6 was used in its first shell fit to reflect the known coordination number of the octahedral Co sites in the hydrated CoHoba while the amplitude term S_0^2, the energy shift, ΔE_0, effective length of the Co-O scattering path $R_{eff,}$ and the mean-square disorder of neighbor atoms σ^2 were varied. The post-activation EXAFS data were fit using the same amplitude, S_0^2 and energy shift, ΔE_0 values as obtained from the pre-activation fit while *N*, R_{eff} and σ^2 parameters were varied. A comparison of the parameter values obtained from these calculated fits, which is presented in Table 2.2, reveals the quantitative structure changes of the Co coordination environment upon dehydration. Specifically the R_{eff} distances reveal a 0.07 Å reduction in Co-O coordination bond length while the best fit scattering path degeneracy value of 4.2 confirms the expected coordination number decrease accompanying near complete removal of metal bound water molecules.

2.3.2. Raman spectroscopy analysis

2.3.2.1 Vibrational mode assignments.

The vibrational mode assignments for the Raman spectra of CoHoba and activated CoHoba were made by rigorous comparisons with experimentally collected Raman spectra for several reference materials, which included a D_2O solvated version of CoHoba and the protonated and deprotonated forms of the H_2oba linker alone. Theoretical vibrational frequency calculations were performed and compared with well

established literature values where applicable to aid the Raman band assignments of these linker systems.

Comparison of the Raman spectrum of the hydrated CoHoba with that of the version containing D_2O reveals the modes that involve the coordinated solvent through the frequency downshifts induced by the effect of the heavier isotope. Two prominent bands at 788 and 1082 cm^{-1} are present in the deuterated version and not in the water containing one. Their disappearance upon activation to remove the D_2O strongly points to their assignments as the coordinated D_2O Co-O stretch and D-O-D bend respectively. The expected downshift in frequencies of theses Raman bands leads to the identification of the analogous modes in the hydrated CoHoba, with the water bending mode assigned to the peak at 1550 and the Co-O (coordinated water) stretch contributing to the overlapping band region between 800 and 850 cm^{-1}. These assignments are further supported by the loss in intensity that occurs in these frequency regions upon activation, indicating the removal of coordinated water molecules.

Many of the modes, particularly those localized on the linker components, can be assigned unambiguously based on known characteristic frequency ranges for different functional groups. [37] Accordingly, the intense peak at 1612 cm^{-1} in the Raman spectrum of CoHoba is assigned to a phenyl CC stretch and the broad shoulder at higher energy (~1630 cm^{-1}) is identified as the CO stretch of the carboxylic acid side of the linker. The symmetric and asymmetric CO stretches of the carboxylate moieties are assigned to the peaks in the hydrated CoHoba at 1416 and 1508 cm^{-1}, respectively. These assignments were also supported by the comparison of the Raman spectra with those of both oxybis(benzoic acid) and oxybis(benzoate) disodium salt. As illustrated in Figure 2.9, the

dicarboxylic acid contains the broad COOH feature between 1600 and 1650 cm^{-1} while the dicarboxylate does not. Similarly, the deprotonated form contains the carboxylate stretches at 1430 and 1503 cm^{-1} while the protonated form shows no peaks in this region. Both forms of the linker contain the characteristic aromatic C-C stretching peak around 1600 cm^{-1}. A similar comparison of CoHoba with the linker references shows that all spectra contain a peak around 1200 cm^{-1}, which falls in the characteristic frequency range of ether group symmetric C-O stretches. [37] DFT vibrational mode calculations on the protonated and deprotonated forms of the linker in this frequency range also support this assignment. The experimental spectra contain peaks around 1135 and 1165 cm^{-1}, which are primarily attributed to in-plane C-H wagging modes on the phenyl groups but are also likely coupled to ring distortions and/or motion of the carboxylate/carboxylic acid groups, as indicated by the DFT calculations of these modes. In the CoHoba spectrum, these modes exhibit energy splitting; a likely consequence of the reduced symmetry and unequal environments of the two phenyl groups in the metal coordinated linker.

The reference spectra and corresponding DFT vibrational mode calculations facilitate the identification of linker modes in the lower frequency region as well, where assignments are typically more challenging. The prominent peak at ~850 cm^{-1} in the CoHoba spectrum is assigned to a linker mode dominated by phenyl ring distortions and OCO carboxylate bending motion. This assignment is based on the observed peak and calculated mode in this frequency region for the reference dicarboxylate linker. At slightly lower energy, several bands with peak maxima at around 800 and 810 cm^{-1} are assigned, with the aid of vibrational calculations on both linker references, to a combination of modes involving phenyl ring, out-of-plane C-H, and hydrogen bond

distortions coupled with bending modes of the oxy bridge. The overlapping intensities and more delocalized nature of the coupled linker modes in this frequency range, however, undermines our confidence in this assignment. The remaining modes observed in this low frequency region are most likely attributed to phenyl ring distortions and tilting modes with the exception of the peak at 645 cm^{-1}, which we have assigned to the Co-O stretch involving the metal and the coordinated linker carboxylate. Despite the fact that this band severely overlaps with and is most likely coupled to the linker-based modes in this frequency region, several factors lend credence to the assignment in this case. For one, theoretical calculations on a model complex composed of the Hoba linker coordinated to a Co(II) ion (Table 2.6) predict a Co-O stretching mode precisely in this frequency range. Also, this region of the low frequency range below 700 cm^{-1} Raman shift, where most metal-ligand stretches fall,[38] is the only part of the spectrum that experiences a significant frequency shift after activation.

2.3.2.2 Structural change implications

Differences in frequency and intensity observed in the Raman spectrum of CoHoba upon dehydration, as illustrated in Figure 2.8 and summarized in Table 2.3, signify the structure changes that occur in the process. An analysis of these spectral changes and the inferred structural ramifications follows.

The loss of coordinated water molecules is indicated by the disappearance of the modes associate with them. Specifically the broad peak at ~1530 cm^{-1}, which is assigned to the coordinated water bending mode shows drastically reduced intensity after activation. Some of the intensity loss in the 800-850 cm^{-1} range may be attributed to dehydration as well since the Co-O_{water} stretching frequency is suspected to be in this

region based on comparison with the Raman spectrum of the D_2O version of CoHoba (see Figure 2.9). The overlapping bands in this region however, prevent a definitive assignment for this vibrational mode.

Changes observed for the vibrational modes involving the Co and carboxylate linker oxygen corroborate the conclusions drawn from the XAS analysis. For example, the mode containing significant Co-O_{linker} stretching character, assigned to the peak at 645 cm^{-1}, exhibits a significant increase in frequency (and therefore force constant) after activation. This trend is consistent with the shorter, more covalent Co-O coordination bonds in the tetrahedral geometry suspected in the dehydrated state. Additionally, the frequency difference between the symmetric and asysmmetic C-O stretch in metal carboxylate complexes has been connected to the carboxylate OCO angle, with reduced splitting accompanying smaller bond angle, albeit in the context of comparing bridging versus chelating carboxylate complexes.[39-41] Therefore, after activation of CoHoba, the observed ~20 cm^{-1} decrease in splitting between the vibrational modes assigned to the symmetric and asymmetric carboxylate C-O stretches suggest a smaller, less strained, bridging carboxylate angle in activated CoHoba compared to the water coordinated network as the cobalt sites collectively distort to tetrahedral geometry. This hypothesis is further supported by the behavior of the 851 cm^{-1} Raman band assigned to a vibration dominated by OCO bending motion of the carboxylate groups. The downshift of this mode to 847 cm^{-1} upon dehydration is consistent with a smaller force constant that would be associated with a less strained bond angle.

Closer inspection of the COO stretching modes reveals that upon activation only the symmetric mode upshifts in frequency to reduce Δ, while the asymmetric COO

stretch is effectively unchanged. The different behavior of these modes is most likely attributed to the steric effects imposed by the bridging coordination of the Hoba linkers. Since the asymmetric mode involves simultaneous shortening and lengthening of C−O bonds, its force constant would not be as significantly altered by the reduced metal−carboxylate coordination sphere as that of the symmetric mode, where both C−O bonds shorten and lengthen in concert. This trend has been documented and explained for other metal carboxylate complexes in which the carboxylate ligand coordination is varied.[42, 43]

Unlike XAS characterization, vibrational spectroscopy studies are not limited to the immediate coordination sphere around the metal sites. In fact they are particularly revealing of the structure change happening on the linker parts of the network. The Raman peak at 801 cm^{-1} attributed primarily to a mode that contains significant COC bending of the oba ether group downshifts to 792 cm^{-1} indicating a change in the dihedral angle between the two phenyl rings in the dehydrated CoHoba and can be explained by considering the bridging oxygen lone pair electron interactions with the neighboring aromatic carbons. In other words, a smaller dihedral angle would lead to increased electron repulsion between the lone pair electrons on oxygen and the π system on the neighbor benzene ring, thereby weakening the C-O bonds. [44, 45] Similarly the peak around 1204 cm^{-1}, which are assigned to COC streching of the oba ether group downshifts in frequency by 4 cm^{-1}, indicating the C-O bond become slightly weaker upon activation. The red shift is much smaller since the stretching mode is less sensitive to bond angle change. Finally, the frequency of the peak at ~1275 cm^{-1}, which we attribute to a (OH…O) distortion between the H-bonded carboxylic acid groups, remains

unchanged after dehydration. This indicates an overall retention of the H-bonding network in the material, while the slight decrease in relative peak intensity, most likely through broadening, may indicate some additional disorder introduced in the H-bonding arrangement. Taken together, analysis of these linker localized vibrational modes suggests minimal change in hydrogen bond strength of between neighboring Hoba linkers with less constrained ether groups serving as "hinges" to accommodate the collective distortions about the Co sites. Notably, these conclusions are consistent with the PXRD measurements of of CoHoba and activated CoHoba, which indicate an expansion along the axis containing these H-bonded linkers.

By comparison, modes experiencing little change in frequency or intensity upon removal of metal bound waters tend to be located on the parts of the network that are less prone to structural rearrangement upon dehydration. For example the vibrations involving the aromatic carbons of the phenyl groups around 1612 cm^{-1} and the C-O and O-H bonds of the carboxylic acid side of the Hoba linker experienced negligible shift in frequency after activation. The low frequency modes below 650 cm^{-1} which tend to be dominated by phenyl ring rocking and out-of-plane deformations also appear to be immune to the structure changes associated with activation.

2.4 Conclusion

In this chapter, we probed the activation process in a flexible MOF material to elucidate the specific structural changes accompanying the metal-bound solvent removal. The two spectroscopy methods employed, XAS and Raman, proved uniquely complementary in attaining this information. This study not only established the efficacy of using this combined spectroscopy approach for interrogating molecular level structure in these porous hybrid materials, but it also revealed the sometimes drastic *local* coordination geometry changes of the metal sites that can occur upon activation but are not readily apparent through PXRD measurements. In the specific material chosen for this investigation, the cobalt (II) sites undergo a change from octahedral to tetrahedral coordination geometry leading to increased covalency of the metal carboxylate bonds and therefore a contraction of the coordination spheres. The results also suggest that the oxygen bridge on the Hoba linker provides a point of flexibility that allows the network to undergo significant distortion while maintaining crystallinity. These structure changes inferred from the XAS and Raman studies are consistent with those indicated by the PXRD measurements, i.e. the crystal expansion between $Co(Hoba)_2$ layers of the network. Taken together, the consequences of these local and long range order structural changes may be crucial for understanding their role in catalytic processes. For example, while coordinated solvent removal through activation implies increased availability of open metal sites for catalytic reactions, the reduced coordination sphere and tetrahedral geometry distortion could in fact inhibit metal accessibility for some particularly flexible networks. Future studies will be dedicated to using these spectroscopy methods for *in situ* interrogation of catalysis reactions in this and other materials.

2.5 Materials and Methods

2.5.1 MOF materials.

The material and corresponding XRD, TGA data were provided by Professor Jing Li in Department of Chemistry at Rutgers University-New Brunswick. The synthesis of CoHoba was performed according to the previously published procedure, [45] $Co(NO_3)_2 \cdot 6H_2O$ (0.4 mmol) and H_2oba (0.8 mmol) were mixed in 10 mL of distilled water, and two drops of TEA was added in to the solution to adjust the pH value to ~7.00. The solution was then heated at 120 °C for 3 days, followed by cooling at a rate of 0.1 °C/min to room temperature. The pink plate-like crystals of **1** (0.1452 g, 0.24 mmol, 60 % yield based on cobalt) were collected.

3.5.2 Powder X-ray diffraction

Powder X-ray diffraction patterns of all the samples were recorded on a Rigaku Ultima IV X-Ray diffractometer at room temperature using Cu Kα radiation (λ = 1.5406 Å). Graphite monochromator was used and the generator power settings were at 40 kV and 44 mA. Data were collected between a 2θ of 3-50° with a step size of 0.02° at a scanning speed of 4.0 deg/min.

2.5.3 Thermogravimetric Analysis

Thermogravimetric (TG) analysis was performed on a TA Q50 Thermogravimetric Analyzer with a temperature ramp of 10 °C/min from room temperature to 600 °C under nitrogen gas flow. The TG profile (Figure 2.10) shows a

weight loss of 6.0 wt% for the as-synthesized sample in the range of 110 °C to 160 °C upon heating. The weight loss can be assigned to the coordinated water molecules and matches very well with the theoretically calculated amount (5.9 %) based on the crystal structure. The water-free sample is thermally stable up to 300 °C, followed by decomposition at higher temperatures.

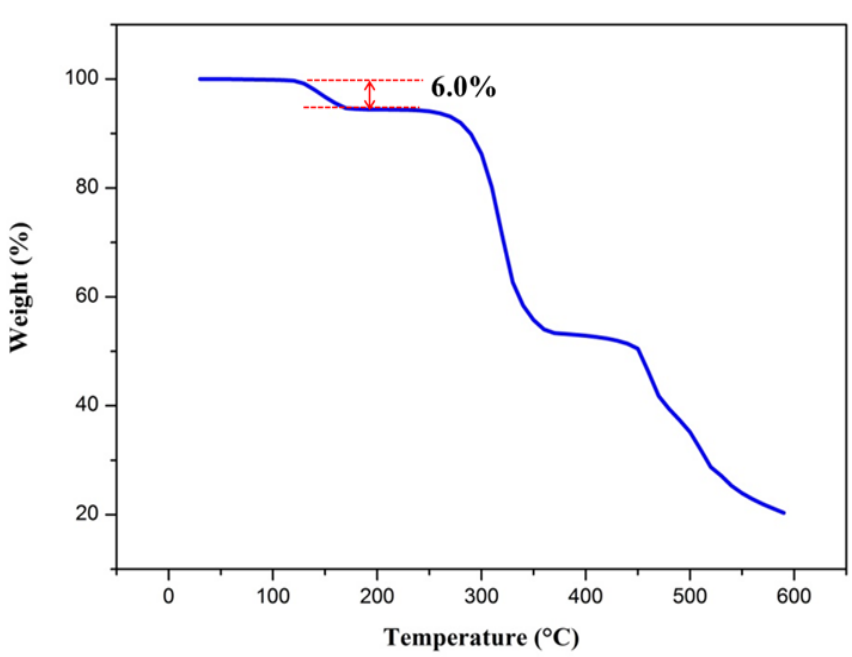

Figure 2.10 Thermogravimetric analysis of a freshly prepared sample of CoHoba showing a good match of the observed weight loss with the calculated value.

2.5.4 X-ray Absorption Spectroscopy

The X-ray absorption data were collected at Beamline X18A at the National Synchrotron Light Source (NSLS). Spectra were collected at the Cobalt K-edge (7709eV) in transmission mode. The X-ray white beam was monochromatized by a Si(111) monochromator and detuned by 25% to minimize the harmonic content of the beam. A cobalt foil was used as the reference for energy calibration. The incident beam intensity (I_0) was measured by a 15 cm ionization chamber with 70% N_2 and 30% He gas

composition. The transmitted beam intensity (I_t) and reference (I_r) were both measured by a 30 cm ionization chambers with 80% N_2 and 20% Ar gas composition.

XAS spectra were collected during the MOF activation process using a specialized sample chamber for in situ measurements, which has previously been described. [46] Briefly, the sample holder consists of 3 mm diameter Kapton tube mounted on a heater. A thermocouple wire in close proximity to the sample is used to monitor the temperature, which was adjusted by a temperature controller. 24.2 mg of CoHoba was thoroughly ground with ~100 mg boron nitride. The mixture was packed into the Kapton tube yielding approximately one absorption length. The sample chamber was continuously purged with dry Helium gas for the duration of the experiment.

XAS spectra of the as-synthesized sample were first collected at room temperature (~25^{o}C) (four scans). While the sample was then gradually heated to 150^{o}C, spectra were continuously collected to monitor the activation process. The sample was maintained at this elevated temperature and data were collected on until no further changes were observed in the spectra (~2 hours) to ensure complete dehydration. The activation temperature was chosen based on previously published data, which showed complete dehydration of CoHoba under these conditions. The sample was then cooled to 25^{o}C and another four scans were collected after returning to this temperature to allow the spectra comparison between the hydrated and dehydrated materials without needing to compensate for temperature effects on the Debye-Waller factor in the analysis. The XAFS data were processed and analyzed using the Athena and Artemis programs of the IFEFFIT package based on FEFF 6. [47, 48]

2.5.5 Raman Spectroscopy

Raman spectra were collected using a 785 nm single frequency diode laser with ~ 25 mW power, a triple monochromator and a 1340 × 100 pixel liquid nitrogen-cooled CCD detector (Princeton Instruments). With 150 μm entrance slit width, the spectral resolution was < 5 cm^{-1} and peak frequency shifts of <1 cm^{-1} could be measured. Raman data of the as-synthesized sample was collected on a spinning pellet prepared from a mixture of 20 wt% of CoHoba in KNO_3, which is used as an internal frequency standard. The sample was spun to minimize the residence time of the laser on one spot of the sample thereby avoiding excessive heating that could locally activate the material. The dehydrated sample, activated CoHoba, was prepared for Raman measurements by suspending 20 mg of CoHoba in 1 ml H_2O in a quartz cuvette equipped with septum top screw cap and followed by extra- and intra-network dehydration at 150^oC in a vacuum oven overnight. Once the dried material had adhered to the walls, solid KNO_3 was added to the cuvette, which was immediately sealed upon removal from the oven.

2.5.6 DFT Computational methods and theoretical vibrational frequency results

The geometry optimizations and theoretical vibrational modes of several reference molecules were calculated using the Gaussian 09 program package [49] at the density functional theory (DFT) level with Becke's three parameter functional and Lee-Yang-Parr functional (B3LYP) method. 6-31G* basis set was used for all the calculations. Calculations were performed on the model systems whose optimized geometries are depicted in Figure 2.11. Mode descriptions were assessed based on animation of the atomic vector displacements using Chemcraft. A summary of the calculated frequencies

for the most Raman active vibrational modes is provided in Table 2.4, 2.5 and 2.6 and does not include compensation for vibrational mode anharmonicities through the use of a scaling factor.[2]

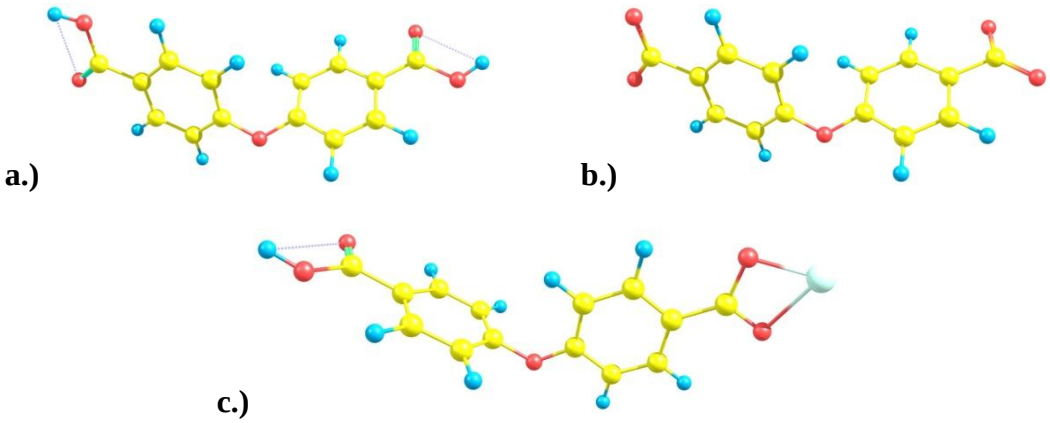

Figure 2.11 Optimized geometries for model systems, a) 4,4'-oxybis(benzoic acid) , b) 4,4'-oxybis(benzoate) c) coordination mode of 4,4'-oxybis(benzoate) to the Co metals.

2.6 Reference

1 X.-S. Wang, L. Meng, Q. Cheng, C. Kim, L. Wojtas, M. Chrzanowski, Y.-S. Chen, X. P. Zhang, S. Ma, *J. Am. Chem. Soc*., 2011, **133**, 16322.

2 B. J. Burnett, P. M. Barron, W. Choe, *CrystEngComm.* 2012, **14**, 3839.

3 S. Matsunaga, N. Endo, W. Mori, *Eur. J. Inorg. Chem.* 2012, 4885.

4 C. Serre, S. Bourrelly, A. Vimont, N. A. Ramsahye, G. Maurin, P. L. Llewellyn, M. Daturi, Y. Filinchuk, O. Leynaud, P. Barnes, G. Férey, *Adv. Mater.*, 2007, **19**, 2246.

5 C. Serre, F. Millange, C. Thouvenot, M. Noguès, G. Marsolier, D. Louër, G. Férey, *J. Am. Chem. Soc.*, 2002, **124**, 13519.

6 C. Mellot-Draznieks, C. Serre, S. Surblé, N. Audebrand, G. Férey, *J. Am. Chem. Soc.*, 2005, **127**, 16273.

7 Z. Wang, S. M. Cohen, *J. Am. Chem. Soc.*, 2009, **131**, 16675.

8 S. Devautour-Vinot, G. Maurin, F. Henn, C. Serre, G. Farey, *Phys. Chem. Chem. Phys.*, 2010, **12**, 12478.

9 F. Salles, G. Maurin, C. Serre, P. L. Llewellyn, C. Knöfel, H. J. Choi, Y. Filinchuk, L. Oliviero, A. Vimont, J. R. Long, G. Férey, *J. Am. Chem. Soc.*, 2010, **132**, 13782.

10 T. K. Trung, I. Déroche, A. Rivera, Q. Yang, P. Yot, N. Ramsahye, S. D. Vinot, T. Devic, P. Horcajada, C. Serre, G. Maurin, P. Trens, *Micropor. Mesopor. Mat.*, 2011, **140**, 114.

11 D. N. Dybtsev, H. Chun, K. Kim, *Angew. Chem. Int. Ed.,* 2004, **43**, 5033.

12 J. Seo, C. Bonneau, R. Matsuda, M. Takata, S. Kitagawa, *J. Am. Chem. Soc.*, 2011, **133**, 9005.

13 C.-L. Chen, A. M. Goforth, M. D. Smith, C.-Y. Su, H.-C zur Loye, *Angew. Chem. Int. Ed.*, 2005, **44**, 6673.

14 J.-P. Zhang, S. Horike, S. Kitagawa, *Angew. Chem. Int. Ed.*, 2007, **46**, 889.

15 A. C. McKinlay, J. F. Eubank, S. Wuttke, B. Xiao, P.S. Wheatley, P. Bazin, J. C. Lavalley, M. Daturi, A. Vimont, G. De Weireld, P. Horcajada, C. Serre, R. E. Morris, *Chem. Mater.*, 2013, **25**, 1592.

16 J. Zhang, A. V. Biradar, S. Pramanik, T. J. Emge, T. Asefa, J. Li, *Chem. Comm.*, 2012, **48**, 6541.

17 F. Bonino, S. Chavan, J. G. Vitillo, E. Groppo, G. Agostini, C. Lamberti, P. D. C. Dietzel, C. Prestipino, S. Bordiga, *Chem. Mater.*, 2008, **20**, 4957.

18 C. Prestipino, L. Regli, J. G. Vitillo, F. Bonino, A. Damin, C. Lamberti, A. Zecchina, P. L. Solari, K. O. Kongshaug, S. Bordiga, *Chem. Mater.*, 2006, **18**, 1337.

19 G. D. Combarieu, S. Hamelet, F. Millange, M. Morcrette, J.-M Tarascon, G. Férey, R. I. Walton, *Electrochem. Commun.*, 2009, **11**, 1881.

20 S. Bordiga, F. Bonino, K. P. Lillerud, C. Lamberti, *Chem. Soc. Rev.*, 2010, **39**, 4885.

21 L. J. Murray, M. Dinca, J. Yano, S. Chavan, S. Bordiga, C. M. Brown, J. R. Long, *J. Am. Chem. Soc.*, 2010, **132**, 7856.

22 L. Valenzano, B. Civalleri, S. Chavan, S. Bordiga, M. H. Nilsen, S. Jakobsen, K. P. Lillerud, C. Lamberti, *Chem. Mater.*, 2011, **23**, 1700.

23 H. Liu, Y. Zhao, Z. Zhang, N. Nijem, Y. J. Chabal, H. Zeng, J. Li, *Adv. Funct. Mater.*, 2011, **21**, 4754.

24 N. Nijem, P. Thissen, Y. Yao, R. C. Longo, K. Roodenko, H. Wu, Y. Zhao, K. Cho, J. Li, D. C. Langreth, Y. J. Chabal, *J. Am. Chem. Soc.*, 2011, **133**, 12849.

25 N. Nijem, H. Wu, P. Canepa, A. Marti, K. J. Balkus, T. Thonhauser, J. Li, Y. J. Chabal, *J. Am. Chem. Soc.*, 2012, **134**, 15201.

26 N. Nijem, P. Canepa, L. Kong, H. Wu, J. Li, T. Thonhauser, Y. J. Chabal, *J. Phys.: Condens. Matter*., 2012, **24**, 424203.

27 K. Tan, N. Nijem, P. Canepa, Q. Gong, J. Li, T. Thonhauser, Y. J. Chabal, *Chem. Mater.*, 2012.

28 Y. Yao, N. Nijem, J. Li, Y. J. Chabal, D. C. Langreth, T. Thonhauser, *Phys. Rev. B*, 2012, **85**, 064302.

29 H. Liu, Y. Zhao, Z. Zhang, N. Nijem, Y. J. Chabal, X. Peng, H. Zeng, J. Li, *Chem. Asian J.*, 2013, **8**, 778.

30 S. Della Longa, A. Bianconi, L. Palladino, B. Simonelli, A. Congiu Castellano, E. Borghi, M. Barteri, M. Beltramini, G. P. Rocco, B. Salvato, *Biophys. J.*, 1993, **65**, 2680.

31 J. A. McCleverty, T. J. Meyer, *Comprehensive Coordination Chemistry II*, Pergamon: Oxford, 2003, p 159.

32 J. Chen, S. Natarajan, J. M. Thomas, R. H. Jones, M. B. Hursthouse, *Angew. Chem. Int. Ed.*, 1994, **33**, 639.

33 J. Chaboy, C. J. Castro, *Non-Cryst. Solids*, 1997, **212**, 11.

34 M. Sano, S. Komorita, H. Yamatera, *Inorg. Chem.*, 1992, **31**, 459.

35 G. D. Gupta, S. K. Joshi, B. D. Shrivastava, K. B. Pandeya, *Jpn. J. Appl. Phys*., 1993, **32S2**, 833.

36 T. E. Westre, P. Kennepohl, J. G. DeWitt, B. Hedman, K. O. Hodgson, E. I. Solomon, *J. Am. Chem. Soc.*, 1997, **119**, 6297.

37 G. Socrates, *Infrared and Raman Characteristic Group Frequencies*; 3rd ed.; John Wiley & Sons, Ltd, 2001.

38 K. Nakamoto, *Infrared and Raman Spectra of Inorganic and Coordination Compounds, Part B: Applications in Coordination, Organometallic, and Bioinorganic Chemistry*; 6th ed.; John Wiley & Sons, Inc.: Hoboken, 2009.

39 G. B. Deacon, R. J. Phillips, *Coordin. Chem. Rev.,* 1980, **33**, 227.

40 A. I. Grigor'ev, A. I. Zh., *Neorg. Khim.,* 1963, **8**, 802.

41 N. W. Alcock, V. M. Tracy, T. C. Waddington, *J. Chem. Soc., Dalton Trans.*, 1976, **0**, 2243.

42 G. Lemercier, E. Mulliez, C. Brouca-Cabarrecq, F. Dahan, J.-P Tuchagues, *Inorg Chem.* 2004, **43**, 2105−2113.

43 V. Robert, G. A. Lemercier, *J. Am. Chem. Soc.* 2006, **128**, 1183−1187.

44 H. E. Van Wart, A. Lewis, H. A. Scheraga, F. D. Saeva, PNAS, 1973, **70**, 2619.

45 S. Qiu, L. Liu, X. Jin, A. Zhang, K. Wu, L. Wang, *Spectro. Chim. Acta A,* 2010, **77**, 572.

46 P. J. Chupas, M. F. Ciraolo, J. C. Hanson, C. P. Grey, *J. Am. Chem. Soc.*, 2001, **123**, 1694.

47 B. Ravel, M. Newville, *J. Synch. Rad.*, 2005, **12**, 537.

48 J. J. Rehr, R. C. Albers, *Rev. Mod. Phys.*, 2000, **72**, 621.

49 M. J. Frisch, G. W. Trucks, H. B. Schlegel, G. E. Scuseria, M. A. Robb, J. R. Cheeseman, G. Scalmani, V. Barone, B. Mennucci, G. A. Petersson, H. Nakatsuji, M. Caricato, X. Li, H. P. Hratchian, A. F. Izmaylov, J. Bloino, G. Zheng, J. L. Sonnenberg, M. Hada, M. Ehara, K. Toyota, R. Fukuda, J. Hasegawa, M. Ishida, T. Nakajima, Y. Honda, O. Kitao, H. Nakai, T. Vreven, J. A. Montgomery, Jr., J. E. Peralta, F. Ogliaro, M. Bearpark, J. J. Heyd, E. Brothers, K. N. Kudin, V. N. Staroverov, R. Kobayashi, J. Normand, K. Raghavachari, A. Rendell, J. C. Burant, S. S. Iyengar, J. Tomasi, M. Cossi, N. Rega, J. M. Millam, M. Klene, J. E. Knox, J. B. Cross, V. Bakken, C. Adamo, J. Jaramillo, R. Gomperts, R. E. Stratmann, O. Yazyev, A. J. Austin, R. Cammi, C. Pomelli, J. W. Ochterski, R. L. Martin, K. Morokuma, V. G. Zakrzewski, G. A. Voth, P. Salvador, J. J. Dannenberg, S. Dapprich, A. D. Daniels, Ö. Farkas, J. B. Foresman, J. V. Ortiz, J. Cioslowski, and D. J. Fox; Gaussian Inc.: Wallingford, CT, 2010.

Chapter 3. *In situ* spectroscopy studies of CO_2 adsorption in a dually functionalized microporous metal-organic framework

3.1 Introduction

The tunable chemical composition, pore size and shape and the unique functionalities these attributes afford make MOF materials ideal for potential adsorption-based applications such as gas separation and storage, heterogeneous catalysis, luminescence-based sensing and others. Several recent reviews have highlighted the progress made in developing MOFs for these applications.[1-9] Current interest in carbon sequestration technology for reducing the amount of atmospheric greenhouse gases has prompted the development of MOF materials for selective CO_2 filtering to prevent its release into the atmosphere, for example from the flue gas emissions of industrial processes. In contrast to conventional CO_2 adsorption technologies, which often suffer from either low capacity or low selectivity, MOFs can be designed with high densities of potential binding sights with strong affinities for CO_2 molecules. For example, the well-studied framework, MOF-74[10] (also known as CPO-27)[11, 12] exhibits exceptional CO_2 uptake and selectivity, particularly for the Mg version, due to its large surface to volume ratio and the favorable binding between CO_2 and the accessible open metal sites lining the channels of the framework.[13, 14] Other frameworks take advantage of the Lewis basicity of amines for promoting CO_2 adsorption ability by incorporating them at linker positions.[15, 16] Furthermore, a handful of frameworks incorporate both types of binding sites (i.e. coordinatively unsaturated metal nodes and amine functionalized linkers) as a strategy for improving MOF CO_2 adsorption performance.[17, 18] In all these frameworks,

an in-depth understanding of the intrinsic host-guest interactions behind the CO_2 adsorption mechanism, which has been the target of several recent experimental and computational studies,[19-23] will be helpful in directing the design of new MOFs for this adsorption-based application. The added structural complexity of dually functionalized frameworks makes assessing the adsorption mechanism especially complicated and a task best tackled using multiple *in situ* characterization methods.

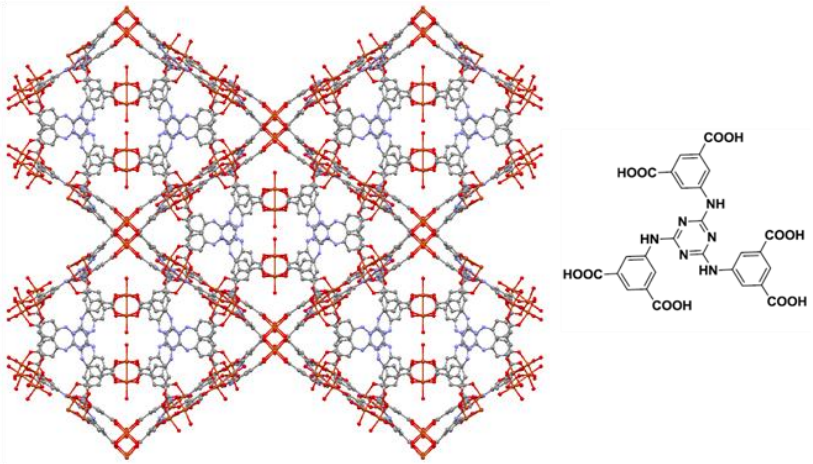

Figure 3.1 Crystal structure of CuTDPAT (left) and H6TDPAT linker (right).

In chapter 2, we show that XAS and Raman spectroscopy are useful complementary techniques to reveal structural changes. In this chapter, we not only focus on interrogating the activation process but also the framework-CO_2 interaction the Cu-based MOF depicted in Figure 3.1, $[Cu_3(TDPAT)(H_2O)_3]\cdot 10H_2O\cdot 5DMA$ (TDPAT=2,4,6-tris(3,5-dicarboxylphenylamino)-1,3,5-triazine). This MOF, which has previously been reported [24, 25] was designed to have both types of potential binding sites for CO_2 adsorption described above; coordinatively unsaturated metals and secondary amine linker functionality. As in other *rht*-type MOFs [26-32] with potentially open metal sites, the paddle wheel Cu sites in CuTDPAT are rendered pore wall accessible by

removal of coordinated labile solvent molecules through thermal activation. The secondary amines that serve as Lewis base sites for gas adsorption are incorporated on the phenyl groups of the triazine linkers. While its remarkable selectivity for CO_2 adsorption has been shown by gas isotherm measurements [24 ,25] and further substantiated through computational studies, [22, 23] the specific molecular level interactions and framework structure changes associated with that behavior have not been evaluated in great detail. In this work, the activation and CO_2 gas adsorption processes in CuTDPAT are probed using a combination of *in situ* spectroscopy techniques, namely UV-visible diffuse reflectance, X-ray absorption and Raman spectroscopy. While the diffuse reflectance measurements probe valence electron transitions, XAS involves monitoring specific core electron transfer processes. Both methods are well suited for studying metal containing materials. The former provides valuable electronic and indirect geometry information through the behavior of the d-d absorption bands. The interpretation of both the X-ray absorption near edge structure (XANES) and extended X-ray absorption fine structure (EXAFS) spectral regions allows complementary evaluation of metal oxidation state, coordination geometry and short range distance information. XAS is well established in the study of other solid state porous materials such as zeolites [33-37] and while it is increasingly being incorporated in the arsenal of MOF characterization methods, its utility has been primarily limited to aiding the refinement of MOF crystal structures and verifying the coordination environments of post-synthetically incorporated metal sites. [38-40] When applied to MOF materials through *in situ* measurement, this technique can provide electronic and atomic level distance information needed to determine potentially important metal electron distribution and framework structural

changes during the host-guest adsorption events. In addition to our own work, [41] other studies have employed XAS to interrogate the local metal coordination in MOF materials upon activation and subsequent adsorption of various gases. [40, 42, 43] Raman spectroscopy is another important characterization technique amenable to both *in situ* and solid state sample measurement. In the context of this work, it is used to monitor the vibrational frequencies assigned to the different components of the framework and the adsorbed CO_2 molecules within the pores. The important structural changes and relative participation of the different framework components are implicated by the observed changes in the individual Raman modes. The utility of this technique has been demonstrated for the structural characterization of MOF materials and their adsorption processes. [19, 41, 44-53] As demonstrated below, each technique has its own limitations, but when combined they generate a more complete picture of activation and gas adsorption process and the local structural ramifications.

3.2 Result

3.2.1 UV-vis diffuse reflectance spectroscopy

The diffuse reflectance spectra of CuTDPAT obtained during activation and CO_2 gas treatment are showed in Figure 3.2. Spectral shift of the lowest energy band is observed almost immediately upon heating and no further change occurs after 70ºC. The maximum absorption of the lowest energy band is observed to blue shift from 708 to 581 nm upon dehydration. Upon subsequent exposure to CO_2 gas environment, the absorption maximum red shifts to a final peak position of 608 nm.

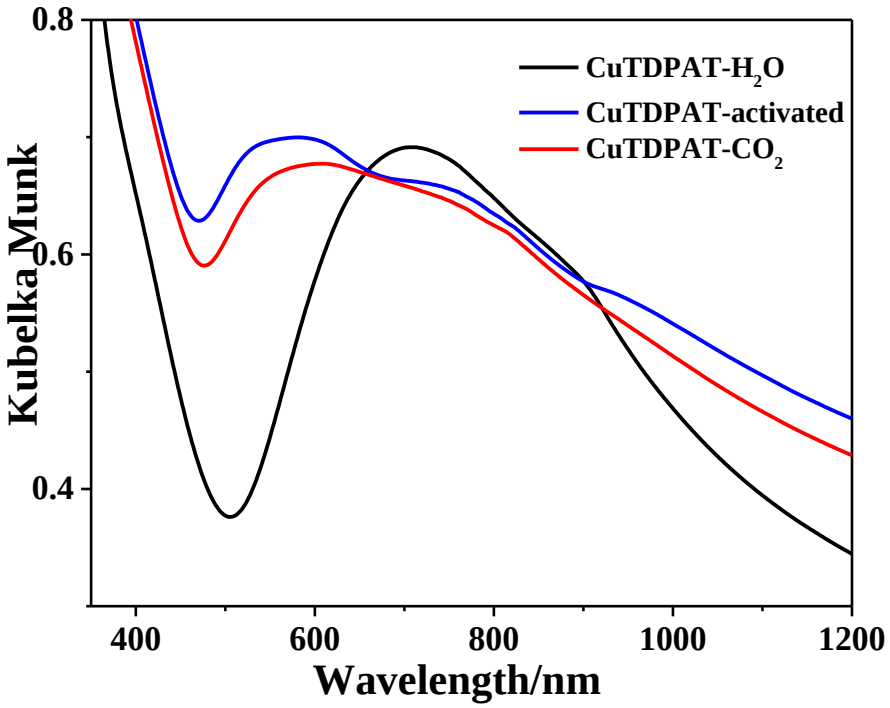

Figure 3.2 In-situ absorption spectroscopy of CuTDPAT (black), activated CuTDPAT (blue), activated CuTDPAT treated with CO_2 (red).

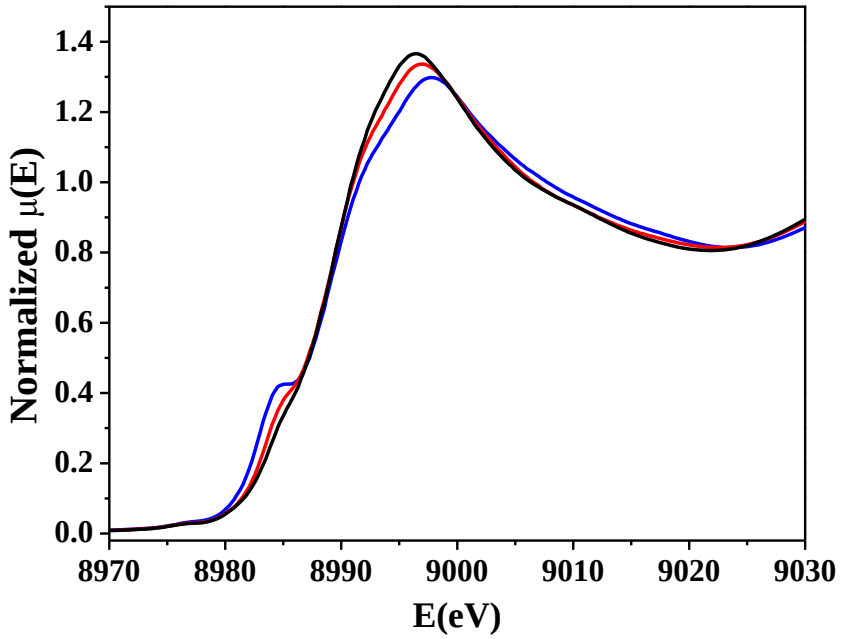

Figure 3.3 Copper K-edge XANES spectra of CuTDPAT (black), activated CuTDPAT (blue), activated CuTDPAT treated with CO_2 (red), all obtained at room temperature.

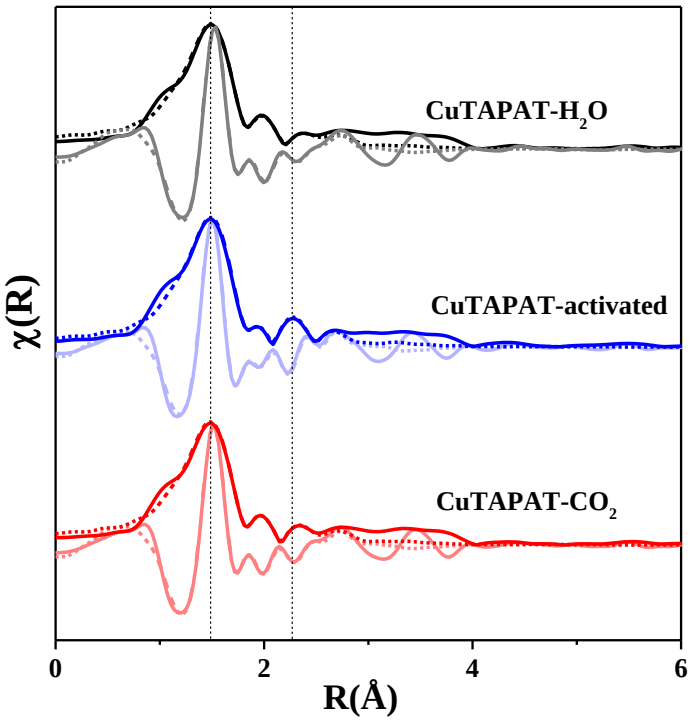

Figure 3.4 Comparison between experimental EXAFS data (solid line) with theoretical fit (dashed line) in R-space (magnitude and real components).

Table 3.1 Summary of EXAFS fitting Parameters.

Scatterig Path	degeneracy (*N*)	R_{eff} (Å)	σ^2 (Å^2)
CuTDPAT-Hydrated : R^2=0.002			
Cu_{abs}-O1	4	1.96 ± 0.01 (1.94) [b]	0.005±0.001
Cu_{abs}-O_{water}	1	2.11 ± 0.08 (2.13)	0.018±0.024
Cu_{abs}-Cu2	1	2.65 ± 0.04 (2.63)	0.008±0.004
Cu_{abs}-C	4	2.87 ± 0.05 (2.84)	0.005±0.005
Cu_{abs}-C-O	8	3.00 ± 0.06 (3.02)	0.006±0.008
CuTDPAT-Activated : R^2=0.003			
Cu_{abs}-O1	4	1.94±0.004	0.005±0.001
Cu_{abs}-Cu2	1	2.55±0.04	0.011±0.004
Cu_{abs}-C	4	2.83±0.03	0.006±0.004
Cu_{abs}-C-O	8	2.96±0.04	0.004±0.005
CuTDPAT-CO_2: R^2=0.003			
Cu_{abs}-O1	4	1.95±0.01	0.005±0.001
Cu_{abs}-Oco_2	0.76 ± 0.5[a]	2.14±0.13	0.017±0.034
Cu_{abs}-Cu2	1	2.63±0.06	0.009±0.006
Cu_{abs}-C	4	2.86±0.06	0.005±0.005
Cu_{abs}-C-O	8	2.99±0.06	0.006±0.008

3.2.2 X-Ray Absorption Spectroscopy

Averages of three XAS scans obtained at room temperature, including before and after activation, as well as after CO_2 loading and rehydration are depicted in Figures 3.3 and 3.4. The changes occurring in the XANES region under these conditions are shown in Figure 3.3 while the EXAFS data and corresponding fits of the CO_2-loaded and rehydrated sample are presented in Figure 3.4. In the latter, EXAFS spectra are shown as the Fourier transform $\chi(R)$ spectra produced using a *k* range of 2-12.5 Å^{-1} and *k* weight of 2. The calculated fit to these data was performed over an R range 1.0-3.1 Å and was generated using a model based on the theoretical scattering paths derived from the reported single crystal data for Cu-TDPAT. [24] The parameter values obtained from the best fits are summarized in Table 3.1. For the hydrated material, the EXAFS fit was generated using fixed scattering path degeneracies, *N*, as determined by the single crystal structure model while the amplitude term, S_0^2, the energy shift, ΔE_0, effective length of

the scattering path R_{eff}, and mean-square disorder term of neighbor atoms σ^2 for each of these paths were variable parameters. The same model without the Cu-O_{water} scattering path was used to fit the post-activation EXAFS data. In this case, the S_0^2 and ΔE_0 values were fixed to those obtained from the pre-activation fit along with the scattering path degeneracies. The scattering path effective distance and disorder parameters however were used as variables. Finally, to fit the spectrum of the CO_2 loaded material the fitting model included an axially positioned O to generate the relevant Cu-O_{CO2} scattering path. It should be noted that EXAFS has limited utility for distinguishing among scattering paths involving the same or similar atoms, such as C, N or O. The fitting scheme described above is only possible because of the ability to restrict the fitting model using *a priori* knowledge of the exact coordination environment from single crystal data and the overall change in coordination known to occur upon the activation and gas adsorption. Nevertheless, some ill-defined fitting parameters are inevitable since the structure predicts several overlapping scattering paths that contribute to the same region of the EXAFS spectrum beyond the first shell peak. An analysis of these data and fits in the context of providing specific structural details about the dehydrated metal sites and their CO_2 interactions, including their limitations, is described in the Discussion Section.

3.2.3 Raman spectroscopy

Raman spectra collected upon activation and gas adsorption of CuTDPAT are shown in Figure 3.5. The observed vibrational frequencies along with corresponding mode assignments are summarized in Table 3.2. Vibrational mode assignments were made by comparison with well-established literature values, [57-61] the TDPAT ligand spectrum and its computed theoretical vibrational mode frequencies. These reference

spectra can be found in Figure 3.6 along with a summary of the DFT calculated TDPAT vibrations in Table 3.3. Accordingly, the intense set of overlapping peaks at 1598 and 1625 cm^{-1} is assigned to the phenyl C-C and amine C-N stretching modes respectively. The peaks in the 1200-1500 cm^{-1} region are dominated by C-C stretch, C-N stretch as well as C-H and N-H wagging modes of the linker. The main peak at 996 cm^{-1} is assigned to a phenyl ring breathing mode while the peak at 978 cm^{-1} is assigned to a triazine ring breathing mode. The region of the spectrum below ~900 cm^{-1} contains the low energy distortion modes of the linker and also those involving the metal site distortions. A triazine ring distortion mode occurs at 681 cm^{-1} in the hydrated framework and downshifts to 677 cm^{-1} upon activation. The strong feature at 497 cm^{-1} is assigned to a Cu-O stretch that includes coordinated water oxygen since it is not present in the ligand Raman spectrum and drastically changes upon activation. The peak in this region observed at 506 cm^{-1} for the activated framework is also attributed to this Cu-O stretch involving only the remaining metal carboxylate oxygen bonds. The broad peak at 171 cm^{-1} in the hydrated framework most likely contains a number of overlapping modes including a Cu- Cu stretch involving the weakly interacting Cu sites spanning the paddlewheel node. This vibration is more evident in the activated framework spectrum which contains a well-resolved up shifted peak at 230 cm^{-1} and is consistent with the vibrational assignments of other Raman studies on similar Cu frameworks. [62]

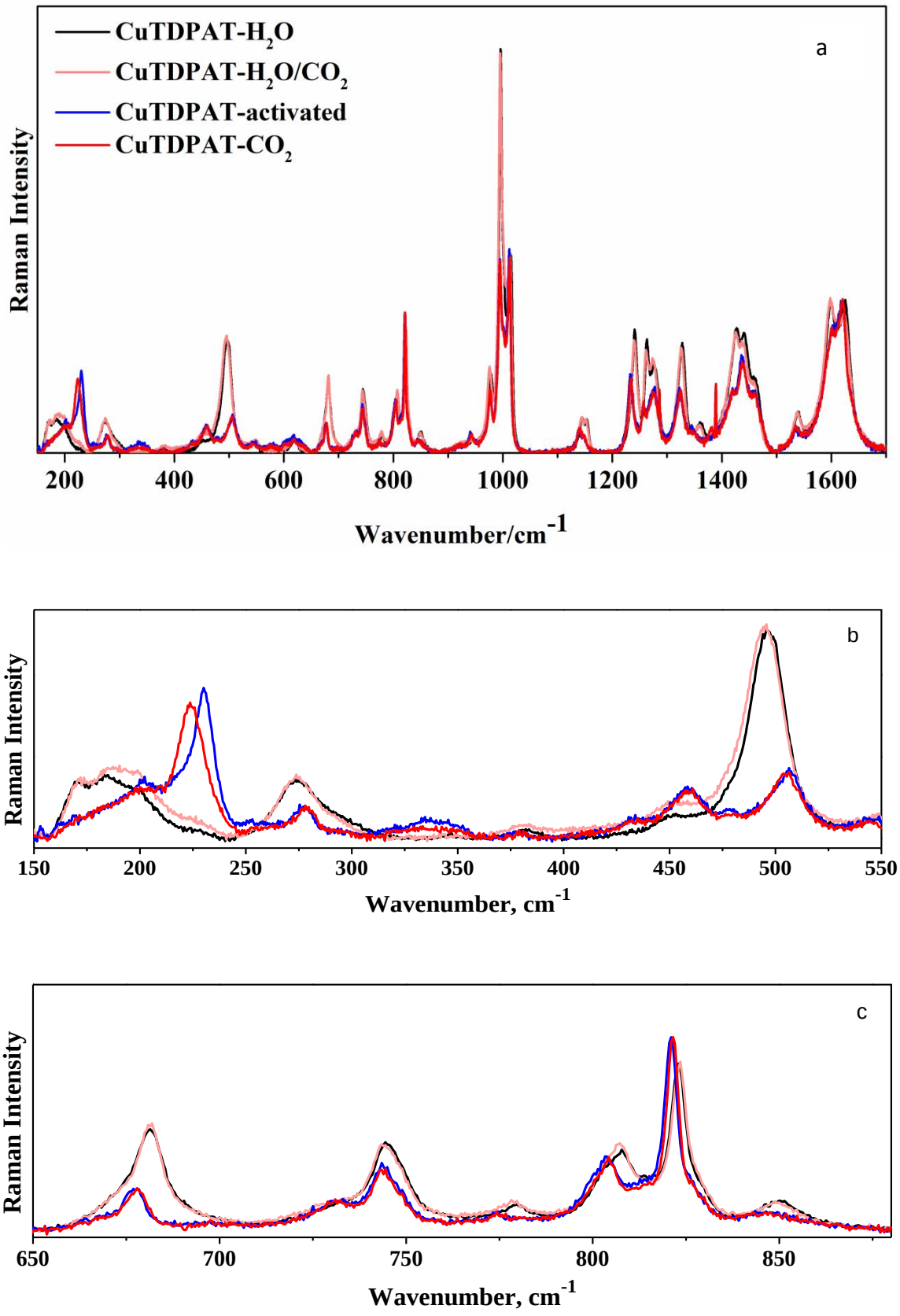
CuTDPAT-H2O
CuTDPAT-H2O/CO2
CuTDPAT-activated
CuTDPAT-CO2
a
Raman Intensity
200
400
600
800
1000
1200
1400
1600
Wavenumber/cm-1
b
Raman Intensity
150
200
250
300
350
400
450
500
550
Wavenumber, cm-1
c
Raman Intensity
650
700
750
800
850
Wavenumber, cm-1

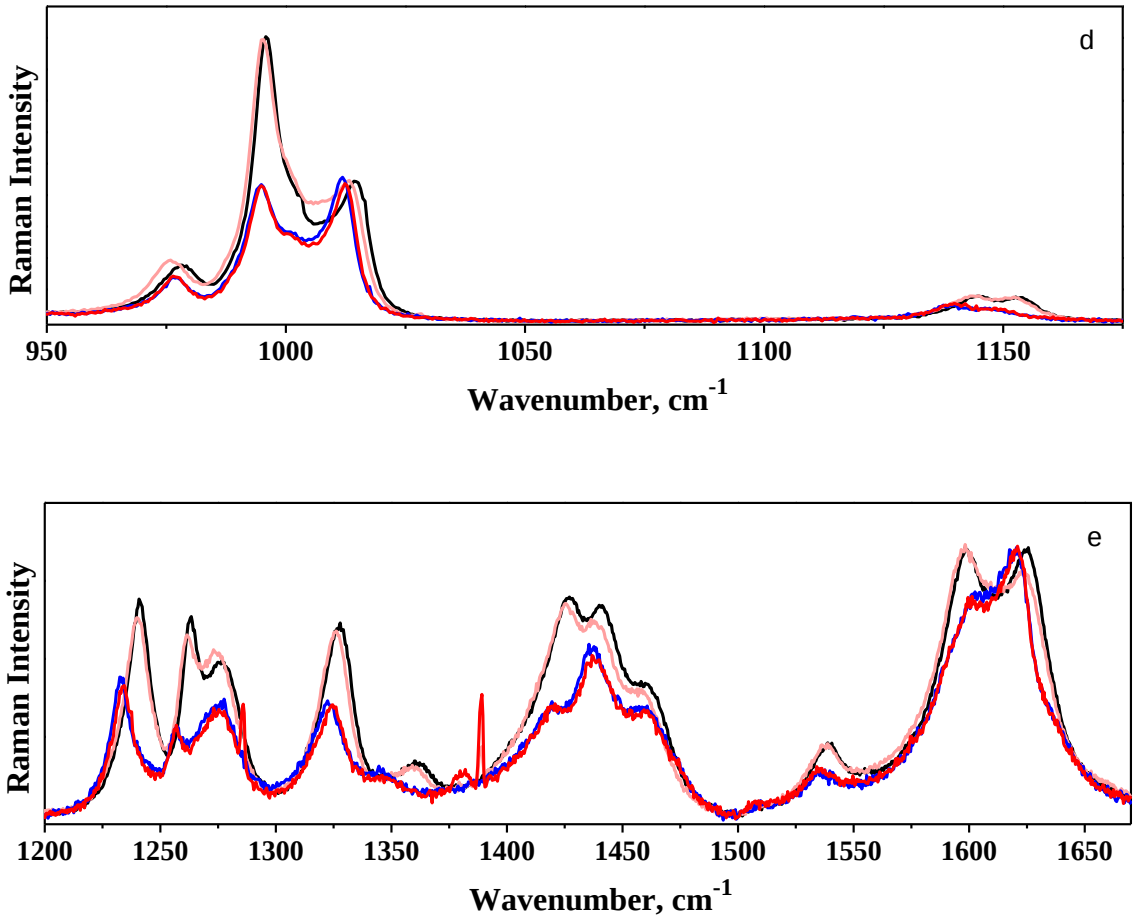

Figure 3.5 Full spectra of as-synthesized CuTDPAT (black), CuTDPAT treated with H_2O saturated CO_2 (pink), activated CuTDPAT (blue), activated CuTDPAT treated with pure CO_2 gas (red); (b-e) expanded spectral regions of the Raman full spectra in (a).

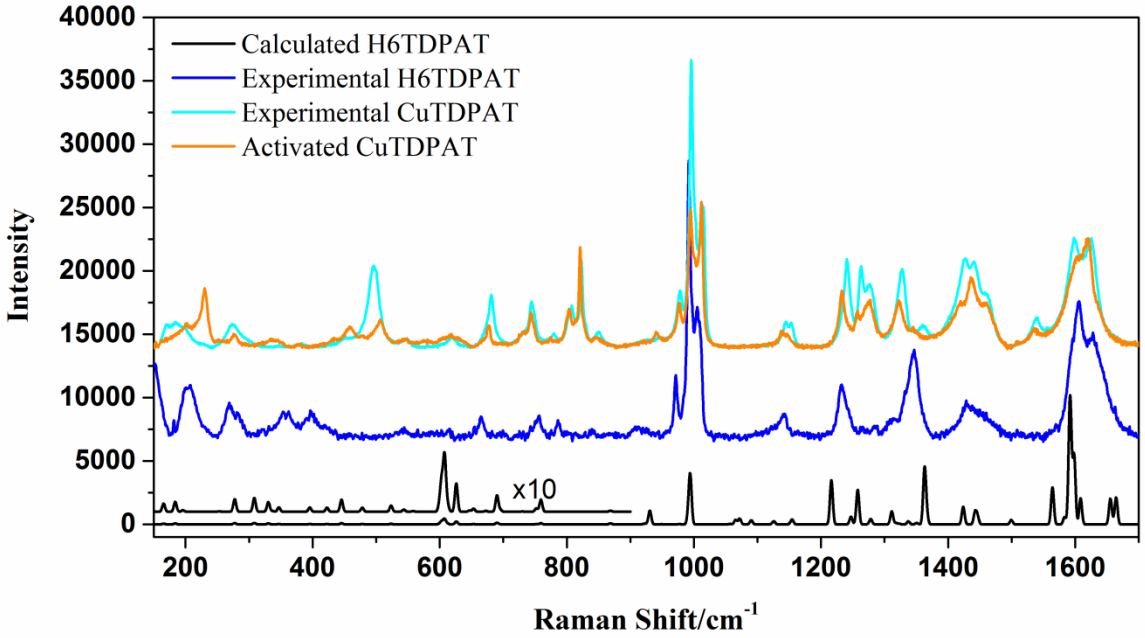

Figure 3.6 Experimental (orange) and calculated (black) Raman spectra of H_6TDPAT ligand. The calculated low frequency peaks were scaled up for better view.

Table 3.2 Experimental Raman Frequencies and Corresponding Vibrational Mode Assignments of CuTDPAT.

CuTDPAT	CuTDPAT-H_2O/CO_2	CuTDPAT-activated	CuTDPAT-CO_2	Raman assignment
171	171	sh	Sh	ν(Cu-Cu) + others
-	-	230	223	ν(Cu-Cu)
-	-	459	459	ν (Cu-O)
497	496	-	-	ν (Cu-O)
-	-	506	505	
681	681	677	677	Triazine ring distortion mode
744	744	743	743	δ Phenyl Ring
808	807	803	804	β(COO^-)
823	823	821	822	
978	976	977	977	Triazine ring breathing mode
996	995	995	995	Phenyl ring breathing mode
1015	1013	1012	1012	Triazine ring distortion mode
1241	1240	1232	1234	$\nu(C\text{-}N)_{triazine}$ + γ (N-H)
1263	1262	1257	1257	ν(C-N) + γ (N-H) + γ (C-H)
1277	1274	1275	1275	ν(C-N)
-	1286	-	1286	$\nu_s(CO_2)$
1328	1326	1323	1325	$\nu(C\text{-}C)_{ph}$ + ν(C-N) + ν(COO^-)
1362	1360	-	-	$\beta(H_2O)_{coordinated}$
-	-	-	1381	$\nu(CO_2)_{coordinated}$
-	1389	-	1389	$\nu_+(CO_2)$
1427	1425	1420	1420	γ(C-H)+γ(N-H)
1441	1441	1437	1437	γ(C-H)+γ(N-H)
1598	1597	1603	1601	$\nu(C\text{-}C)_{ph}$
1625	1624	1621	1621	ν(C-N)

Table 3.3 Experimental and calculated Raman active vibrational mode frequencies with descriptions of dominant components of the corresponding vibrational mode assignments for the H_6TDPAT ligand.

Exp. Frequency of H_6TDPAT	Calc. Frequency	Raman assignment
199.5	165	In plane Phenyl Ring tilt
207.1	184	Out plane Phenyl Ring tilt
269.1	277	δ Phenyl Ring
354.2	308	β(COOH)
396.5	330	ν(COOH)
665.7	607	δ Phenyl Ring
756.9	690	In plane δ benzene ring
786.0	759	δ Phenl Ring + $\gamma(N\text{-}H)_{amine}$
971.5	931	Triazine ring breath
992.1	994	Phenyl ring breath
1232.0	1216	$\nu(C\text{-}N)_{tirazine}$
-	1258	$\nu(C\text{-}C)_{phenyl}+\nu(C\text{-}N)+\beta(C\text{-}H)+\beta(N\text{-}H)+\beta(O\text{-}H)$
1346.8	1363	$\nu(C\text{-}C)_{phenyl}+\nu(C\text{-}N)+\beta(C\text{-}H)+\beta(N\text{-}H)+\beta(O\text{-}H)$
1428.5	1424	$\nu(C\text{-}C)_{phenyl}+\nu(C\text{-}N)+\beta(C\text{-}H)+\beta(N\text{-}H)$
-	1443	$\nu(C\text{-}C)_{phenyl}+\nu(C\text{-}N)+\beta(C\text{-}H)+\beta(N\text{-}H)$
-	1499	$\nu(C\text{-}C)_{phenyl}+\nu(C\text{-}N)+\beta(C\text{-}H)+\beta(N\text{-}H)$
1605.3	1592	$\nu(C\text{-}C)_{phenyl}$
1626.2	1608	ν(C-OH)

3.3 Discussion

3.3.1 Local metal coordination changes upon activation and CO_2 gas adsorption

The single crystal structure of Cu-TDPAT in its as-synthesized form (Figure 3.1) shows that the Cu sites have a distorted square pyramidal symmetry, excluding the weak Cu-Cu interactions spanning the paddlewheel node. Simple ligand field theory can be used to rationalize this geometry and predict the trend in geometry change upon dehydration and CO_2 interaction. In the hydrated coordination environment, the electrostatic repulsion from coordinated water molecule drives the carboxylate oxygens out of plane from the Cu(II) ions, while removal of these z-axis ligated molecules (through activation) eliminates this repulsion, predicting a structure change toward square planar. The electronic ramifications of this altered coordination geometry lead to a larger d-orbital energy level splitting through energy stabilization of the z-component *d*-orbitals and destabilization of the x,y-plane *d*-orbitals. Upon axial binding with CO_2, the distorted square pyramidal geometry along with a smaller d-orbital splitting should be only partially recovered owing to the weaker interaction compared to that of H_2O. The lowest energy region of the UV-vis diffuse reflectance spectra (Figure 3.2) contains the d-d absorption band reflecting this splitting behavior. Therefore energy shifts in this region can be interpreted as an indirect probe of metal coordination changes. Indeed, the observed spectral behavior of Cu-TDPAT upon *in situ* activation and CO_2 adsorption steps (spectral blue shift followed by partial red shift return) is consistent with the aforementioned predicted changes in metal geometry. However, this type of electronic spectroscopy inadequately measures the more subtle changes in local metal coordination environment, such as the interaction between the close lying copper sites that will

invariably influence the d-orbital splitting as well. Moreover, the overlap with other nearby absorption bands, namely LMCT bands confounds the assignment and interpretation of spectral changes. Consequently, these diffuse reflectance data are best complemented by a combination of other structurally sensitive spectroscopy measurements to build a more complete picture of the local metal coordination environment associated with the CO_2 adsorption process.

The XAS results reveal both electronic and structural changes of the Cu sites within the framework first upon transformation into the activated form and then upon exposure to CO_2 gas environment. The edge position at 8990 eV, which remains unshifted throughout the experiment, confirms the Cu^{2+} oxidation state of the metal sites. The XANES region contains a very weak pre-edge feature at 8977 eV attributed to the 1s→3d quadrupole allowed transition. The preserved low intensity of this feature indicates that the Cu sites maintain their high centrosymmetry upon changes in the axial coordination position. The edge feature at 8985 eV, which is weak in the hydrated material but becomes more pronounced upon *in situ* activation, is assigned to a metal localized 1s to 4p transition with "shakedown" contribution arising from a coupled LMCT transition. [63, 64] This feature is commonly observed in Cu(II) square planar complexes. Polarized XAS studies on oriented single crystals of Cu(II) complexes with geometries ranging from square planar to tetragonal have revealed unambiguously that this transition involves final states with metal $4p_z$ character, i.e. oriented perpendicular to the equatorial CuL_4 plane. [65] Consequently, sensitivity to the nature of metal ligation in the axial position is expected. In the absence of axial coordination, this $4p_z$ orbital can be regarded as σ-nonbonding and therefore highly localized on the metal center. Axial

ligation reduces this Cu $4p_z$ character and the resulting changes in the valence electron shielding account for the decreased intensity of this edge feature. This is consistent with the $1s \rightarrow 4p_z$ intensity increase observed upon dehydration. When the framework is loaded with CO_2, the edge feature intensity falls to an intermediate level between those observed for the activated and hydrated forms, which indicates that the CO_2 is indeed interacting with the open metal sites but not as strongly as water.

Analysis and fitting of the EXAFS region provides additional structural information of the metal coordination number and distance changes that occur during the activation and CO_2 adsorption processes. These fitting results are summarized in Table 3.1. As anticipated, the best fit of the hydrated framework EXAFS spectrum yields only minor deviations from the scattering path distances derived from the crystal structure model. The activated framework data set was best fit using a Cu coordination model that lacks the axially ligated oxygen path, indicating the removal of the coordinated water molecules from the Cu sites upon thermal treatment. EXAFS fitting shows that the Cu-$O_{carboxylate}$ bond distances remained relatively constant throughout the dehydration and adsorption processes. Rather, the distance between the pair of copper atoms that comprise the metal paddle wheel nodes of the framework appears to be more sensitive to the presence or absence of axial interaction with both H_2O and CO_2 molecules. The fits reveal a 0.1 Å reduction in Cu-Cu distance upon activation from the hydrated to dehydrated form. This change is consistent with that derived from other EXAFS work on the activation of the well-studied HKUST-1 MOF also with paddlewheel-like nodes. [39] Following exposure of the activated Cu-TDPAT framework to CO_2, the fit of the resulting spectrum yields a Cu-Cu distance of 2.63 Å, which is close to the 2.65 Å of the

hydrated framework. This change implies that CO_2 interaction with the exposed metal sites induces a return to the distorted Cu geometry similar to that of H_2O coordination. The large σ^2 values associated with the axial Cu-O paths obtained from the fits of both the hydrated and CO_2-loaded frameworks indicate a higher level of disorder as expected for these labile coordinated molecules in each case. While the EXAFS fitting results point to more subtle structural implications of the activation and CO_2 adsorption processes, the complexity of the structure and the resulting overlapping scattering paths yield a considerably congested EXAFS spectrum. The resulting uncertainties in the fits demand caution against over interpretation and prevents a truly accurate assessment of the coordination distances beyond the first shell.

Raman data collected under identical conditions provides the necessary complementary measure of the local metal structure changes incurred during the activation and CO_2 loading processes. First, the disappearance (and reappearance upon rehydration) of the mode containing the $Cu\text{-}O_{water}$ stretch at 496 cm^{-1} confirms the loss of the coordinated water molecules upon activation. Furthermore, changes in the low frequency region containing the Cu-Cu stretch are consistent with the inter-metallic distances derived from EXAFS fitting described above. Specifically, in the hydrated framework, the broad feature with maximum around 170 cm^{-1} gives way to a new peak at 230 cm^{-1} upon *in situ* activation. This peak then red shifts to 223 cm^{-1} upon CO_2 adsorption. With the dominant vibrational mode contribution to these bands assigned to a mode involving significant Cu-Cu stretch, its behavior provides further evidence that there is increased metal-metal interaction (i.e. stronger force constant for interaction and shorter Cu-Cu distance) first upon removal of axially ligated solvent molecules and then

also when loaded with CO_2. Moreover, the frequency shift of this band in the latter case indicates that the weaker Cu-CO_2 interaction causes a smaller perturbation of the Cu-Cu interaction than found in the framework with hydrated Cu sites.

3.3.2 Linker localized structure changes upon activation and CO_2 adsorption

In this section we discuss structural changes incurred by the triazine linkers within the Cu-TDPAT framework during the activation and CO_2 loading processes. EXAFS is not sensitive to longer range distances from the absorbing Cu sites, so we turn to Raman spectroscopy and the behavior of the linker localized vibrational modes for inferring more structural information about these framework components. Most of these modes, which include distortions of the triazine core, secondary amine and phenyl group, undergo some degree of red-shift in frequency (3-7 cm^{-1}) upon removal of the framework coordinated and encapsulated water molecules as outlined in Table 3.2. This most likely reflects an overall lower energy and cooperative relaxation that the linker system experiences in the process. The crystal structure of the hydrated framework reveals a slightly twisted orientation of the phenyl rings relative to the triazine core yet by DFT geometry optimization, the H_6TDPAT molecule alone has a planar structure. Therefore, the Raman behavior upon dehydration and in comparison to the H_6TDPAT reference spectrum (Figure 3.6) indicates a transition to this less strained linker geometry. When CO_2 is introduced to the activated framework, some changes in linker localized mode frequencies are observed but the subtlety of these frequency shifts compared to those involving the metal sites however, indicates that the amine site-CO_2 interaction has negligible structural effect on the linkers.

3.3.3 CO_2 interactions with dually functionalized framework

Evidence of the CO_2 interactions with the different potential binding sites within this dually functionalized framework is provided by the behavior of both the Raman active CO_2 vibrational modes and those of the framework. The characteristic CO_2 Fermi resonance peaks at 1388 and 1285 cm^{-1} are observed when the framework is exposed to CO_2 gas environment. Their unaltered frequency and sharpness indicates they are attributed to the non-interacting (or very weakly interacting) CO_2 molecules within the vicinity of the laser focus. The new band observed at 1381 cm^{-1} in this spectrum is attributed to the CO_2 molecules that are coordinated within the framework. A shift to lower frequency of the upper Fermi resonance band is expected upon coordination since the accompanying change in electron density induces symmetry breaking of the linear molecule. [67] To determine the relative contributions of the linker versus metal site coordination in producing this observed spectral change, these Raman data were compared with that obtained from a sample purged with "wet" CO_2 (i.e. the activated framework was purged with H_2O saturated CO_2 gas). In this case, H_2O, with its higher affinity for metal binding, will preferentially coordinate the open metal sites, [23] rendering only the secondary amine binding sites on the linker available for CO_2 binding. The spectrum shows only the sharp Fermi dyad peaks and a complete absence of the lower frequency peak around 1381 cm^{-1}. This observation implies that only coordination with the open metal sites strongly perturbs the electronics and symmetry of the CO_2 molecules. This approach of "poisoning" the metal sites to differentiate contributions to gas binding behavior has been successfully applied in other vibrational spectroscopy studies of MOF CO_2 adsorption. [68] The Raman spectrum of the CO_2/H_2O loaded

framework, CuTDPAT-H_2O/CO_2 exposes the interaction between CO_2 and the triazine linkers with the slight out of plane distortion found in the initial hydrated crystal structure. As shown in Figure 3.4 and outlined in Table 3.2, all the phenyl localized vibrational modes, such as the breathing mode at 996 cm^{-1} and C-C stretch mode at 1598 cm^{-1} shows negligible change after CO_2 adsorption (<1 cm^{-1}). In contrast, the triazine breathing mode at 978 cm^{-1} and the secondary amine modes involving a C-N stretching and N-H wagging motion at 1277, 1427 and 1441 cm^{-1} and all experience a red shift of at least 2 cm^{-1}. The red shift of these peaks is consistent with the lowered force constants expected for electron donating interactions with CO_2. These mode frequency shifts are not observed however when comparing the spectra of the activated versions, ie CuTDPAT-activated vs CuTDPAT-CO_2. This suggests that the amine groups serve as stronger binding sites for CO_2 in the hydrated form. One possible explanation is that the out-of-plane distortion of the triazine linker in the hydrated form of the framework may enhance its Lewis basicity. While more evidences are needed to support this hypothesis, the observations are consistent with the studies published by Zhang and co-worker. [23] Their work shows that CuTDPAT can adsorb CO_2 up to ~3 wt% from dry mixture (15:85 CO_2/N_2) verse the ~2 wt% from wet mixture (15:75:10 $CO_2/N_2/H_2O$) at 1 atm. However, the selectivity of CO_2 in the later experiment is higher over the entire pressure range from 0 to 1atm. These results can be rationalized by our observations in Raman spectra of CuTDPAT. In CuTDPAT-H_2O/CO_2 sample, open metal sites are preferentially coordinated by water molecules so that the CO_2 uptake is less than the activated CuTDPAT, in which both open metals sites and amine functional groups are avaible. While the larger shifts of amine related modes in CuTDPAT-H_2O/CO_2 Raman spectrum

imply that structural difference from the activated form may increase the accessibility or basicity of the amine groups, which can be related to the higher selectivity of CO_2 over N_2.

3.4 Conclusion

In this chapter, the structural changes and CO_2 binding interactions in an *rht*-type MOF material with multiple potential binding sites were probed by *in situ* UV-vis, XAS and Raman spectroscopy methods. The combined spectroscopic analysis revealed the reversible Cu coordination geometry changes from square pyramidal to square planar upon activation and partial recovery when CO_2 is coordinated to the metal sites. The *in situ* Raman measurements revealed subtle structural changes of the linker and metal node components as well as the Cu upon framework activation and CO_2 adsorption. These results showed that the dehydration process produced larger structural rearrangements of the framework compared to subsequent CO_2 adsorption. Raman analysis comparisons between the dry and wet CO_2 loaded frameworks provide experimental evidence for the interaction of CO_2 and both open metal and linker amine/triazine groups. These results support the concept that Lewis base functionalized linkers provide binding sites for CO_2 in addition to the open metal coordination sites but indicate that the linker distortion that occurs upon activation can influence the effectiveness of the binding interaction possibly by altering its basicity.

3.5 Materials and Methods

The materials were provided by Professor Li at Rutgers University-New Brunswick.

3.5.1 Synthesis of 2, 4, 6-tris(3, 5-dicarboxylphenylamino)-1, 3, 5-triazine (H_6TDPAT)

5-aminoisophthalic acid (7.6 g, 0.042 mol), NaOH (2.68 g, 0.067 mol), and $NaHCO_3$ (4.37 g, 0.052mol) were mixed in 70 mL H_2O. The mixture was stirred at 0 ^oC, during which cyanuric chloride (1.84 g, 0.01 mol) in 1,4-dioxane (35 mL) was added dropwise. The mixture was then stirred at 100 ^oC for 24 hours before cooling down to room temperature. The solution was adjusted to pH =2 with HCl solution and the resulting solid was collected by filtration, rinsed several times with distilled water and then hot methanol and dried to give pure H_6TDPAT (5.0 g, yield: 90%). ^1H NMR ([D6] DMSO, 300 MHz): δ=8.12 (3H), 8.47 (6H), 9.67 (3H) ppm.

3.5.2 MOF Materials.

CuTDPAT was synthesized following the previously published procedure, [24] $Cu(NO_3)_2•3H_2O$ (492 mg, 2.04 mmol), H_6TDPAT (90 mg, 0.147 mmol) were dissolved in 6 mL DMA, 6 mL DMSO, 0.3 mL H_2O and 2.7 mL HBF_4. The mixture was sonicated until homogeneous solution was achieved and then sealed in a vial and heated at 85 ^oC for 5 days. Upon cooling to room temperature, blue crystals were collected after filtration and washing with DMA for several times. The as-made Cu-TDPAT sample was immersed in methanol for 3 days to exchange the non-volatile solvents, during which the extract was decanted and replaced with fresh methanol every 3 hours and all samples

were characterized by powder X-ray diffraction to verify the crystallinity.

3.5.3 Diffuse reflectance spectroscopy

Diffuse reflectance spectra of CuTDPAT were collected using a Cary-Varian UV-visible-NIR spectrophotometer equipped with a diffuse reflectance accessory and controlled environment (vacuum/gas and temperature) solid state sample holder (Harrick Instruments). Adsorption spectra of the sample ground with KBr were collected at 10 ºC intervals from 30 ºC to 120 ºC under dynamic vacuum. After cooling the sample to room temperature adsorption data were collected upon subsequent purging with CO_2 gas until no further spectral changes were observed.

3.5.4 Raman spectroscopy

Raman spectra were collected using a 532 nm single frequency diode laser with ~ 8 mW power, a triple monochromator and a 1340 × 100 pixel liquid nitrogen-cooled CCD detector (Princeton Instruments). With 50 μm entrance slit width, the spectral resolution was < 3 cm^{-1} and peak frequency shifts of <1 cm^{-1} could be measured. The sample was deposited on a stainless steel frit and attached on a spinning sample holder in a home-made reaction chamber with optic windows. The sample was spun during the data collection process to minimize the residence time of the laser on one spot of the sample thereby avoiding excessive heating that could locally activate the framework. The Raman data of as-synthesized CuTDPAT, activated CuTDPAT and CO_2 treated CuTDPAT was measured *in-situ* in the reaction chamber.

3.5.5 X-ray Characterization

X-ray absorption data were collected at the copper K-edge (8979eV) in transmission mode at Beamline X18A at the National Synchrotron Light Source (NSLS). The X-ray white beam was monochromatized by a Si(111) monochromator and detuned by 25% to minimize the harmonic content of the beam. Copper foil was used as the reference for energy calibration. The incident beam intensity (I_0) was measured by a 15 cm ionization chamber with 100% N_2. The transmitted beam intensity (I_t) and reference (I_r) were both measured by a 30 cm ionization chamber with 60% N_2 and 40% Ar. XAS spectra were collected during heat activation, CO_2 adsorption and H_2O re-coordination using a Claussen cell reactor. This cell, which has previously been described,[43] enables simultaneous controlled temperature and gas flow environment on a sample contained within a 3mm diameter Kapton tube for *in situ* measurements. A mixture of 5 mg of CuTDPAT thoroughly ground with ~100 mg of boron nitride was packed into the sample tube to yield approximately one X-ray absorption length. Three XAS spectra of the as-synthesized sample were first collected at room temperature (~25 ºC) under continuous He gas purge. Spectra were continuously collected during heat activation of the sample (ie. gradual heating to 150 ºC under He gas flow) until no further spectral changes were observed to ensure complete dehydration. Another three scans were collected once the sample was cooled back to 25^{o}C to void the temperature effects on the Debye-Waller factor in comparison between hydrated and dehydrated sample data. To study the CO_2 adsorption process, the gas flow was switched to dry CO_2 and again the data was collected continuously to monitor the uptake of CO_2 in the framework. Finally, *in situ* XAS was used to monitor the MOF rehydration process. In this step, the same sample,

having undergone the treatments described above, was first thermally reactivated and then cooled to room temperature under dry He flow to drive off adsorbed CO_2. The reactivated sample was then purged with "wet" helium gas (ie He was sent through a bubbler containing water prior to exposure to the MOF sample) to recover the hydrated framework. XAS spectra were collected throughout this process to monitor the rehydration structure. All XAFS data were processed and analyzed using the Athena and Artemis programs of the IFEFFIT package based on FEFF 6.[44, 45]

The crystallinity of this MOF sample was monitored by synchrotron PXRD (Figure 3.7) immediately before and after each adsorption/desorption step described above to show that the crystallinity and long range order were preserved throughout the process. The diffraction patterns of CuTDPAT were recorded on a 2D detector at X18A of NSLS in Brookhaven National Lab. All the measurements were operated at room temperature using 10keV X-ray right after the corresponding XAFS scans.

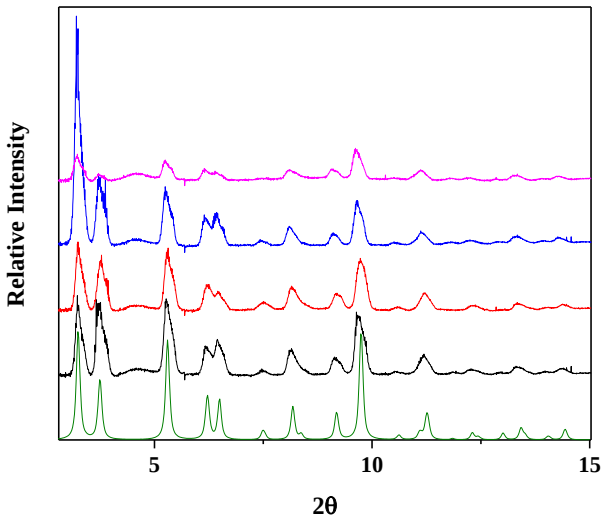

Figure 3.7 PXRD patterns of CuTDPAT before and after activation, upon CO_2 loading and rehydration. Bottom trace: theoretical PXRD pattern.

3.5.6 DFT computational methods

The geometry optimization and vibrational modes of TDPAT was calculated using the Gaussian 03 program package [68] at the density functional theory (DFT) level with Beck's three parameter functional and Lee-Yang-Parr functional (B3LYP) method. 6-31G basis set was used. A summary of the calculated frequencies for the most Raman active vibrational modes is provided in Table 3.3. The vibrational mode anharmonicities were compensated using of a scaling factor of 0.96 in reporting their frequencies.

3.6 Reference

1 H. Furukawa, K. E. Cordova, M. O'Keeffe and O. M. Yaghi, *Science*, 2013, **341**, 6149.

2 C. Wang, D. Liu and W. Lin,J. Am. Chem. Soc., 2013, 135, 13222–13234.

3 M. L. Foo, R. Matsuda and S. Kitagawa,Chem. Mater., 2014, 26, 310–322.

4 J. Lee, O. K. Farha, J. Roberts, K. A. Scheidt, S. T. Nguyen and J. T. Hupp, *Chem. Soc. Rev.*, 2009, **38**, 1450–1459.

5 J. Liu, P. K. Thallapally, B. P. McGrail, D. R. Brown and J. Liu, *Chem. Soc. Rev.*, 2012, **41**, 2308–2322.

6 K. Sumida, D. L. Rogow, J. A. Mason, T. M. McDonald, E. D. Bloch, Z. R. Herm, T.-H. Bae and J. R. Long, *Chem. Rev.*, 2012, **112**, 724–781.

7 H. Wu, Q. Gong, D. H. Olson and J. Li, *Chem. Rev.*, 2012, **112**, 836–868.

8 Y. Cui, Y. Yue, G. Qian and B. Chen, *Chem. Rev.*, 2012, **112**, 1126.

9 Z. Hu, B. J. Deibert and J. Li, *Chem. Soc. Rev.*, 2014, **43**, 5815–5840.

10 N. L. Rosi, J. Kim, M. Eddaoudi, B. Chen, M. O'Keeffe and O. M. Yaghi, *J. Am. Chem. Soc.*, 2005, **127**, 1504–1518.

11 P. D. C. Dietzel, Y. Morita, R. Blom and H. Fjellv˚ag, *Angew Chem., Int. Ed.*, 2005, **44**, 6354–6358.

12 P. D. C. Dietzel, R. E. Johnsen, H. Fjellvag, S. Bordiga, E. Groppo, S. Chavan and R. Blom, *Chem. Commun.*, 2008, 5125–5127.

13 S. R. Caskey, A. G. Wong-Foy and A. J. Matzger, *J. Am. Chem. Soc.*, 2008, **130**, 10870–10871.

14 D. Britt, H. Furukawa, B. Wang, T. G. Glover and O. M. Yaghi, *Proc. Natl. Acad. Sci. U. S. A.*, 2009, **106**, 20637–20640.

15 S. Couck, J. F. M. Denayer, G. V. Baron, T. R´emy, J. Gascon and F. Kapteijn, *J. Am. Chem. Soc.*, 2009, **131**, 6326–6327.

16 J. An, S. J. Geib and N. L. Rosi, *J. Am. Chem. Soc.*, 2009, **132**, 38–39.

17 H. Xu, Y. He, Z. Zhang, S. Xiang, J. Cai, Y. Cui, Y. Yang, G. Qian and B. Chen, *J. Mater. Chem. A*, 2013, **1**, 77–81.

18 X. Rao, J. Cai, J. Yu, Y. He, C. Wu, W. Zhou, T. Yildirim, B. Chen and G. Qian, *Chem. Commun.*, 2013, **49**, 6719–6721.

19 N. Nijem, P. Canepa, L. Kong, H. Wu, J. Li, T. Thonhauser and Y. J. Chabal, *J. Phys.: Condens. Matter.*, 2012, **24**, 424203.

20 L.-C. Lin, J. Kim, X. Kong, E. Scott, T. M. McDonald, J. R. Long, J. A. Reimer and B. Smit, *Angew. Chem., Int. Ed.*, 2013, **52**, 4410–4413.

21 N. Planas, A. L. Dzubak, R. Poloni, L.-C. Lin, A. McManus, T. M. McDonald, J. B. Neaton, J. R. Long, B. Smit and L. Gagliardi, *J. Am. Chem. Soc.*, 2013, **135**, 7402–7405.

22 T. Pham, K. A. Forrest, J. Eckert, P. A. Georgiev, A. Mullen, R. Luebke, A. J. Cairns, Y. Belmabkhout, J. F. Eubank, K. McLaughlin, W. Lohstroh, M. Eddaoudi and B. Space, *J. Phys. Chem. C*, 2014, **118**, 439–456.

23 Z. Zhang, Z. Li and J. Li, *Langmuir*, 2012, **28**, 12122–12133.

24 B. Li, Z. Zhang, Y. Li, K. Yao, Y. Zhu, Z. Deng, F. Yang, X. Zhou, G. Li, H. Wu, N. Nijem, Y. J. Chabal, Z. Lai, Y. Han, Z. Shi, S. Feng and J. Li, *Angew. Chem., Int. Ed.*, 2012, **51**, 1412–1415.

25 R. Luebke, J. F. Eubank, A. J. Cairns, Y. Belmabkhout, L. Wojtas and M. Eddaoudi, *Chem. Commun.*, 2012, **48**, 1455–1457.

26 D. Zhao, D. Yuan, D. Sun and H.-C. Zhou, *J. Am. Chem. Soc.*, 2009,**131**, 9186–9188.

27 J. F. Eubank, F. Nouar, R. Luebke, A. J. Cairns, L. Wojtas, M. Alkordi, T. Bousquet, M. R. Hight, J. Eckert, J. P. Embs, P. A. Georgiev and M. Eddaoudi, *Angew. Chem., Int. Ed.*, 2012, **51**, 10099–10103.

28 O. K. Farha, A. Özgür Yazaydın, I. Eryazici, C. D. Malliakas, B. G. Hauser, M. G. Kanatzidis, S. T. Nguyen, R. Q. Snurr and J. T. Hupp, *Nat. Chem.*, 2010, **2**, 944–948.

29 F. Nouar, J. F. Eubank, T. Bousquet, L. Wojtas, M. J. Zaworotko and M. Eddaoudi, *J. Am. Chem. Soc.*, 2008, **130**, 1833–1835.

30 B. Zheng, J. Bai, J. Duan, L. Wojtas and M. J. Zaworotko, *J. Am. Chem. Soc.*, 2011, **133**, 748–751.

31 Y. Yan, S. Yang, A. J. Blake, W. Lewis, E. Poirier, S. A. Barnett, N. R. Champness and M. Schroder, *Chem. Commun.*, 2011, **47**, 9995–9997.

32 Y. Yan, M. Suyetin, E. Bichoutskaia, A. J. Blake, D. R. Allan, S. A. Barnett and M. Schroder, *Chem. Sci.*, 2013, **4**, 1731–1736.

33 G. Agostini, C. Lamberti, L. Palin, M. Milanesio, N. Danilina, B. Xu, M. Janousch and J. A. van Bokhoven, *J. Am. Chem. Soc.*, 2009, **132**, 667–678.

34 D. E. Doronkin, M. Casapu, T. G¨ unter, O. Müller, R. Frahm and J.-D. Grunwaldt, *J. Phys. Chem. C*, 2014, **118**, 10204–10212.

35 D. Grandjean, A. M. Beale, A. V. Petukhov and B. M. Weckhuysen, *J. Am. Chem. Soc.*, 2005, **127**, 14454–14465.

36 I. J. Drake, Y. Zhang, M. K. Gilles, C. N. Teris Liu, P. Nachimuthu, R. C. C. Perera, H. Wakita and A. T. Bell, *J. Phys. Chem. B*, 2006, **110**, 11665–11676.

37 G. Plazenet, E. Payen, J. Lynch and B. Rebours, *J. Phys. Chem. B*, 2002, **106**, 7013–7028.

38 S. Bordiga, F. Bonino, K. P. Lillerud and C. Lamberti, *Chem. Soc. Rev.*, 2010, **39**, 4885–4927.

39 C. Prestipino, L. Regli, J. G. Vitillo, F. Bonino, A. Damin, C. Lamberti, A. Zecchina, P. L. Solari, K. O. Kongshaug and S. Bordiga, *Chem. Mater.*, 2006, **18**, 1337–1346.

40 F. Bonino, S. Chavan, J. G. Vitillo, E. Groppo, G. Agostini, C. Lamberti, P. D. C. Dietzel, C. Prestipino and S. Bordiga, *Chem. Mater.*, 2008, **20**, 4957–4968.

41 Y. Chen, J. Zhang, J. Li and J. V. Lockard, *J. Phys. Chem. C*, 2013, **117**, 20068–20077.

42 W. S. Drisdell, R. Poloni, T. M. McDonald, J. R. Long, B. Smit, J. B. Neaton, D. Prendergast and J. B. Kortright, *J. Am. Chem. Soc.*, 2013, **135**, 18183–18190.

43 S. Chavan, J. G. Vitillo, E. Groppo, F. Bonino, C. Lamberti, P. D. C. Dietzel and S. Bordiga, *J. Phys. Chem. C*, 2009, **113**, 3292–3299.

44 N. Nijem, P. Thissen, Y. Yao, R. C. Longo, K. Roodenko, H. Wu, Y. Zhao, K. Cho, J. Li, D. C. Langreth and Y. J. Chabal, *J. Am. Chem. Soc.*, 2011, **133**, 12849–12857.

45 J. Seo, C. Bonneau, R. Matsuda, M. Takata and S. Kitagawa, *J. Am. Chem. Soc.*, 2011, **133**, 9005–9013.

46 S. Chavan, J. G. Vitillo, C. Larabi, E. Alessandra Quadrelli, P. D. C. Dietzel and S. Bordiga, *Microporous Mesoporous Mater.*, 2012, **157**, 56–61.

47 N. Nijem, H. Wu, P. Canepa, A. Marti, K. J. Balkus, T. Thonhauser, J. Li and Y. J. Chabal, *J. Am. Chem. Soc.*, 2012,**134**, 15201–15204.

48 K. Tan, N. Nijem, P. Canepa, Q. Gong, J. Li, T. Thonhauser and Y. J. Chabal, *Chem. Mater.*, 2012, **24**, 3153–3167.

49 Y. Yao, N. Nijem, J. Li, Y. J. Chabal, D. C. Langreth and T. Thonhauser,Phys. Rev. B: Condens. *Matter Mater. Phys.*, 2012, **85**, 064302.

50 H. Liu, Y. Zhao, Z. Zhang, N. Nijem, Y. J. Chabal, X. Peng, H. Zeng and J. Li, *Chem.–Asian J.*, 2013, **8**, 778–785.

51 M. I. Breeze, G. Clet, B. C. Campo, A. Vimont, M. Daturi, J.-M. Grenèche, A. J. Dent, F. Millange and R. I. Walton, *Inorg. Chem.*, 2013, **52**, 8171–8182.

52 L. Hamon, P. L. Llewellyn, T. Devic, A. Ghoufi, G. Clet, V. Guillerm, G. D. Pirngruber, G. Maurin, C. Serre, G. Driver, W. v. Beek, E. Jolimaître, A. Vimont, M. Daturi and G. F´erey, *J. Am. Chem. Soc.*, 2009, **131**, 17490–17499.

53 H. Leclerc, T. Devic, S. Devautour-Vinot, P. Bazin, N. Audebrand, G. Férey, M. Daturi, A. Vimont and G. Clet, *J. Phys. Chem. C*, 2011, **115**, 19828–19840.

54 P. J. Chupas, M. F. Ciraolo, J. C. Hanson and C. P. Grey, *J. Am. Chem. Soc.*, 2001, **123**, 1694–1702.

55 B. Ravel and M. Newville, *J. Synchrotron Radiat.*, 2005, **12**, 537–541.

56 J. J. Rehr and R. C. Albers, *Rev. Mod. Phys.*, 2000, **72**, 621–654.

57 K. Nakamoto, *Infrared and Raman Spectra of Inorganic and Coordination Compounds, Part B*, John Wiley & Sons, Inc, 6th edition, 2009.

58 P. J. Larkin, M. P. Makowski and N. B. Colthup, *Spectrochim. Acta, Part A*, 1999, **55**, 1011–1020.

59 W. Sawodny, K. Niedenzu and J. W. Dawson, *J. Chem. Phys.*, 1966, **45**, 3155–3156.

60 G. Socrates, *Infrared and Raman Characteristic Group Frequencies*, John Wiley & Sons, Ltd, 3rd edition, 2001.

61 M. K. Marchewka, *Bull. Korean Chem. Soc.*, 2004, **25**, 466–470.

62 D. L. Phillips, C.-M. Che, K. H. Leung, Z. Mao and M.-C. Tse, *Coord. Chem. Rev.*, 2005, **249**, 1476–1490.

63 S. E. Shadle, J. E. Penner-Hahn, H. J. Schugar, B. Hedman, K. O. Hodgson and E. I. Solomon, *J. Am. Chem. Soc.*, 1993, **115**, 767–776.

64 L. S. Kau, D. J. Spira-Solomon, J. E. Penner-Hahn, K. O. Hodgson and E. I. Solomon, *J. Am. Chem. Soc.*, 1987, **109**, 6433–6442.

65 T. A. Smith, J. E. Penner-Hahn, M. A. Berding, S. Doniach and K. O. Hodgson, *J. Am. Chem. Soc.*, 1985, **107**, 5945–5955.

66 F. Salles, G. Maurin, C. Serre, P. L. Llewellyn, C. Kn¨ofel, H. J. Choi, Y. Filinchuk, L. Oliviero, A. Vimont, J. R. Long and G. r. F´erey, *J. Am. Chem. Soc.*, 2010, **132**, 13782–13788.

67 H. Forster and M. Schumann, *J. Chem. Soc., Faraday Trans. 1*, 1989, **85**, 1149–1158.

68 P. L. Llewellyn, S. Bourrelly, C. Serre, A. Vimont, M. Daturi, L. Hamon, G. De Weireld, J.-S. Chang, D.-Y. Hong, Y. Kyu Hwang, S. Hwa Jhung and G. Férey, *Langmuir*, 2008, **24**, 7245–7250.

68 M. J. Frisch, G. W. Trucks, H. B. Schlegel, G. E. Scuseria, M. A. Robb, J. R. Cheeseman, G. Scalmani, V. Barone, B. Mennucci, G. A. Petersson, H. Nakatsuji,M. Caricato, X. Li, H. P. Hratchian, A. F. Izmaylov, J. Bloino, G. Zheng, J. L. Sonnenberg, M. Hada, M. Ehara, K. Toyota, R. Fukuda, J. Hasegawa, M. Ishida, T. Nakajima, Y. Honda, O. Kitao, H. Nakai, T. Vreven, J. A. Montgomery, Jr., J. E. Peralta, F. Ogliaro, M. Bearpark, J. J. Heyd, E. Brothers, K. N. Kudin, V. N. Staroverov, R. Kobayashi, J.

Normand, K. Raghavachari, A. Rendell, J. C. Burant, S. S. Iyengar, J. Tomasi, M. Cossi, N. Rega, J. M. Millam, M. Klene, J. E. Knox, J. B. Cross, V. Bakken, C. Adamo, J. Jaramillo, R. Gomperts, R. E. Stratmann, O. Yazyev, A. J. Austin, R. Cammi, C. Pomelli, J. W. Ochterski, R. L. Martin, K. Morokuma, V. G. Zakrzewski, G. A. Voth, P. Salvador, J. J. Dannenberg, S. Dapprich, A. D. Daniels, Ö. Farkas, J. B. Foresman, J. V. Ortiz, J. Cioslowski, and D. J. Fox; Gaussian Inc.: Wallingford, CT, 2010.

Chapter 4 *In-situ* Raman studies of activation and CO_2 gas adsorption in a series of iso-structural M/DOBDC frameworks

4.1 Introduction

Materials with enhanced physisorption behavior have attracted intensive attention for fuel gas storage and selective separation of gas mixtures. [1-3] The relatively low regeneration energy requirements of physisorption can help reduce the operation cost significantly, but the low capacity usually limits their applications. [4] Metal-Organic frameworks (MOF) seem capable to overcome this shortcoming thanks to their huge surface areas and versatile internal chemical environment. Among the thousands of newly developed MOF materials, M/DOBDC (M = Mg, Ni, Co, Zn; DOBDC = 2,5-dioxido-1,4-benzenedicarboxylate) MOFs (also known as CPO-27 [5, 6] or MOF-74. [7, 8]) have demonstrated extraordinary capacity for CO_2 adsorption, [3] as well as H_2, propylene and other fuel gases. [1] Each of these materials consists of M(II) ions connected by DOBDC linker to form a 3D porous honeycomb-like hexagonal structure with 1D channels. Each metal ion in these frameworks coordinates to six oxygens in an octahedral symmetry, in which five oxygens come from carboxylate ligand and one from a coordinated solvent molecule. The solvent molecule can be removed upon elevated temperature or vacuum to expose open metal sites. Despite the relative low surface area of M/DOBDC frameworks, the high concentration of open metal sites distributed along the internal face of M/DOBDC frameworks gives them ultra high capacity and selectivity of various gases at low pressure (Figure 4.1). Interestingly, although all M/DOBDC family members show superior gas capacity compared with most of other frameworks under low pressure, [3]

M/DOBDC frameworks with different metals exhibit dramatic differences in performance when compare to each other. In the study in 2008, Caskey *et al* measured the CO_2 uptake of the four best performing M/DOBDC under low (0.1 atm) and atmospheric pressure. [9] The result shows Mg/DOBDC hosts ~12 CO_2 molecules per unit cell under 0.1 atm, while Co/DOBDC and Ni/DOBDC hosts ~7, respectively. And Zn/DOBDC has a significant lower uptake of 4 molecules per unit cell. In another study the next year, Yazaydin and coworkers compared this M/DOBDC series with 10 other MOFs under 0.1 bar (Figure 4.2). [10] The result also shows a considerable difference of CO_2 uptake in the isostructure M/DOBDC frameworks. These uptakes are 0.721, 0.436, 0.638 and 0.213 molecules of CO_2 per metal site for Mg, Co, Ni and Zn. The reason for these significantly different uptakes and the order with respect to the metal is not entirely clear. Caskey proposed that the ionic character of Mg-O bond may be responsible for the ultra high capacity of CO_2 in Mg/DOBDC. Incomplete activation, pore blockage and/or partial collapse of the Zn/DOBDC structure upon activationwas hypothesized to play a role in the significantly lower CO_2 uptake in that framework, but the crystallographic characterization does not seem to support that argument. The full picture could be much more complicated than merely one or two factors, thus, local coordination environment and framework flexibility, including the relative accessibility of the metal sites after the activation process should be considered for a better interpretation.

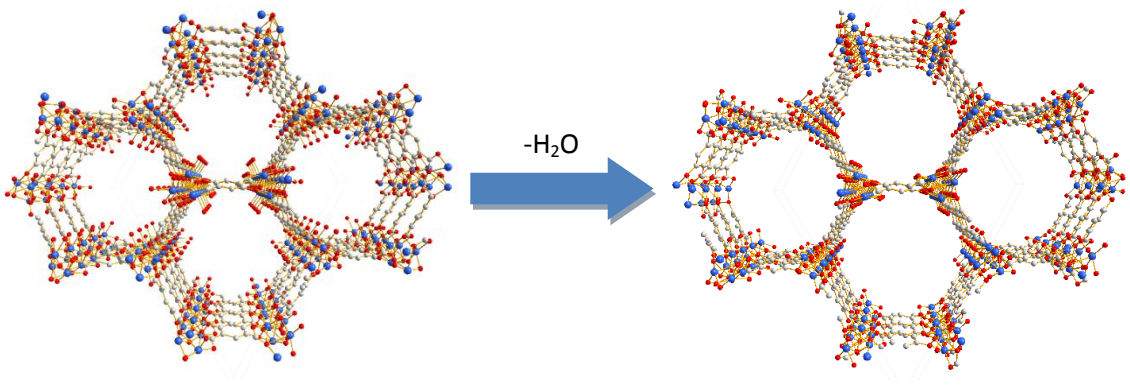

Figure 4.1 Illustration of M/DOBDC frameworks. M (blue), oxygen (red) and carbon (grey).

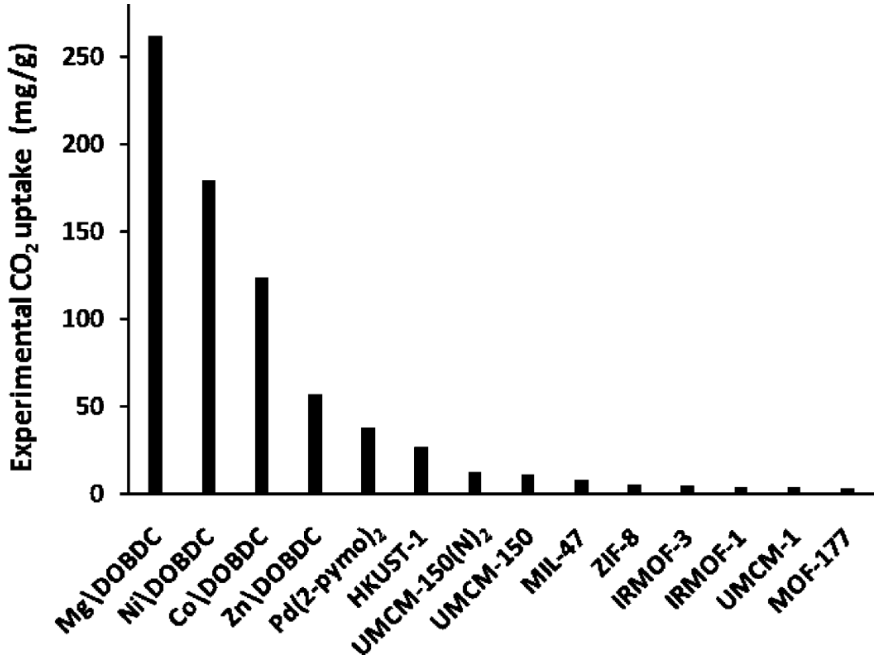

Figure 4.2 Experimental CO_2 uptake in 14 different MOFs at 0.1 bar. Reprinted with permission from *J. Am. Chem. Soc.*, 131:18198-18199. Copyright 2009 American Chemical Society

So far, XRD, [11-13] vibrational spectroscopy, [13-15] neutron powder diffraction (NPD), [16] XAS, [17-20] and theoretical simulation [15, 20-23] studies have been conducted to explain the adsorption behavior of M/DOBDC. Most of these investigations focus on individual M/DOBDC frameworks and do not include systematic comparisons between

each of the M/DOBDC family members. In this chapter, a combination of XRD, *in-situ* diffuse reflectance and *in-situ* Raman spectroscopy methods is used to investigate the subtle structural changes in the series of M/DOBDC frameworks with different metal nodes upon activation and CO_2 adsorption.

4.2 Result

4.2.1 X-ray diffraction

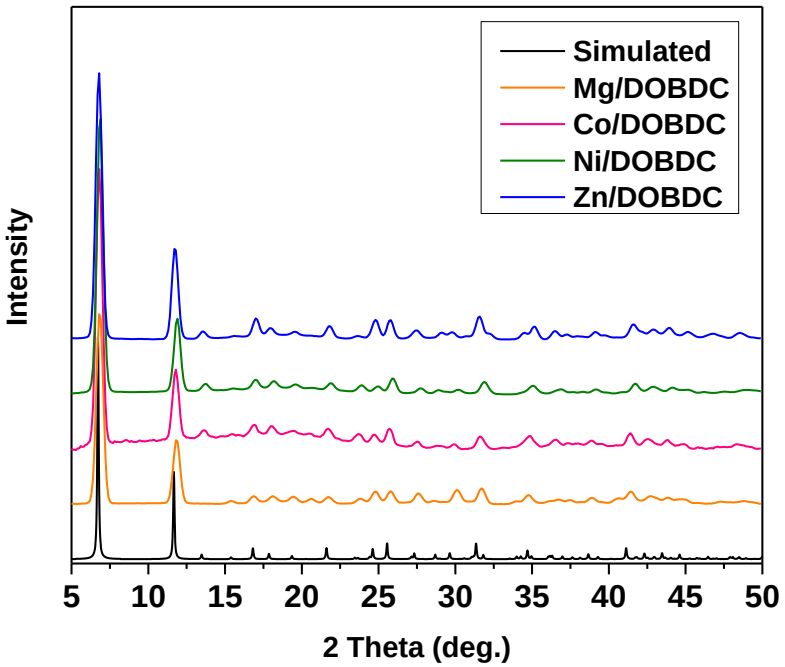

Figure 4.3 The PXRD patterns of simulated Zn/DOBDC(black), Mg/DOBDC (orange), Co/DOBDC (pink), Ni/DOBDC (green) and Zn/DOBDC (blue)

The PXRD patterns of samples used in this experiment are shown in Figure 4.3. These PXRD data were compared to a PXRD pattern simulated from Zn/DOBDC single crystal XRD data [11] to verify that they have the structure of M/DOBDC. After the *in-situ* Raman study, the PXRD data was collected from the same sample again to exam the structure and crystallinity. As shown in Figure 4.4, the results show that the crystal structures of all four samples after heat and CO_2 treatment are consistent with the as-

synthesized samples. No significant change of signal intensity also indicates that little loss of crystallinity occurs during the experiment.

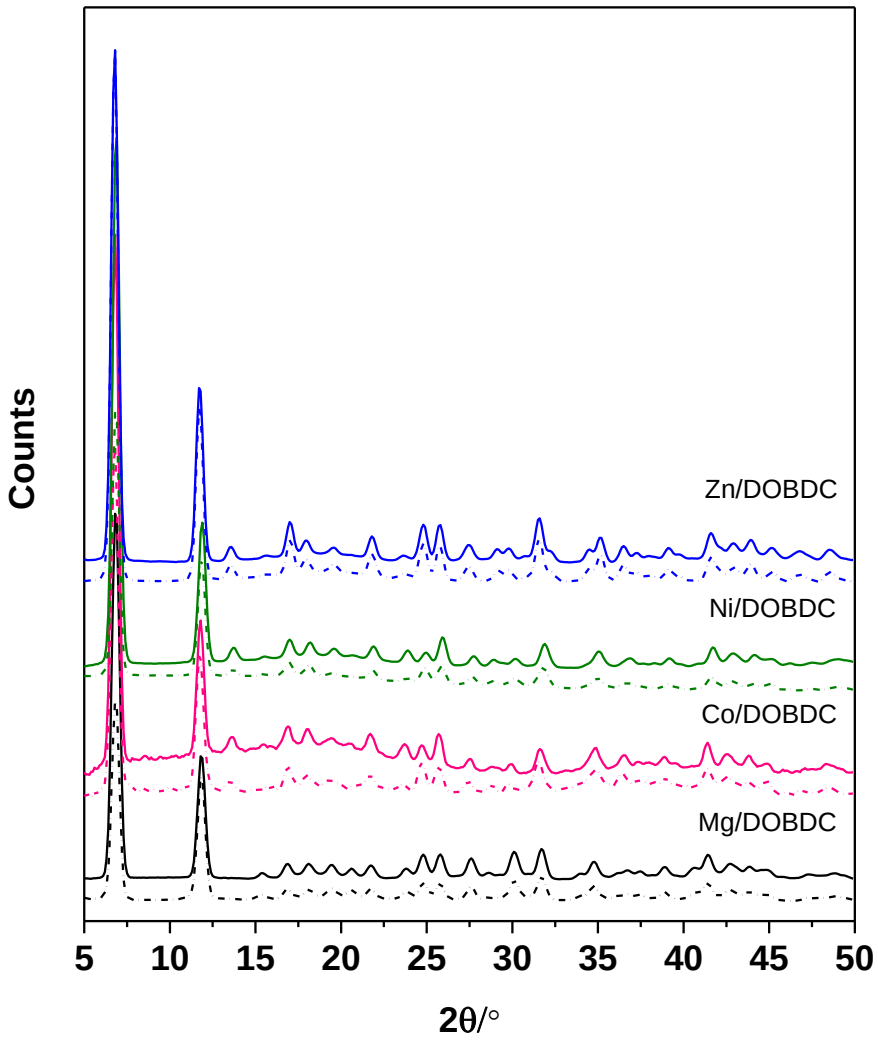

Figure 4.4 The PXRD pattern of M/DOBDC frameworks before (solid line) and after activation/CO_2 adsorption (dashed line)

4.2.2 UV-vis diffuse reflectance spectroscopy

The diffuse reflectance spectra of M/DOBDC obtained during activation and CO_2 treatment are shown in Figure 4.5. Mg/DOBDC (Figure 4.5a) and Zn/DOBDC (Figure 4.5d) shows no signal in the visible region as expected due to the absence of d-d transitions. In all cases the absorption from the ligand (λ_{max} ~ 400 nm) shows little change since the removal of metal coordinated water has negligible impact on the electronic state of the ligands.

Diffuse reflectance spectra of Co/DOBDC are shown in Figure 4.5c. Given the tetragonally distorted octahedral approximate coordination for the high spin Co(II) sites in the as-synthesized (hydrated) framework, the two absorption bands at 18348 cm^{-1} and below 8000 cm^{-1} for can be assigned to the $^4A_2(F) \rightarrow {}^4E(P)$ and $^4A_2(F) \rightarrow {}^4E(F)$ ligand field state transitions,[24-26] respectively. The former band red shifts to 17574 cm^{-1} upon activation and then partially returns to 17920 cm^{-1} after CO_2 adsorption. The latter band is not complete due to the limitation of instrument so that it will not be discussed in this chapter. The band that appears at 13986 cm^{-1} after activation is assigned to a $^4E(F) \rightarrow {}^4B_1(F)$ transition and then blue shifted to 14265 cm^{-1} after CO_2 adsorption. This band is probably buried under the strong transition to $^4A_2(P)$ in the as-synthesized sample as it is well documented to be a weak transition in pseudo octahedral geometries. [25] The increased intensity of this band is due to the symmetry change to five coordinate C_{4v} upon activation.

The spectrum of the as-synthesized Ni/DOBDC shows four bands at 20280, 15200, 13620 and 9337 cm^{-1}, which can be assigned to ligand field state transitions under

C_{4v} symmetry. The shoulder peak at 20280 likely has contributions from the $^3B_1 \rightarrow {}^3E(P)$ and $^3B_1 \rightarrow {}^3A_2(P)$ transitions. [27] This band blue shifts upon activation and becomes more overlapped with the ligand absorption band. The absorption band with double maxima at 15200 and 13620 nm is most likely dominated by a $^3B_1 \rightarrow {}^3E$ transition with significant contribution from the transition to the the close lining spin forbidden $^1A_1$ state that gains intensity as a result of spin-orbit coupling. [28] The two peaks merge into one maximum at 14472 upon activation and then after CO_2 treatment, the band splits once again to two descernable features with maxima at14930 and 13333 cm^{-1}. The 9337 cm^{-1} band is assigned to the transition to $^3B_2$ state. [24, 27] This band shifts to 9660 cm^{-1} upon framework activation and returns to nearly the same peak position (9354 cm^{-1}) after CO_2 adsorption.

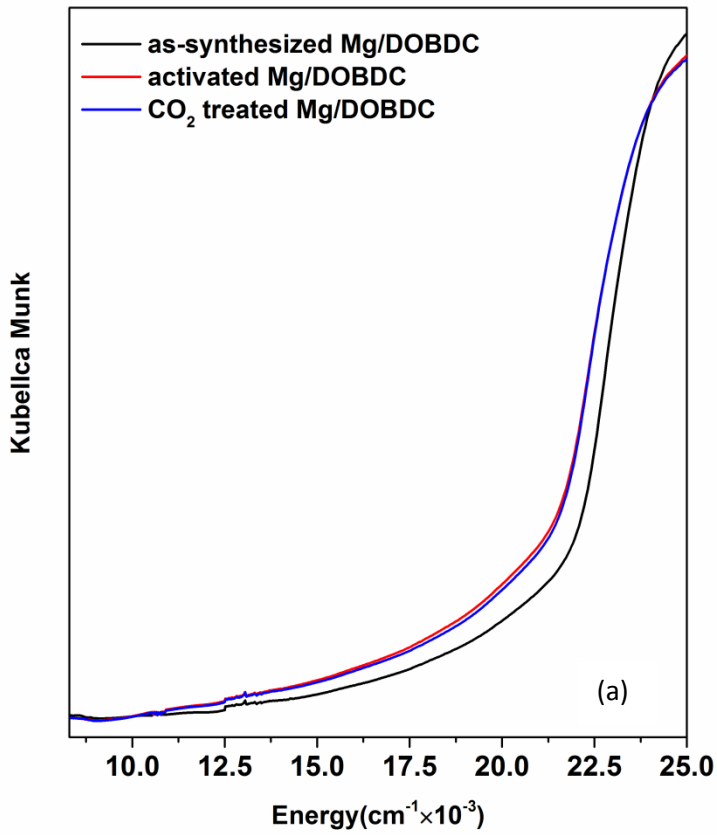

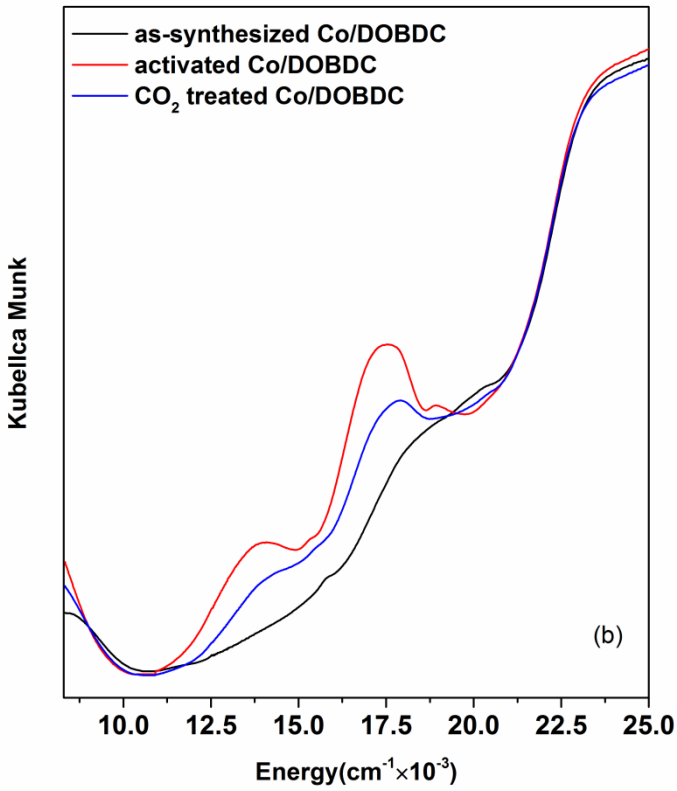
as-synthesized Co/DOBDC
activated Co/DOBDC
CO2 treated Co/DOBDC
Kubellca Munk
(b)
10.0
12.5
15.0
17.5
20.0
22.5
25.0
Energy(cm-1×10-3)

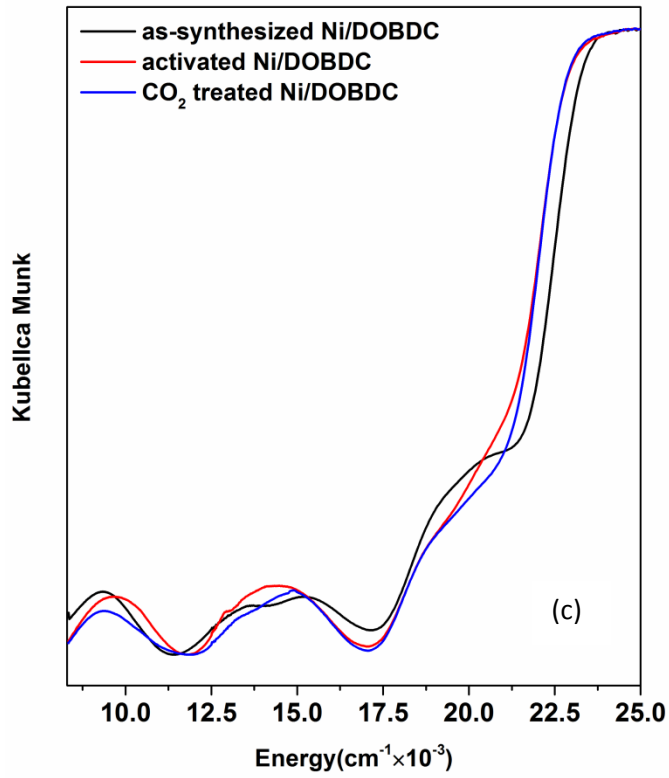
as-synthesized Ni/DOBDC
activated Ni/DOBDC
CO2 treated Ni/DOBDC
Kubellca Munk
(c)
10.0
12.5
15.0
17.5
20.0
22.5
25.0
Energy(cm-1×10-3)

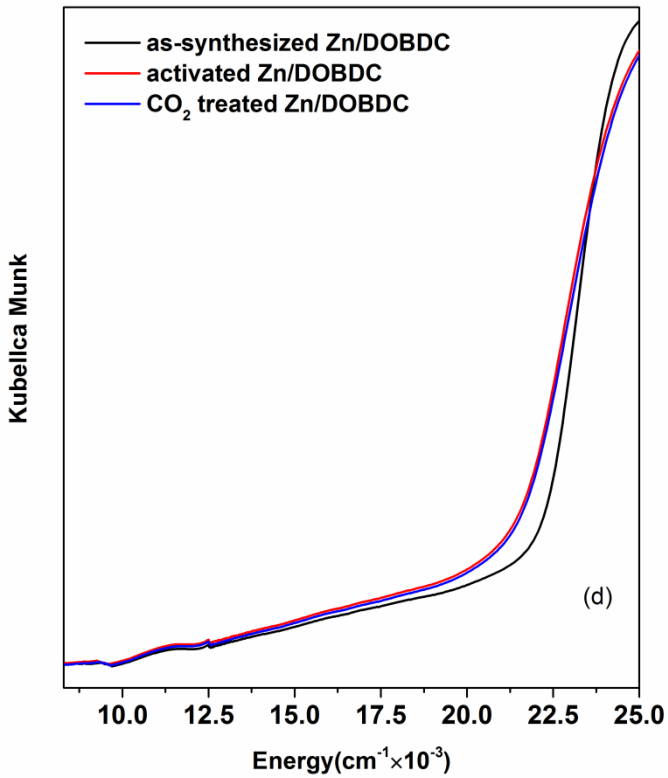

Figure 4.5 Diffuse reflectance spectra of M/DOBDC frameworks.

4.2.3 Raman Spectroscopy

A comparison of the Raman spectra of the four frameworks is shown in Figure 4.6. Raman spectra collected upon activation and CO_2 adsorption of M/DOBDC frameworks are shown in Figure 4.7 and Figure 4.8. The observed vibrational frequencies with the corresponding mode assignments are listed in Table 4.1. The assignments were determined by comparison with literature values [29-36] and those measured from H_4DOBDC ligand alone which were in turn supplemented by computed theoretical vibrational modes frequencies. The reference spectrum is illustrated in Figure 4.9 and a summary of the experimental frequency values of H_4DOBDC and corresponding DFT calculated vibrational modes are provided in Table 4.2. All four samples were activated

and again exposed to water vapor at room temperature. This process was monitored by Raman and the final resulting hydrated sample generated almost identical Raman spectra as the as-synthesized hydrated samples, illustrating the reversibility of the hydration/dehydration process in these frameworks. The comparisons between as-synthesized samples and samples recovered after the *in-situ* experiments are shown in Figure 4.10 which indicates the change observed in the experiment are reversible. Both XRD and Raman data show that no permanent structure change or framework damage occurred during the experiment.

Due to the similarity of Raman spectra of all samples, the description below is the general assignment of all four frameworks. One should be aware that the assignments of some low frequency region (100 cm^{-1} to 400 cm^{-1}) are derived primarily from literature values. Some ambiguity exists due to the potential solid state effects. The weak peaks from 100 cm^{-1} to 250 cm^{-1} are assigned to O-M-O symmetric and asymmetric bending modes. The peaks in the region 375 cm^{-1} to 410 cm^{-1} are assigned to M-O stretching. The strong peaks around ~560 cm^{-1} are the bending mode of carboxylate group. The sharp peaks at ~820 cm^{-1} are assignment to the benzene breathing mode. The intense peaks in the region of 1260-1290 cm^{-1} is assigned to the hydroxyl C-O stretch mode. The peak at ~1420 cm^{-1} and 1500 cm^{-1} are assigned to the symmetric and asymmetric stretch mode of coordinated carboxylate groups, respectively. The broad peaks in the 1550 cm^{-1} to 1580 cm^{-1} region is the C-C stretch mode of the benzene ring and the last set of peaks at ~1617 cm^{-1} is the C=O stretch mode. Notably, two small but distinct peaks at 1389 cm^{-1} and 1381 cm^{-1} (Figure 4.11), which only appear upon CO_2 treatment are assigned to CO_2 localized vibrations. The first one is assigned to the higher energy Femi dyad peak of free

CO_2 (the other one of the pair which would be anticipated at 1285 cm^{-1}, is obscured by one of the intense linker band at 1284 $cm^{-1}$and therefore not observed). The peak at 1381 cm^{-1} can be assigned to the same vibrational mode but red shifted due to the break of CO_2 symmetry. [37, 38] Mg/DOBDC shows two extra peaks at 310 and 1660 cm^{-1} which disappear after activation. The origin of the two peaks is not clear but may be related to the local vibration of coordinated H_2O.

Table 4.1 Experimental Raman frequencies (cm^{-1}) and corresponding vibrational mode assignment. The shift after activation is shown in parentheses.

Mg/DOBDC	**Co/DOBDC**	**Ni/DOBDC**	**Zn/DOBDC**	Raman assignment
137 (-22)	137 (-14)	153 (-15)	142 (-33)	β (O-M-O)
229 (-16)	239 (-21)	269 (-11)	219 (-16)	β (O-M-O)
410 (+14)	391 (+20)	410 (+8)	379 (+34)	ν(M-O)
562 (+6)	563 (+9)	570 (+6)	559 (+16)	$\beta\ (COO)_{carboxylate}$
821 (-3)	818 (0)	827 (0)	820 (-5)	Ring breath
1284 (+13)	1272 (+9)	1274 (+9)	1267 (+11)	$\nu(C\text{-}O)_{hydroxyl}$ + ring breath
1430 (+3)	1413 (+9)	1417 (+2)	1411 (+13)	sym. $\nu(COO)_{carboxylate}$
1505 (-6)	1503 (-5)	1501 (-7)	1505 (-3)	asym. $\nu(COO)_{carboxylate}$
1576 (0)	1560 (0)	1561 (0)	1563 (-3)	$\nu(C\text{-}C)_{phenyl}$
1626 (+4)	1617 (+4)	1618 (+2)	1618 (+6)	$\nu(COO)_{carboxylate}$ + $\nu(C\text{-}C)_{phenyl}$

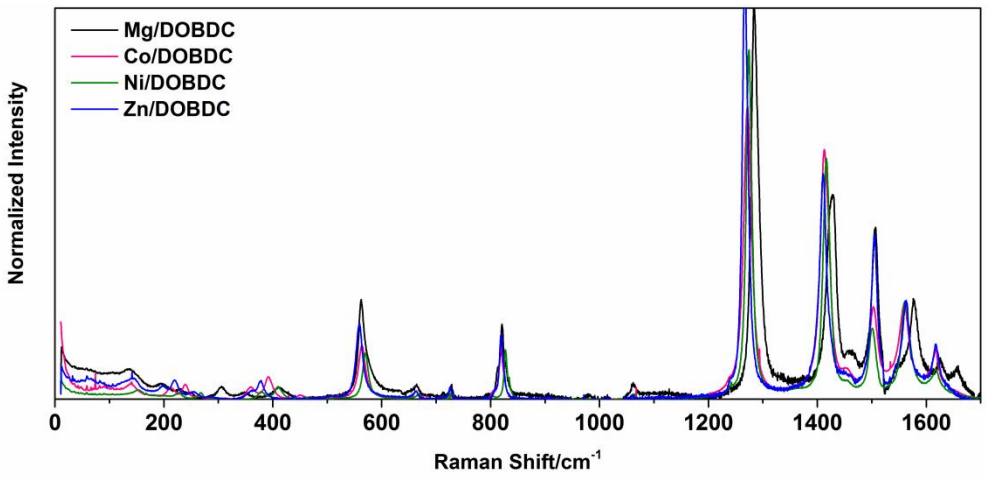

Figure 4.6 Full Raman spectra of as-synthesized Mg/DOBDC (black), Co/DOBDC (pink), Ni/DOBDC (green) and Zn/DOBDC (blue).

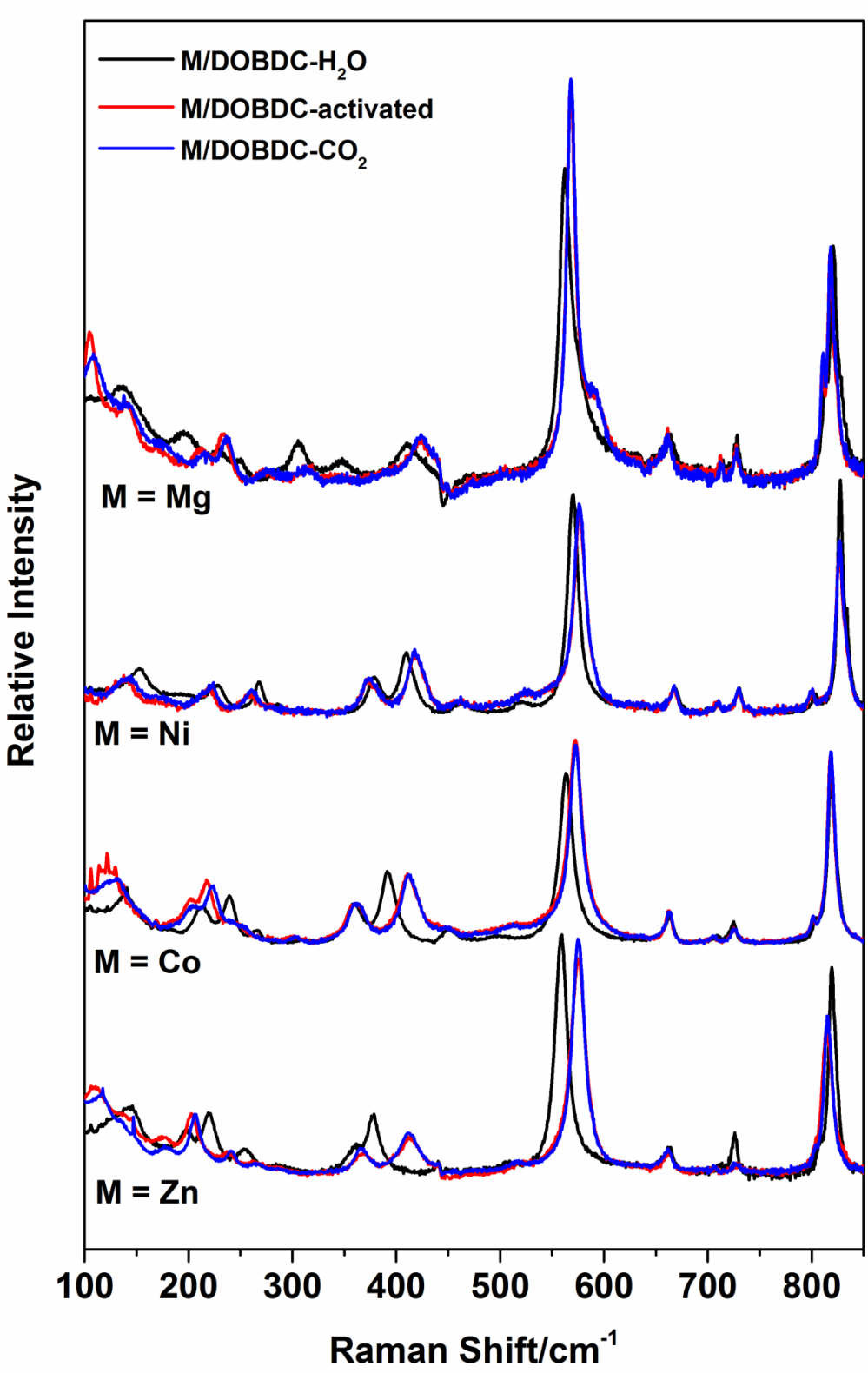

Figure 4.7 Expanded low frequency region of as-synthesized (black), activated (red) and CO_2 treated (blue) M/DOBDC.

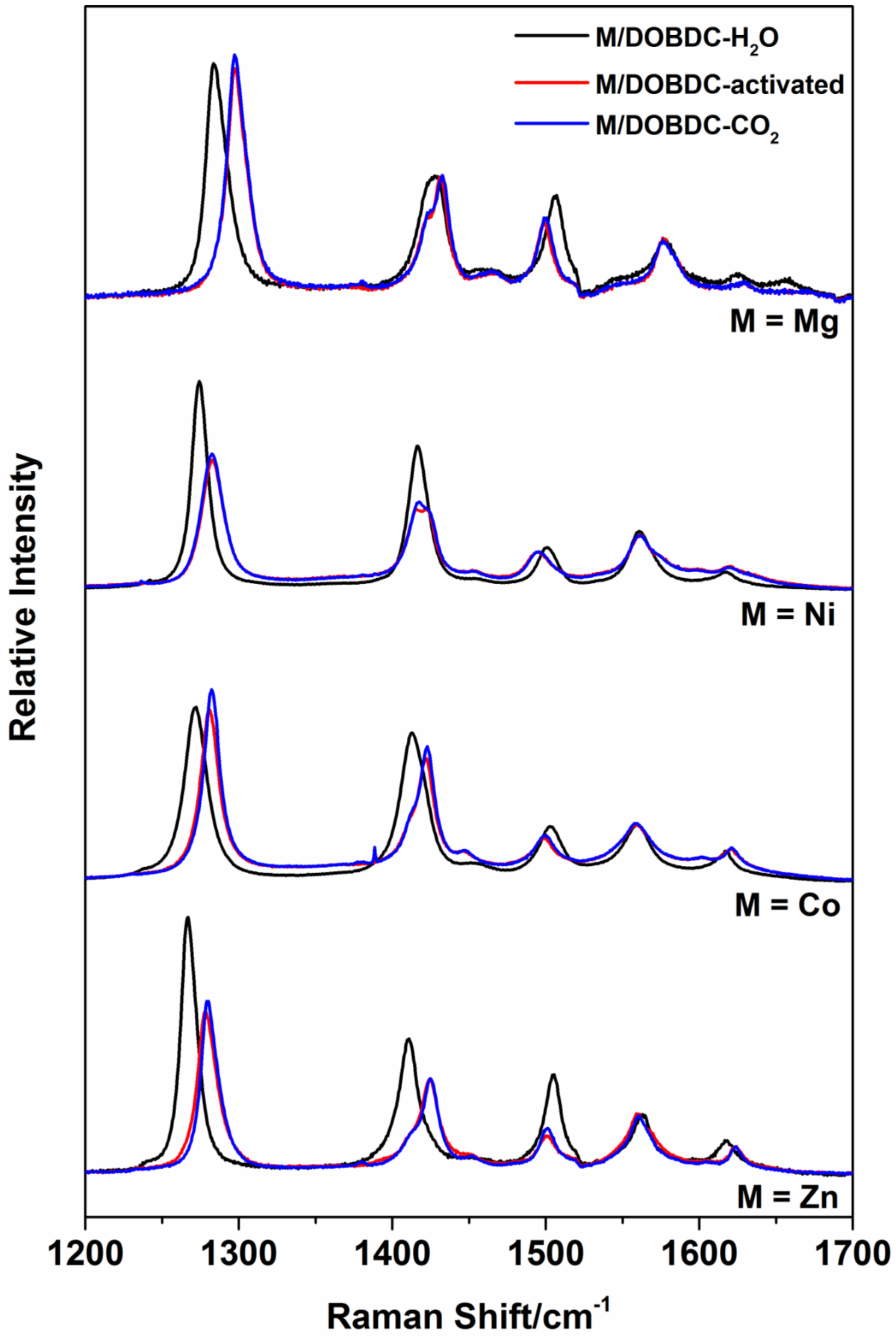

Figure 4.8 Expanded high frequency region of as-synthesized (black), activated (red) and CO_2 treated (blue) M/DOBDC.

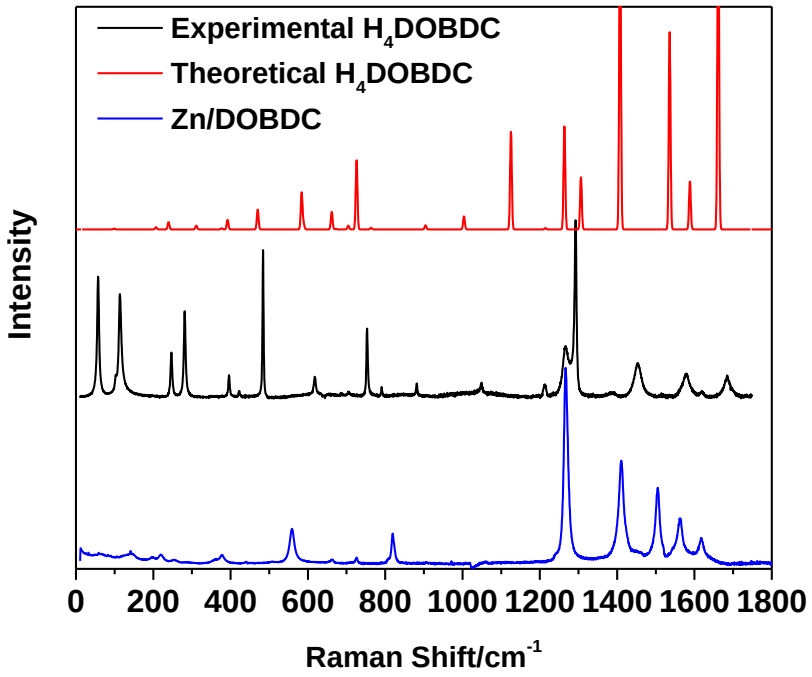

Figure 4.9 The Raman spectra of calculated H_4DOBDC ligand (red), experimental H4DOBDC (black) and Zn/DOBDC (blue).

Table 4.2 Experimental and calculated Raman active vibrational mode frequencies with descriptions of dominant components of the corresponding vibrational mode assignments for the H_4DOBDC ligand

Exp. Frequency of H_4DOBDC	Calc. Frequency	Raman assignment
396	392	Out of plane ring tilt
484	490	In plane ring tilt
752	756	Ring breathing
1267	1316	ν(C-O)$_{hydroxyl}$ + Ring breathing
1293	1360	β(C-H)
1453	1466	sym. ν(COOH) + β(C-H) + Ring breathing
1578	1600	asym. sym. ν(COOH) + β(C-H) + Ring breathing
1675	1731	ν(C=O) + sym ν(C-C)$_{phenyl}$

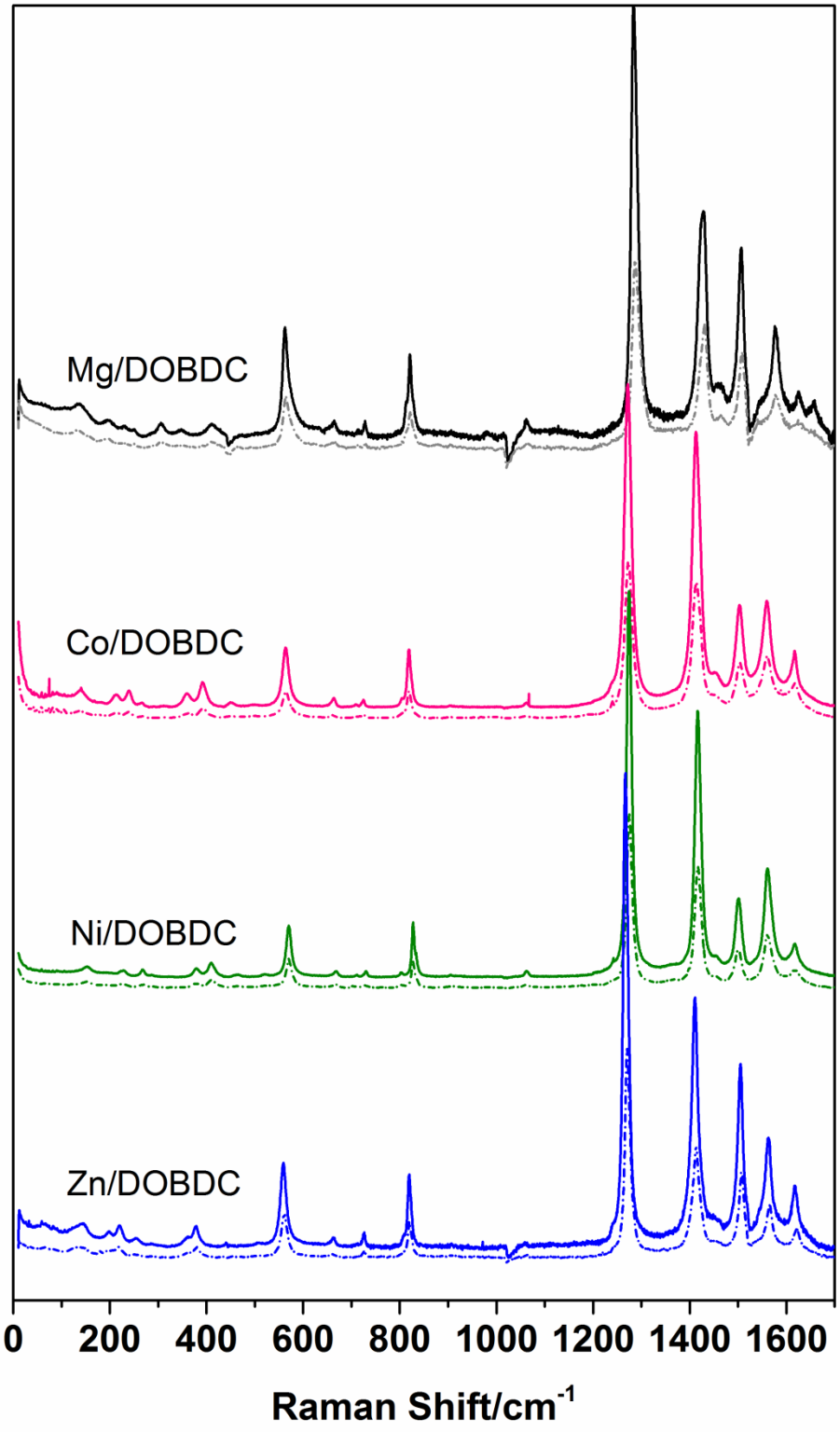

Figure 4.10 The Raman spectra of as-synthesized M/DOBDC frameworks and frameworks recovered after in-situ experiments.

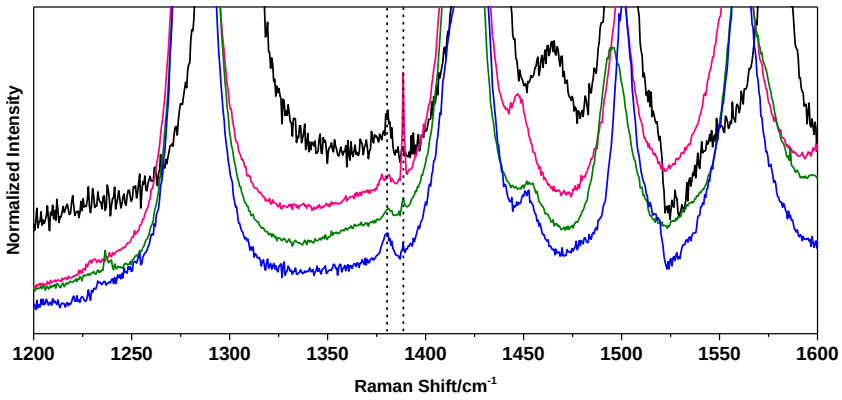

Figure 4.11 Expanded spectra of highlighted CO_2 features in Mg/DOBDC (black), Co/DOBDC (pink), Ni/DOBDC (green) and Zn/DOBDC (blue).

4.3 Discussion

As discussed above, CO_2 uptake measured for each framework increased in the order Zn<Co<Ni<Mg. A well established theory may be used to explain the difference. Based on empirical data and electron repulsion model, Holmes [41] showed that in high spin square pyramidal coordination compounds, the L_{basal}-M-L_{basal} angle (defined as θ) increases upon increasing number of d-electrons from d^7 to d^9 transition metals. In this C_{4v} symmetry, this increasingly fills the d_{xz}, d_{yz} and d_{z^2} orbitals, generating more repulsion between these orbitals and basal ligands which force the basal ligands move toward a larger θ. When the number of electrons increases to ten, however all the *d* orbitals are filled and a uniform d-electron distribution is formed, the symmetry of lowest energy goes to a small θ again. So that in terms of the L_{basal}-M-L_{basal} angle θ, a relation of Zn^{2+} (d^{10}) < Ni^{2+} (d^8) > Co^{2+} (d^7) can be built. This comparison brings a new factor that may be contributing to the difference of CO_2 uptake. One can imagine that at least for transition metal based versions of the framework, the open metal sites generated upon activation may be less accessible with smaller θ, fitting with the Zn/DOBDC < Ni/DOBDC > Co/DOBDC trend in observed CO_2 uptake performance. Mg/DOBDC is excluded from the comparison because its electron structure is quite different from the other three elements. An analysis of the reported crystal structures along with the diffuse reflectance and Raman data obtained upon activation follows and shows strong support for this structure changes hypothesis.

The single crystal XRD data [13] show that the metal site in M/DOBDC in the hydrated form is a tetragonally distorted octahedral symmetry with elongated axial ligands, in which the metal ion is equatorially coordinated to four oxygens atoms, and

axially coordinated to one linker hydroxyl oxygen and one oxygen from a pore wall-facing water molecule. The two axial M-O bonds are approximately 2.2 Å. The four equatorial M-O bonds are approximately 2.0 Å and slightly bent out-of-plane away from the coordinated water, leading to C_{4v} symmetry for these metal sites. Upon the removal of the water through thermal activation, the coordination geometry converts to a distorted 5 coordinate square pyramidal geometry, also with C_{4v} symmetry which makes Holmes' theory applicable. The degree to which this distortion occurs may ultimately impact the accessibility of the metal sites in the framework walls for further gas adsorption.

As shown in figure 4.5a-d, these coordination geometry changes have negligible effect on the diffuse reflectance (DR) spectra of Mg/DOBDC and Zn/DOBDC due to the absence of d-d transitions but alter the DR spectra of Co/DOBDC and Ni/DOBDC. While the general trends of these changes can be explained by ligand field theory, the interpretation presented here may not be comprehensive since these changes can also be affected by steric and electrostatic effects.

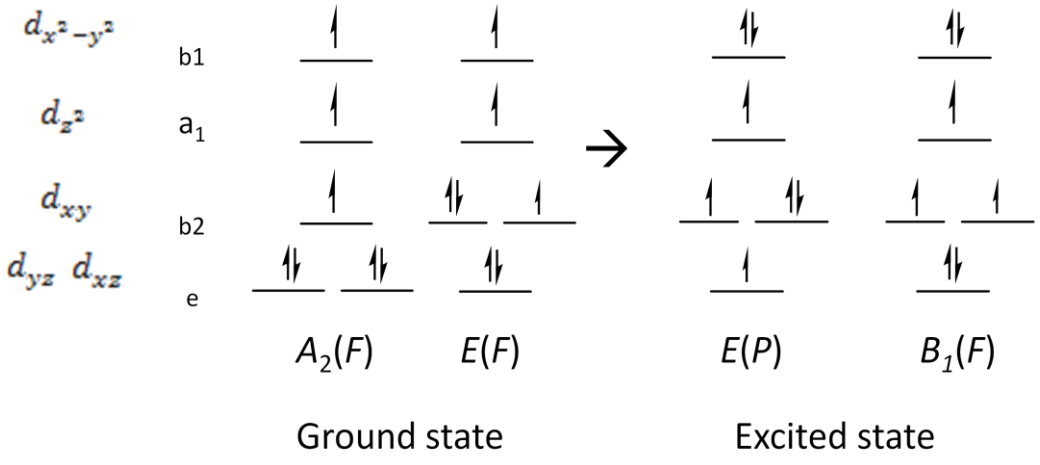

Figure 4.12 the ground and excited state d-electron configurations under these two geometries.

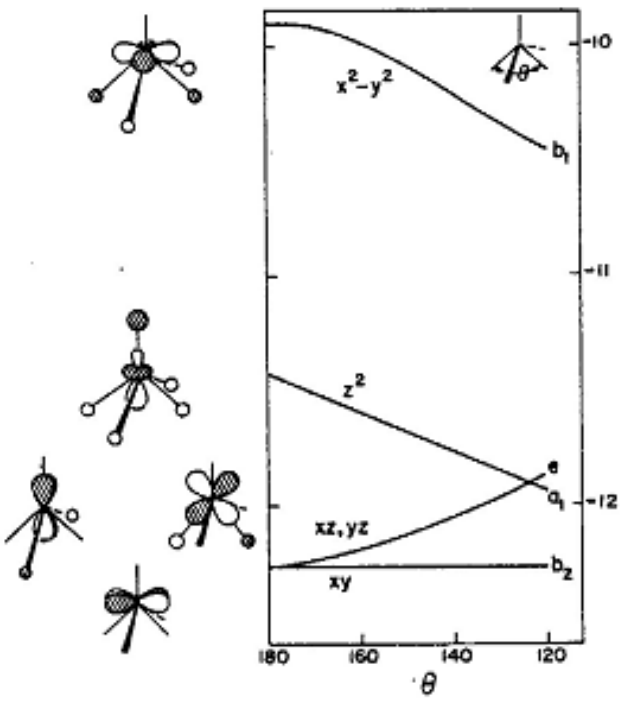

Figure 4.13 calculated orbital energy level of square pyramid pentacoordinated transition metal ion, as a function of the Lbasal-M-Lbasal angle θ. The vertical energy unit is in eV. Reprinted with permission from Inorg. Chem. 14:365-374 . Copyright 1975 American Chemistry Society.

In the DR-UV-vis spectra of Co/DOBDC, a considerable red shift of the $^4E(P)$ and $^4B_1$ transitions occurs upon framework activation, indicating a significant energy decrease between the ground state and the excited states in the newly created 5 coordinate geometry. This shift may be explained at least in part by considering the ground and excited state d-electron configurations under these two geometries illustrated in Figure 4.12 and a simple electron repulsion model. In this model, the removal of axial ligand reduces the repulsion between d_{z^2}, $d_{xz}$and d_{yz} orbitals because the interaction between the d electrons and σ orbitals of ligands is anti-bonding, after the coordinated water is removed, the basal oxygens should move toward the empty position due to the repulsion between ligands. As shown in Figure 4.13, the relative energies of d orbitals in a

pentacoordinated square pyramid complex are predicted to be strongly associated with the L_{basal}-M-L_{basal} angle, defined as θ. [26, 27, 39, 40] As this bond angle θ bends away from 180º, the d_{xz} and d_{yz} orbitals begin to mix with the basal ligand σ orbitals, so the anti-bonding interaction increases the energy of the two orbitals. At the same time, the overlap between the basal ligand orbitals and d_{z^2}, $d_{x^2-y^2}$ orbitals is reduced which leads to a decrease of d_{z^2} and $d_{x^2-y^2}$ energy level. Thus, the red shift of Co/DOBDC absorbance bands may indicate a notable change of θ. from a starting value of ~189º in the hydrated framework to a value less than 180º In this case, the four equatorial oxygens flipped away from the axial ligand and move towards the empty axial position. This assumption is also supported by the increased intensity of transition to $^4B_1(F)$ state. This transition usually is very weak in pseudo octadehral symmetry because its orbitally forbidden from a $^4A_2(F)$ ground state. But in a square pyramidal symmetry with relatively small θ, the energy level of $^4E(F)$ ground state become more degenerate with $^4A_2(F)$ so that the transition can be observed.

While the analysis of Ni/DOBDC DR spectra may be more complicated, due to the significant overlap of the $^3E(P)$ band with that of the ligand, it is apparent that the blue shift of the band is opposite to what is found in the Co/DOBDC case. The reversed shift direction compared to Co/DOBDC suggests a different change in θ when the coordination environment changes. In Ni/DOBDC, the basal ligands should move towards the empty axial position like Co/DOBDC but the final form may be a planar geometry with θ closer to 180º. The reduced overlap with d_{xz}, d_{yz} orbitals stabilized these orbitals and cause a larger energy gap between the ground state and $^3E(P)$, $^3B_1(F)$ states. These observations are consistent with the Holms' work. [41]

Raman data collected under the same condition adds more information to the local structural changes. First, Raman spectra from *in-situ* experiments provide evidence that the coordinated water molecules are indeed removed upon activation and the yielded open metal sites are then occupied by CO_2 molecules. The significant red shift of O-M-O bending vibrational mode in the region of 150 cm^{-1} ~ 300 cm^{-1} indicates a reduced repulsion from the axial position. These peaks then show a slight blue shift after CO_2 treatment, which implies the existence of weakly interacted CO_2 molecules. Furthermore, a weak feature at 1381 cm^{-1} that appears upon CO_2 treatment is a peak red shifted from a signature peak of CO_2 at 1388 cm^{-1} (Figure 4.11). [37, 38] This peak is a sign of 'end-on' interaction between CO_2 molecule and open metal site because the electron density change breaks the original $D_{\infty h}$ symmetry to a $C_{\infty h}$. The characteristic 1388 cm^{-1} peak of free CO_2 is also observed in the spectra and very likely come from the non-interacting or very weakly interacting CO_2 molecules. The reason that the intensity of this free CO_2 peak varies in the spectra from one M/DOBDC CO_2 treated sample to the other is not entirely clear.

Another significant change of Raman spectra is related to the bond distance between the metal ion and surrounding ligands. From table 4.1, an interesting trend of the M-O stretch, COO bending mode and symmetric COO stretch modes can be observed upon activation. All three vibrational modes mentioned above undergo blue shift of frequencies upon activation. This change can be rationalized by a more compact coordination sphere with shorter M-O and C-O bonds. It's worth to remark that the blue shift of M-O stretch vibrational mode (~400 cm^{-1}) of Ni/DOBDC is less than half that of Co/DOBDC and only one fourth of Zn/DOBDC. The same trend remains for the other

two modes, in which Mg/DOBDC and Ni/DOBDC only have minor increase of frequencies, but Co/DOBDC and Zn/DOBDC shifted much more. Approximately, the frequencies shift is in the order of Mg/DOBDC ≈ Ni/DOBDC < Co/DOBDC < Zn/DOBDC. This difference strongly implies that Zn/DOBDC experienced the most dramatic local structure alternation to form a compact coordination sphere, while Mg/DOBDC and Ni/DOBDC has relatively small changes of bond length. In this case, the open metal sites are harder to access by CO_2 molecules due to steric effect. Hence, the trend fits the expectation from the CO_2 adsorption experiments.

Beside the local coordination environment, Raman data also provides a hint about an additional structural change of Zn/DOBDC compared to the other frameworks. After the activation process, the ring breathing mode and the C=C stretching mode from the ligand stay at the same frequencies in all samples except for Zn/DOBDC, which shows a slightly shift to lower frequencies after water removal. These frequency changes suggest that a rearrangement of the ligand position or orientation occurs upon activation. But the relationship between this phenomenon and the property of framework is not clear.

4.4 Current Conclusions and Future Work

In this chapter, four isostructure M/DOBDC (M = Mg, Co, Ni, Zn) MOFs were investigated by in-situ DR-UV-vis and Raman spectroscopy methods. The comparison of the resulting spectra reveals unique structural change in each framework. DR-UV-vis shows that a possible variation of ligand-metal-ligand bond angles among the activated frameworks. Raman spectra revealed the difference of metal-ligand bond length changes upon activation. Both factors have the potential to affect CO_2 adsorption property and agree with the experimental data of CO_2 uptake. This study shows that CO_2 capacity of M/DOBDC may be affected by a combination of various factors, and that the local coordination structure at the metal site upon activation likely plays an important role.

Correct interpretation of the complicated spectroscopy data is not trivial and frequently over simplified model is used. The results are not only obtained from the combination of various spectroscopy techniques, but also from previously obtained single crystal structure and CO_2 adsorption data. Some previously mentioned ambiguities, such as the uncertain assignment of low frequency modes in the Raman spectra, as well as the local structure information of Mg/DOBDC and Zn/DOBDC are still waiting for more work to support. These missing pieces can be filled by phonon calculation of the extended frameworks and XAS experimental, which will be the center of the future work.

4.5 Material and Methods

4.5.1 Synthesis of M/DOBDC MOF materials

M/DOBDC MOFs were synthesized following the previously published procedure, [11, 13] **Mg/DOBDC**: A solution of 2,5-dihydroxybenzene-1,4-dicarboxylic acid (0.074 g, 0.375 mmol) in THF (5 ml) and a solution of magnesium(II) acetate (0.19 g, 0.75 mmol) in water (3 ml) were mixed in a glass reaction tube of 50 ml. 1.5 ml NaOH (1 mol/L) was added into the mixture while stirring. The tube was sealed by a Teflon cap and heated in a pre-heated oven at 110ºC for 3 days. The light yellow powder was collected by filtration and washed by THF and water. **Co/DOBDC**: A solution of 2,5-dihydroxybenzene-1,4-dicarboxylic acid (0.74 g, 3.75 mmol) in THF (50 ml) and a solution of cobalt(II) acetate (1.87 g, 7.5 mmol) in water (25 ml) were mixed in a glass reaction tube of 150 ml. The tube was sealed by a Teflon cap and heated in a pre-heated oven at 110ºC for 3 days. The deep red micro-crystals was collected by filtration and washed by THF and water. **Ni/DOBDC**: A solution of 2,5-dihydroxybenzene-1,4-dicarboxylic acid (0.6 g, 3 mmol) in THF (10 ml) and a solution of cobalt(II) acetate (1.5 g, 6 mmol) in water (10 ml) were mixed in a glass reaction tube of 40 ml. The tube was sealed by a Teflon cap and heated in a pre-heated oven at 110ºC for 3 days. The yellow powder was collected by filtration and washed by THF and water. **Zn/DOBDC**: A solution of 2,5-dihydroxybenzene-1,4-dicarboxylic acid (0.074 g, 0.375 mmol) in THF (5 ml) and a solution of zinc(II) acetate (0.23 g, 0.75 mmol) in water (3 ml) were mixed in a glass reaction tube of 50 ml. 1.5 ml NaOH (1 mol/L) was added into the mixture while stirring. The tube was sealed by a Teflon cap and heated in a pre-heated oven at 110ºC

for 3 days. The light yellow powder was collected by filtration and washed by THF and water.

4.5.2 X-ray diffraction

The powder samples of M/DOBDC (M = Mg, Co, Ni, Zn) before and after activation were measured on a Bruker SMART APEX CCD diffractometer by using Cu Kα radiation over the range of 3-50º at room temperature.

4.5.3 Diffuse reflectance spectroscopy

Diffuse reflectance spectra of M/DOBDC (M = Mg, Co, Ni, Zn) samples were collected using a Cary-Varian UV-visible-NIR spectrophotometer equipped with a diffuse reflectance accessory and controlled environment (vacuum/gas and temperature) solid state sample holder (Harrick Instruments). Adsorption spectra of the samples were collected at 10 ºC intervals from 30 ºC to 150 ºC under dynamic vacuum**.** The adsorption spectra were collected again after cooling to room temperature and followed by purging with CO_2 gas until no further spectral changes were observed.

4.5.4 Raman spectroscopy

Raman spectra were collected using a 532 nm single frequency diode laser with ~ 8 mW power, a triple monochromator and a 1340 × 100 pixel liquid nitrogen-cooled CCD detector (Princeton Instruments). With 50 μm entrance slit width, the spectral resolution was < 3 cm^{-1} and peak frequency shifts of <1 cm^{-1} could be measured. The sample was deposited on a stainless steel frit and attached on a spinning sample holder in a home-made reaction chamber with optic windows and a remote IR temperature detector.

The sample was spun during the data collection process to minimize the residence time of the laser on one spot of the sample thereby avoiding excessive heating that could locally activate the framework. The Raman data of as-synthesized M/DOBDC, activated M/DOBDC and CO_2 treated M/DOBDC was measured *in-situ* in the reaction chamber. After the collection of as-synthesized sample, the samples were heated to 150 ºC under vacuum and the temperature was hold for 1 hr to ensure complete activation. Then the chamber was purged with dry N_2 and cooled to room temperature when the Raman spectra of activated samples were collected. At last, dry CO_2 was purged through the chamber for 20 min to replace N_2 and Raman spectra were collected again.

4.5.5 DFT calculation

The geometry optimization and vibrational modes of H_4DOBDC was calculated using the Gaussian 03 program package [42] at the density functional theory (DFT) level with Becke's three parameter functional and Lee-Yang-Parr functional (B3LYP) method. 6-31G basis set was used. A summary of the calculated frequencies for the most Raman active vibrational modes is provided in Table 4.2.

4.6 Reference

1 J.-R. Li, R. J. Kuppler, H.-C. Zhou, *Chem. Soc. Rev.*, 2009, **38**, 1477–1504

2 K. Sumida, D. L. Rogow, J. A. Mason, T. M. McDonald, E. D. Bloch, Z. R. Herm, T.-H. Bae, J. R. Long, *Chem. Rev.*, 2012, **112**, 724–781

3 H. Furukawa, K. E. Cordova, M. O'Keeffe, O. M. Yaghi, *Science*, **341**, 974

4 D. M. D'Alessandro, B. Smit, J. R.Long, *Angew. Chem. Int. Ed.*, 2010, **49**, 6058–6082

5 P. D. C. Dietzel, B. Panella, M. Hirscher, R. Blom, H. Fjellvåg, *Chem. Commun.*, 2006, 959–961

6 P. D. C. Dietzel, Y. Morita, R. Blom, H. Fjellvåg, *Angew. Chem.*, 2005, **117**, 6512–6516; Angew. Chem. Int. Ed.2005, 44, 6354–6358

7 N. L. Rosi, J. Kim, M. Eddaoudi, B. Chen, M. O. Keefe, O. M. Yaghi, *J. Am. Chem. Soc.*, 2005, **127**, 1504–1518

8 D. Britt, H. Furukawa, B. Wang, T. Grant Glover, O. M. Yaghi, *PNAS*, **106**, 20637-20640

9 S. R. Caskey, A. G. Wong-Foy, A. J. Matzger, *J. Am. Chem. Soc.*, 2008, **130**, 10870–10871

10 A. Ö. Yazaydin, R. Q. Snurr, T.-h. Park, K. Koh, J. Liu, M. D. LeVan, A. I. Benin, P. Jakubczak, M. Lanuza, D. B. Galloway, J. J. Low, R. R. Willis, *J. Am. Chem. Soc.*, 2009, **131**, 18198–18199

11 P. D. C. Dietzel, R. D. Johnsen, R. Blom, H. Fjellvåg, *Chem. Eur. J.*, 2008, **14**, 2389 – 2397

12 P. D. C. Dietzel, Y. Morita, R. Blom, H. Fjellvåg, *Angew. Chem. Int. Ed.*, 2005, **44**, 6354–6358

13 P. D. C. Dietzel, R. E. Johnsen, H. Fjellvåg, S. Bordiga, E. Groppo, S. Chavan, R. Blom, *Chem. Commun.*,2008, 5125–5127

14 N. Nijem, P. Canepa, L. Kong, H. Wu, J. Li, T. Thonhauser, Y. J. Chabal, *J. Phys.: Condens. Matter.*, 2012, **24**, 424203

15 L. Valenzano, B. Civalleri, S. Chavan, G. T. Palomino, C. O. Areán, S. Bordiga, *J. Phys. Chem. C*, 2010, **114**, 11185–11191

16 W. L. Queen, C. M. Brown, D. K. Britt, P. Zajdel, M. R. Hudson, O. M. Yaghi, *J. Phys. Chem. C*, 2011, **115**, 24915–24919

17 S. Chavan, J. G. Vitillo, E. Groppo, F. Bonino, C. Lamberti, P. D. C. Dietzel, S. Bordiga, *J. Phys. Chem. C*, 2009, **113**, 3292–3299

18 S. Chavan, F. Bonino, J. G. Vitillo, E. Groppo, C. Lamberti, P. D. C. Dietzel, A. Zecchina, S. Bordiga, *Phys.Chem.Chem.Phys.*, 2009, **11**, 9811–9822

19 F. Bonino, S. Chavan, J. G. Vitillo, E. Groppo, G. Agostini, C. Lamberti, P. D. C. Dietzel, C. Prestipino, S. Bordiga, *Chem. Mater.*, 2008, **20**, 4957–4968

20 W. S. Drisdell, R. Poloni, T. M. McDonald, J. R. Long, B. Smit, J. B. Neaton, D. Prendergast, J. B. Kortright, *J. Am. Chem. Soc.*, 2013, **135**, 18183−18190

21 J. Yu, P. B. Balbuena, *J. Phys. Chem. C*, 2013, **117**, 3383−3388

22 L. Valenzano, B. Civalleri, K. Sillar, J. Sauer, *J. Phys. Chem. C*, 2011, **115**, 21777–21784

23 A. L. Dzubak, L.-C. Lin, J. Kim, J. A. Swisher, R. Poloni, S. N. Maximoff, B. Smit, L. Gagliardi, *Nat. Chem.*, 2012, **4**, 810-816

24 D. C. Harris, M. D. Bertolucci, *Symmetry and Spectroscopy: An Introduction to Vibrational and Electronic Spectroscopy*, Dover Publication, Inc, 2013

25 Lever, A. B. P., *Inorganic Electronic Spectroscopy* 2nd ed.; Elsevier Science Publishers: New York, 1984

26 M. Gerloch, J. Kohl, J. Lewis, W. Urland, Inorg. Phys. Theor., 1970, 3283-3296

27 M. Gerloch, J. Kohl, J. Lewis, W. Urland, Inorg. Phys. Theor., 1970, 3269-3283

28 B. Pullman, N. Goldblum, *Metal-Ligand Interactions in Organic Chemistry and Biochemistry*, D. Reidel Publishing Company, 1976

29 K. Helios, M. Duczmal, A. Pietraszko, D. Michalska, *Polyhedron*, 2013, **49**, 259-268

30 K. Malek, H. Kozłowski, L. M. Proniewicz, *Polyhedron*, 2005, **24**, 1175-1184

31 R. Wysokiński, B. Morzyk-Ociepa, T. Głowiak, D. Michalska, *J. Mol. Struct.*, 2002, **606**, 241-251

32 T. Ishioka, Y. Shibata, M. Takahashi, I. Kanesaka, *Spectrochim. Acta, Part A*, 1998, **54**, 1811-1818

33 T. Ishioka, Y. Shibata, M. Takahashi, I. Kanesaka, Y. Kitagawa, K. T. Nakamura, *Spectrochim. Acta, Part A*, 1998, **54**, 1827-1836

34 K. Nakamoto, *Infrared and Raman Spectra of Inorganic and Coordination Compounds*, John Wiley & Sons, Inc, 4th Edition, 1986

35 J. R. Ferraro, *Low-Frequency Vibrations of Inorganic and Coordination Compounds*, Plenum Press, 1971

36 G. Socrates, *Infrared and Raman Characteristic Group Frequencies: Tables and Charts*, John Wiley & Sons, Inc, 3th Edition, 2004

37 H. Forster and M. Schumann, *Journal of the Chemical Society, Faraday Transactions 1: Physical Chemistry in Condensed Phases*, 1989, **85**, 1149-1158

38 F. X. Llabrés i Xamena, A. Zecchina, *Phys. Chem. Chem. Phys.*, 2002, **4**, 1978–1982

39 A. R. Rossi, R. Hoffmann, *Inorg. Chem.*, 1975, **14**, 365-374

40 T. A. Albright, J. K. Burdett, M.-H. Whangbo, *Orbital Interactions in Chemistry*, John Wiley & Sons, Inc, 2th Edition, 2013

41 R. R. Holmes, *J. Am. Chem. Soc.*, 1984, **106**, 3745-3750

42 M. J. Frisch, G. W. Trucks, H. B. Schlegel, G. E. Scuseria, M. A. Robb, J. R. Cheeseman, G. Scalmani, V. Barone, B. Mennucci, G. A. Petersson, H. Nakatsuji, M. Caricato, X. Li, H. P. Hratchian, A. F. Izmaylov, J. Bloino, G. Zheng, J. L. Sonnenberg, M. Hada, M. Ehara, K. Toyota, R. Fukuda, J. Hasegawa, M. Ishida, T. Nakajima, Y. Honda, O. Kitao, H. Nakai, T. Vreven, J. A. Montgomery, Jr., J. E. Peralta, F. Ogliaro, M. Bearpark, J. J. Heyd, E. Brothers, K. N. Kudin, V. N. Staroverov, R. Kobayashi, J. Normand, K. Raghavachari, A. Rendell, J. C. Burant, S. S. Iyengar, J. Tomasi, M. Cossi, N. Rega, J. M. Millam, M. Klene, J. E. Knox, J. B. Cross, V. Bakken, C. Adamo, J. Jaramillo, R. Gomperts, R. E. Stratmann, O. Yazyev, A. J. Austin, R. Cammi, C. Pomelli, J. W. Ochterski, R. L. Martin, K. Morokuma, V. G. Zakrzewski, G. A. Voth, P. Salvador, J. J. Dannenberg, S. Dapprich, A. D. Daniels, Ö. Farkas, J. B. Foresman, J. V. Ortiz, J. Cioslowski, and D. J. Fox; Gaussian Inc.: Wallingford, CT, 2010

Chapter 5. A Raman spectroscopy study of cucurbit[7]uril-ferrocene host-guest complex in the solid state

5.1 Introduction

Owing to their selective complexation behavior, cucurbit[n]urils (CB[n]s), have emerged as promising water soluble macrocyclic hosts for a number of applications, including stereoselective chemical reaction mediation, drug delivery and dye-binding for displays, sensors and solar cells.[1-3] The unique architecture and the negative electrostatic potential surface of the interior create an ideal host environment for the encapsulation of either positively charged or neutral guest molecules. Multiple intermolecular forces are responsible for the CB[n] complexation process, including ion-dipole and hydrophobic interactions between the molecular guest and the host cavity interior.[2-4] Additionally, the carbonyl groups on the perimeter of the CB[n] opening can strongly interact with metal ions.[5-8] This complexation mechanism contrasts with that found in other cavitands such as cyclodextrins, in which the hydrophobic interactions alone are believed to dominate the complexation process.[9] Consequently, the multiple binding forces involved in CB[n] encapsulation give rise to highly stable inclusion complexes in solution, with binding equilibrium constants as high as 10^{15} M^{-1},[10] as well as in the solid state. In fact several crystal structures of CB complexes with encapsulated guest molecules have been reported.[11-13]

Given the growing interest in using these supramolecular hosts in solid state materials, in particular interfaced with semiconductor surfaces,[2, 14-16] it is essential to understand the structural ramifications for guest@CB[n] complexes in the solid state.

One important question is whether these host-guest complexes are stable not only in single crystalline form but in other solid state environments as well. While there are standard ways of probing the CB encapsulation process in solution (^{1}H NMR, for one), studying CB complexes in solid phase environments presents a greater challenge since characterization methods are more limited. Vibrational spectroscopy is a useful method for analyzing molecular structure and structural changes of inclusion complexes by monitoring the frequency shifts of specific vibrational modes attributed to either the host or the guest. FTIR is a readily available technique that has been applied to several CB[n] complexes in solid state environments. [17-19] As illustrated by these examples, the utility of this technique for gaining in depth structural information is severely limited when the measurable IR bands originating from the CB host overlap with those of the encapsulated guest. Raman spectroscopy is ideally suited for studying materials in solid state has been used to interrogate the structures of other host-guest systems such as molecular species inside zeolite frameworks [20-22] carbon nanotubes,[23, 24] clathrates[25, 26] and other supramolecular cavitand complexes,[27-31] it has not been widely utilized to study CB[n] complexes. The Raman spectra of the CB[n] (n=5-8) host macrocycles were only recently published along with their vibrational mode assignments.[32] Since then, several surface enhanced Raman scattering (SERS) investigations of CB complexes adsorbed onto metal nanoparticles in solution have been reported.[33-35] The plasmonic effects at the interfaces or nanojunctions in these systems afford incredibly large Raman enhancement factor (10^{10} to 10^{11}), allowing measurements of very low CB complex concentrations. Traditional Raman spectroscopy techniques are needed to elucidate the structural

ramifications of cucurbituril complex formation on non-metallic surfaces and other solid state environments where CB[n] concentrations are much higher.

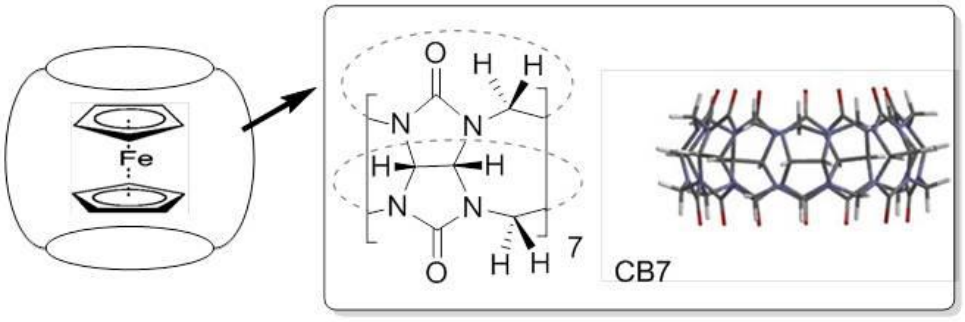

Figure 5.1 Depiction of CB7 and Fc@CB7

In this chapter we present that the Raman spectroscopy can be a useful tool to investigate supramolecular complex in the solid state, specifically a complex formed between CB7 and ferrocene, Fc@CB7 (Figure 5.1). Ferrocene and CB7 can form stable complex with an equilibrium constant of 4×10^4 L/mol in aqueous solution. [49] This investigation demonstrates how Raman spectroscopy can be used to 1.) confirm the residence of the guest molecule inside the CB7 cavity in the solid state and 2.) interrogate the structural changes that both the host and guest experience upon encapsulation. Ferrocene was chosen for this initial study because its Raman spectrum is well known and fully assigned [36, 37] and its complexation behavior with CB7 has been well documented. [13, 38-40]

5.2 Result and Discussion

These Raman data comparisons (Figure 5.2) demonstrate the vibrational frequency shifts (or lack thereof) for the different vibrational modes upon complexation. The two low frequency bands of Fc, the symmetric Fe-Cp ring stretch at 307 and ring tilt at 391 cm^{-1}, increase in frequency to 318 and 400 cm^{-1} respectively, indicating higher force constants for these modes upon complexation with CB7. This trend is in line with the anticipated restricted motion along these vibrational coordinates for a constrained Fc molecule residing within the CB cavity. Similar changes in force constant have been reported for Fc derivatives with bridge Cp ligands that also restrict motion along these Fc-Cp stretch and tilt coordinates.[42] Additionally, this interpretation of the Raman data is consistent with the crystal structure of Fc@CB7. [13] The slightly shorter Fe-C distances reported for the complex compared to the known values for unbound Fc with the same conformation indicate higher bond orders and therefore higher force constants for the Fe-Cp stretch and tilt modes.

The vibrational modes localized on the CB7 macrocycle also exhibit subtle changes when Fc is incorporated in the complex. Most notably, the two CB ring distortion modes at 442 and 833 cm^{-1}, which both involve deformations of the cavity interior, appear at lower frequencies when Fc is included. The reduced force constants for these modes may reflect an overall expansion of the macrocycle upon Fc encapsulation due to weak interactions between the peripheral hydrogens of the Cp rings and the C and N atoms of the CB7 cavity interior. [13] At the same time, modes such as the one assigned to a CB HC-CH twist at 654 cm^{-1} with only peripheral atomic displacements, show no

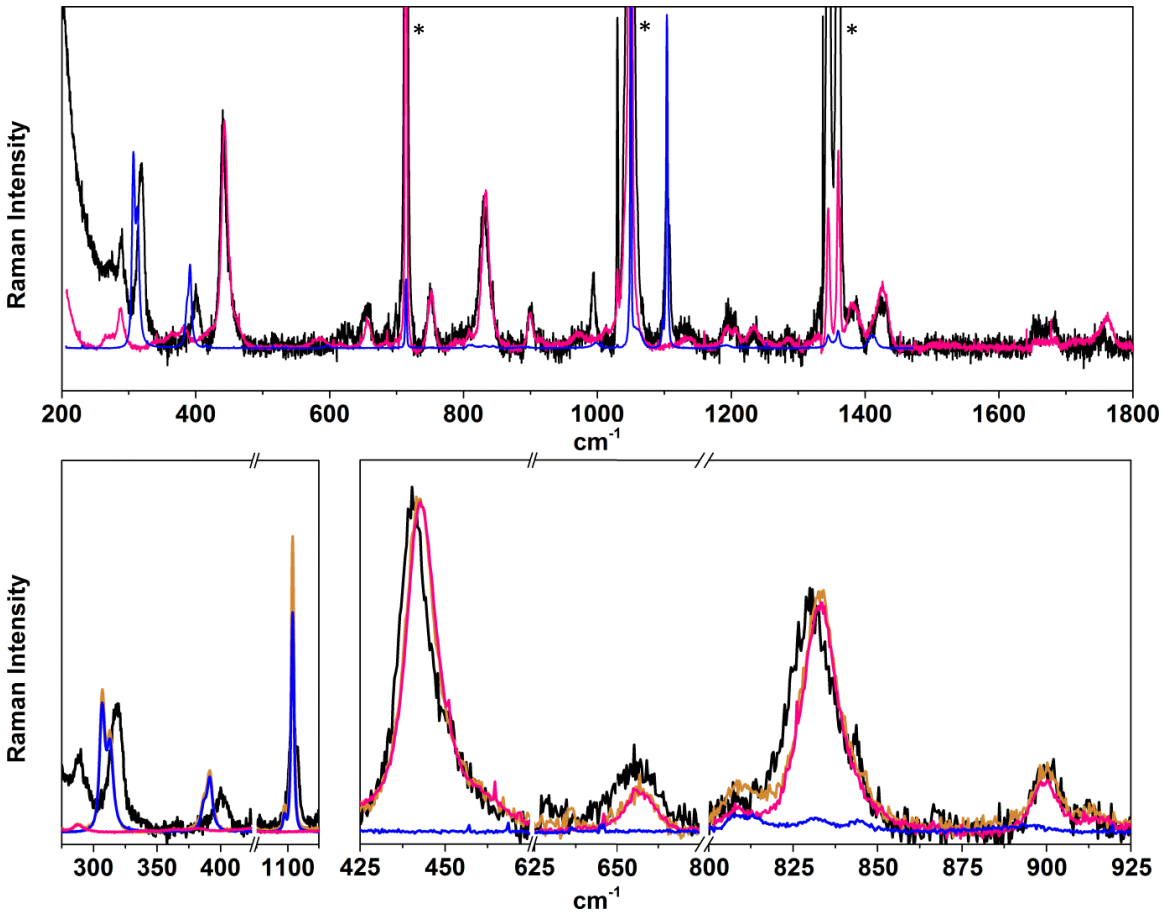

Figure 5.2 (a) Raman spectra of Ferrocene (Blue), CB7(red), the physical mixture(Orange) and Fc@CB7 (Black). Selected Raman spectral regions highlighting (b) Fc and (c) CB7 vibrational modes. (note: KNO_3 internal standard peaks indicated with *)

change in frequency when Fc is present. One likely explanation for this observation is that guest molecule encapsulation may have little or no effect on the force constants of modes dominated by atomic displacements of the macrocycle exterior. In other words with the ferrocene located inside the CB7 cavity, the outside of the macrocycle host would probably not contribute much to the weak intermolecular forces responsible for guest binding and therefore vibrational modes localized on this part of the ring would not be sensitive to the guest presence. Accordingly, a similar trend is observed for the ring deformation mode at 899 cm^{-1} and both the symmetric and asymmetric CB7 C-N

stretching modes (1382 and 1425 cm^{-1}, respectively), none of which involve significant distortions of the ring interior. However, the spectral overlap of the Fc and nitrate bands in the higher frequency range makes the assessment difficult for the latter two modes.

Table 5.1 Observed Raman frequencies for Fc, CB7 and Fc@CB7 and corresponding vibrational mode assignments.[a,b]

Fc	Fc@CB7	vibrational assignment	mode no.[a]
307 cm^{-1}	318 cm^{-1}	νFe-Cp	4
391	400	Cp ring tilt	16
998	994	βC-H (‖)	13
1059	-	βC-H (‖)[c]	24
1104	1104	Cp ring breathing	3
1411	-	νC-C[c]	15
CB7	Fc@CB7	vibrational assignment	
443	440	σN-C-N	
654	655	τHC-CH	
834	829	δC-N-C + ρCH_2	
899	900	βC-N-C +τN-C-C-N + νC-C	
1382	-	Sym. νC-N[c]	
1425	1426	Asym. νC-N	
1760	~1755[d]	νC=O	

ν = stretch, β = bend, δ = deformation, ρ = rock, σ = scissor, τ = twist.

‖ is with respect to the Cp ring plane. [a]vibrational mode assignments and mode numbers for Fc obtained from reference [30] [b]vibrational mode assignments for CB7 obtained from reference [27] [c]overlap with other Raman peaks prevents accurate frequency determination. [d]very weak

The steric interactions imposed by host-guest complexation may restrain certain vibrational motion, providing an intuitive explanation for some of the observed vibrational frequency changes described above. However, this is undoubtedly only part of the picture. There are electrostatic interactions that may also shift the vibrational mode frequencies, but not necessarily in the same direction as the steric effect. For example one

might reasonably expect that encapsulation would mechanically constrain the Cp ring breathing mode, thereby increasing its force constant. However, strong electrostatic field generated by neighboring functional groups, such as carbonyl group in CB7, may decrease the breathing mode of Cp ring. Down shift of Cp ring breathing mode has been reported in other type of host materials, such as zeolites. [20, 43] These opposing influences between steric effect and electrostatic field within the Fc@CB7 complex would, at least in part, negate each other's effect on this intraligand mode. While we should not exclude the possibility that the Cp ring breathing mode simply is not affected by encapsulation and therefore does not shift in frequency, a negating effect could be another reason that the intense Cp ring breathing mode at 1104 cm^{-1} shows no frequency change in the Raman spectrum of the Fc@CB7 complex.

The C-H bending modes of the Cp ring may also be sensitive to electrostatic effects, which can be used to explainthe observed downshift (i.e. lower force constant) of the Cp C-H bending mode from 998 to 994 cm^{-1}. This C-H bending vibration also exhibits a significant rise in relative intensity, which implies an increase in polarizability of this mode upon CB7 interaction with the Fc guest in the complex.

In addition to the multifaceted nature of the host-guest interaction, there are other factors that need be recognized when interpreting the Raman data for this complex. For one, the crystal structure reveals that the Fc enjoys some degree of rotational freedom within the CB7 cavity, leading to different orientations within the solid state complex. [13] This structural inhomogeneity is most likely responsible for the slight Fc peak broadening observed in the Fc@CB7 Raman spectrum, which reflects an average of the guest orientations in the CB7 cavity. The other important factor that should not be neglected is

the effect of counterions that coordinate with the complex. It is well known that cations in solution influence CB[n] complexation behavior due to their interaction with the electronegative part of the ring. [7, 8] Upon solvent removal, the location of the remaining cations relative to the CB cavity, with or without Fc guest molecules present, is not entirely clear and therefore neither is their contribution to the observed Raman spectrum. Most likely though, these countercations reside in the vicinity of the electronegative carbonyl groups lining the CB ring and would therefore influence the carbonyl stretching mode observed around 1760 cm^{-1}. While this mode appears to downshift upon CB7 complexation, the inability to discern the influence of the guest from that of the cations outside the cavity prevents us from drawing any conclusion regarding the role of the carbonyls in the host-guest interaction based on these data alone. These structural ambiguities and complicated host-guest interactions of Fc@CB7 highlight the need for additional experimental or theoretical evidence to fully explain the observed Raman spectrum changes for this complex in the solid.

5.3 Conclusion

In summary, despite some ambiguities, the observed behavior of specific vibrational modes localized on different parts of the complex provide strong evidence that Fc resides within the CB7 cavity and points to some of the more subtle structural and electronic interactions between the host and guest components. This chapter represents the fundamental Raman spectroscopy study of a cucurbituril host-guest complex in the solid state, laying the foundation for future Raman studies that aim to elucidate the structure of other CB[n] complexes in solid state environments when single crystal is not avaible or *in-situ* monitor a working CB[n] device.

5.4 Materials and Methods

5.4.1 General

CB7, CB7-Fc complex and corresponding NMR, IR, UV spectra are provided by Professor Galoppini at Rutgers University-Newark. ^{1}H-NMR (499.896 MHz) spectra were collected on a Varian IN0VA 500 NMR spectrometer at room temperature in D_2O. Chemical shifts were reported in ppm (δ) relative to the central line of the solvent (δ_{D2O}=4.82 ppm). Acetone, methanol (HPLC grade), ferrocene, glycoluril, formaldehyde (37% solution in water), α–cyano-4-hydroxy-cinnamic acid (CHCA) were used as received. Spectrophotometric grade solvents were used for the spectroscopic and spectrometric measurements. Attenuated Total Reflectance Infrared (FT-IR-ATR) spectra were recorded at room temperature on a Thermo Scientific Nicolet 6700 Spectrometer, with 100 numbers of scans and a resolution of 4 cm^{-1}. High resolution mass spectra (MALDI) were obtained on the departmental mass facility (Bruker Daltonics Apex-Qe series, Fourier Transform Mass Spectrometer) using CHCA as the matrix. The complex was mixed with a solution of the matrix in CH_2Cl_2/$CHCl_3$. The mixture was deposited on the plate and allowed to dry in the air at room temperature prior to the measurement. UV-Vis absorption spectra were acquired at ambient temperature on a Varian Cary-500 spectrophotometer.

5.4.2 Synthesis of Cucurbit[7]uril.

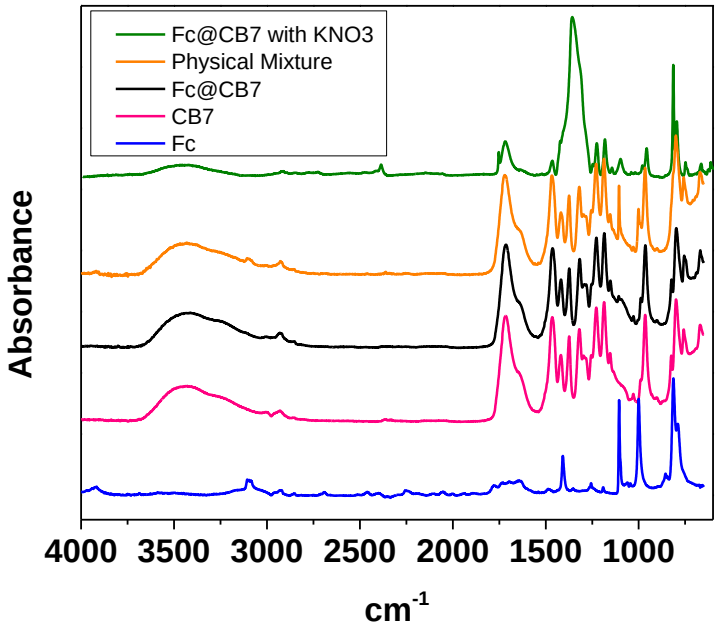

Figure 5.3 FTIR-ATR spectrum of Fc@CB7 compared with those of CB7, Fc, physical mixture of Fc and CB7 and Fc@CB7 mixed with KNO_3 (same sample used for Raman measurements, peak at 1370 attributed to NO_3 internal standard for Raman frequency calibration)

CB7 was synthesized following a procedure published by Nau and coworkers, [44] and separation of CB7 from the CB[n] homologues and the product purification were adapted from procedures described by Kim and coworkers.[41, 45] The pure product was dried under vacuum at 140 ^{o}C for 48 h. The spectral data were consistent with those reported in literature: [14, 41, 46-48] ^{1}H-NMR (D_2O): δ = 4.27-4.30 ppm (d, 14 H, J = 15.5, CH_2), 5.58 ppm (s, 14 H, CH), 5.82-5.85 ppm (d, J = 15.4, 14 H, CH_2); FT-IR-ATR: ~ 3432 (N-H), 2925 (C-H), 1721 (C=O), 1634 (C=C), 1468 (C-N), 1373, 1320, 1219, 1185, 965, 800 cm^{-1}, MALDI *m/z* calcd for $[(C_6H_6N_4O_2)_7 + Na]^+$: 1185.3327; found: 1185.3334. calcd for $[(C_6H_6N_4O_2)_7 + K]^+$: 1201.3067; found: 1201.3066.

5.4.3 Formation of Fc@CB7 Complex

The encapsulated ferrocene can be easily oxidized into ferrocenium[49] in acidic solutions as indicated by the appearance of the characteristic ferrocenium peak at 625 nm in the UV-vis spectrum (Figure 5.4). Therefore, in order to obtain the neutral complex, the aqueous CB7 (1 mM) solution was first adjust to pH 7 and then 3 mL aqueous solution of CB7 was transfered into a quartz cuvette charged with ferrocene (0.6 mg, 0.003 mmol). The mixture was degased by several freeze-pump-thaw cycles, then sonicated and stirred overnight. Figure 5.5 shows that the complex under neutrual pH is stable and there is no sign of ferrocenium formation after one and half weeks, unlike that of the complex obtained at pH<2 (Figure 5.5). The pH 7 solution was quickly transferred into a round bottom flask and water was removed by rotary evaporation. The resulting orange powder was collected and used for Raman measurements.

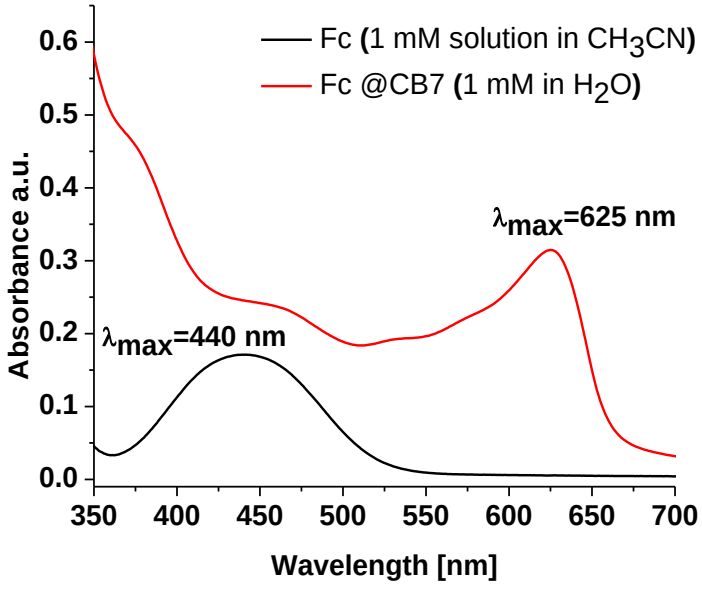

Figure 5.4 UV-Vis spectra of Fc and Fc@CB7 solutions in aerated conditions.

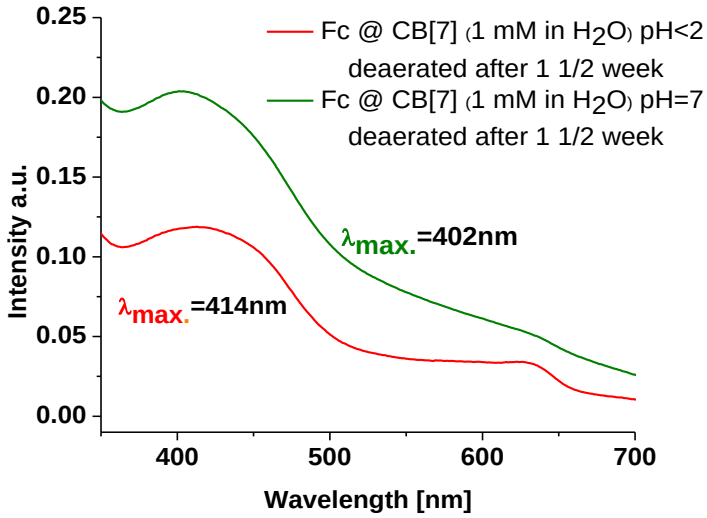

Figure 5.5 Solution UV-Vis spectra of Fc@CB7 complexes deaerated (pH<2 and pH 7) after 1 ½ week.

5.4.4 Raman Spectroscopy

Solid State CB7 and ferrocene samples were prepared Raman measurements by grinding with ~80 wt% KNO_3 as an internal frequency standard and then pressed into pellets. Raman spectra were collected using 785 nm diode laser (Innovative Photonic Solutions) excitation (~25 mW), a Trivista triple monochromator and a 1340 x 100 pixel Spec-10 liquid nitrogen-cooled CCD detector (Princeton Instruments). With 150 μm entrance slit width, the spectral resolution was < 5 cm^{-1}. Data were collected on spinning samples when possible to minimize photodecomposition or thermal damage. Due to a reduced amount of sample, The Fc@CB7 complex was pressed with KNO_3 in a smaller sample holder that did not allow spinning. However, no evidence of photodecomposition or thermal damage was detected upon laser irradiation throughout the experiment.

5.5 Reference

1 K. Kim, N. Selvapalam, Y. H. Ko, K. M. Park, D. Kim and J. Kim, *Chem. Soc. Rev.*, 2007, **36**, 267-279.

2 E. Masson, X. Ling, R. Joseph, L. Kyeremeh-Mensah and X. Lu, *RSC Advances*, 2012, **2**, 1213-1247.

3 J. W. Lee, S. Samal, N. Selvapalam, H.-J. Kim and K. Kim, *Acc. Chem. Res*., 2003, **36**, 621-630.

4 K. Kim, N. Selvapalam and D. H. Oh, *J. Incl. Phenom. Macro.*, 2004, **50**, 31-36.

5 D. Whang, J. Heo, J. H. Park and K. Kim, *Angew. Chem. Int. Ed.*, 1998, **37**, 78-80.

6 X. X. Zhang, K. E. Krakowiak, G. Xue, J. S. Bradshaw and R. M. Izatt, *Ind. Eng. Chem. Res.*, 2000, **39**, 3516-3520.

7 W. Ong and A. E. Kaifer, *J. Org. Chem.*, 2004, **69**, 1383-1385.

8 H. Tang, D. Fuentealba, Y. H. Ko, N. Selvapalam, K. Kim and C. Bohne, *J. Am. Chem. Soc.*, 2011, **133**, 20623-20633.

9 M. V. Rekharsky and Y. Inoue, *Chem. Rev.*, 1998, **98**, 1875-1918.

10 M. V. Rekharsky, T. Mori, C. Yang, Y. H. Ko, N. Selvapalam, H. Kim, D. Sobransingh, A. E. Kaifer, S. Liu, L. Isaacs, W. Chen, S. Moghaddam, M. K. Gilson, K. Kim and Y. Inoue, *PNAS*, 2007, **104**, 20737-20742.

11 T. V. Mitkina, M. N. Sokolov, D. Y. Naumov, N. V. Kuratieva, O. A. Gerasko and V. P. Fedin, *Inorg. Chem.*, 2006, **45**, 6950-6955.

12 T. V. Mitkina, N. F. Zakharchuk, D. Y. Naumov, O. A. Gerasko, D. Fenske and V. P. Fedin, *Inorg. Chem.*, 2008, **47**, 6748-6755.

13 W. S. Jeon, K. Moon, S. H. Park, H. Chun, Y. H. Ko, J. Y. Lee, E. S. Lee, S. Samal, N. Selvapalam, M. V. Rekharsky, V. Sindelar, D. Sobransingh, Y. Inoue, A. E. Kaifer and K. Kim, *J. Am. Chem. Soc.*, 2005, **127**, 12984-12989.

14 M. Freitag, E. Galoppini, *Langmuir*, 2010, **26**, 8262-8269.

15 M. Freitag and E. Galoppini, *Eng. Eviron. Sci.*, 2011, **4**, 2482-2494.

16 M. Porel, A. Klimczak, M. Freitag, E. Galoppini and V. Ramamurthy, *Langmuir*, 2012, **28**, 3355-3359.

17 N. i. Saleh, A. Khaleel, H. Al-Dmour, B. al-Hindawi and E. Yakushenko, *J. Therm. Anal. Calorim.*, 2012, 1-8.

18 S. H. Kim, D. Debnath and K. E. Geckeler, *Supramol. Chem.*, 2011, **23**, 337-341.

19 Y. Huang, S.-F. Xue, Z. Tao, Q.-J. Zhu, H. Zhang, J.-X. Lin and D.-H. Yu, *J. Incl. Phenom. Macro.*, 2008, **61**, 171-177.

20 P. K. Dutta and M. A. Thompson, *Chem. Phys. Lett.*, 1986, **131**, 435-437.

21 C. Zhang, P. M. Allotta, G. Xiong and P. C. Stair, *J. Phys. Chem. C*, 2008, **112**, 14501-14507.

22 J. G. Mesu, T. Visser, A. M. Beale, F. Soulimani and B. M. Weckhuysen, *Chem. Eur. J.*, 2006, **12**, 7167-7177.

23 S.-K. Joung, T. Okazaki, S. Okada and S. Iijima, **Phys. Status. Solidi. B**, 2010, **247**, 2700-2702.

24 W. Plank, H. Kuzmany, R. Pfeiffer, T. Saito and S. Iijima, **Phys. Status. Solidi. B**, 2009, **246**, 2724-2727.

25 J. E. D. Davies, *J. Chem. Soc., Dalton Trans.*, 1972, 1182-1188.

26 H. Ohno, M. Kida, T. Sakurai, Y. Iizuka, T. Hondoh, H. Narita and J. Nagao, *ChemPhysChem*, 2010, **11**, 3070-3073.

27 E. H. Witlicki, S. W. Hansen, M. Christensen, T. S. Hansen, S. D. Nygaard, J. O. Jeppesen, E. W. Wong, L. Jensen and A. H. Flood, *J. Phys. Chem. A*, 2009, **113**, 9450-9457.

28 W. Li, B. Lu, F. Chen, F. Yang and Z. Wang, *J. Mol. Struct.*, 2011, **990**, 244-252.

29 J. Marques, L. Anjo, M. P. M. Marques, T. M. Santos, F. A. Almeida Paz and S. S. Braga, *J. Organomet. Chem.*, 2008, **693**, 3021-3028.

30 Y. Pellegrin, R. J. Forster and T. E. Keyes, *Inorg. Chim. Acta*, 2008, **361**, 2683-2691.

31 H. M. Heise, R. Kuckuk, A. Bereck and D. Riegel, *Vib. Spectrosc.*, 2010, **53**, 19-23.

32 S. Mahajan, T.-C. Lee, F. Biedermann, J. T. Hugall, J. J. Baumberg and O. A. Scherman, *Phys. Chem. Chem. Phys.*, 2010, **12**, 10429-10433.

33 C.-A. Tao, Q. An, W. Zhu, H. Yang, W. Li, C. Lin, D. Xu and G. Li, *Chem. Comm.*, 2011, **47**, 9867-9869.

34 M. L. Roldan, S. Sanchez-Cortes, J. V. Garcia-Ramos and C. Domingo, *Phys. Chem. Chem. Phys.*, 2012, **14**, 4935-4941.

35 R. W. Taylor, T.-C. Lee, O. A. Scherman, R. Esteban, J. Aizpurua, F. M. Huang, J. J. Baumberg and S. Mahajan, *ACS Nano*, 2011, **5**, 3878-3887.

36 J. S. Bodenheimer and W. Low, *Spectrochim. Acta A*, 1973, **29**, 1733-1743.

37 E. Diana, R. Rossetti, P. L. Stanghellini and S. F. A. Kettle, *Inorg. Chem.*, 1997, **36**, 382-391.

38 S. Yi, B. Captain and A. E. Kaifer, *Chem. Comm.*, 2011, **47**, 5500-5502.

39 S. Liu, C. Ruspic, P. Mukhopadhyay, S. Chakrabarti, P. Y. Zavalij and L. Isaacs, *J. Am. Chem. Soc.*, 2005, **127**, 15959-15967.

40 W. Ong and A. E. Kaifer, *Organometallics*, 2003, **22**, 4181-4183.

41 J. Kim, I.-S. Jung, S.-Y. Kim, E. Lee, J.-K. Kang, S. Sakamoto, K. Yamaguchi and K. Kim, *J. Am. Chem. Soc.*, 2000, **122**, 540-541.

42 I. S. Butler, P. D. Harvey and G. C. Allen, *J. Ram. Spec.*, 1987, **18**, 1-7.

43 J. Brunvoll, S. J. Cyvin and L. Schäfer, *J. Organomet. Chem.*, 1971, **27**, 107-111.

44 C. Marquez, F. Huang, W. M. Nau, *IEEE T.NANOBIOSI.*, 2004, **3**, 39-45.

45 J. Zhao, H.-J. Kim, J. Oh, S.-Y. Kim, J. W. Lee, S. Sakamoto, K. Yamaguchi, K. Kim, *Angew. Chem. Int. Ed,*. 2001, **113**, 4363-4365.

46 J. P. Silva, N. Jayaraj, S. Jockusch, N. Turro, V. Ramamurthy, *Org.Lett.*, 2011, **13**, 2410-2413.

47 U. Pischel, V. D. Uzunova, P. Remon, W. R. Nau, *Chem. Commun.* , 2010, **46**, 2635-2637.

48 C. P. Carvalho, V. D. Uzunova, J. P. Silva, W. M. Nau, U. Pischel, *Chem. Commun.*, 2011, **47**, 8793-8795.

49 W. Ong, A. E. Kaifer, *Organometallics*, 2003, **22**, 4181-4183

CONCLUSION

In this dissertation, Raman spectroscopy and XAS are used to investigate the structural change and host-guest interaction in three kinds of MOF materials and one supramolecular complex. We first validated our methodology in Chapter 2 by monitoring the activation process of a flexible framework-CoHoba. The results show that these methods are useful complementary techniques to reveal local structural changes in coordination complex when XRD fall short to provide detailed information. In terms of the materials, these studies also revealed large structure changes that may have implications regarding the accessibility of the metal sites for further catalytic reactions. Then in Chapter 3, we applied *in-situ* Raman spectroscopy and XAS to obtain a more complete picture of the structural changes during activation process and the host-guest interaction in a dual functionalized framework-CuTDPAT. This work provides evidences about the interaction between both binding sites in this framework and also reveals that the structural differences between activated and hydrated CuTDPAT may have considerable impact on the adsorption behavior. In Chapter 4, rather than investigate individual frameworks, we start to look for a pattern in the structure-property relationship. In this chapter, the activation and gas adsorption process of four iso-structural frameworks are studied by *in-situ* Raman spectroscopy and diffuse reflectance UV-vis. The results show that in frameworks with the same ligand and structure, different metal centers behave differently upon activation and eventually lead to distinguishable gas uptakes. XAS and computational studies are planned to further elucidate the relationship between metal coordination geometry changes and gas adsorption property. Although the limited amount of works in this dissertation can not give a direct guidance for MOF

design and synthesis, further investigation of other MOF systems can reveal more patterns in the structure-property relationship and eventually provide enough information for rational design of MOFs.

We also attempted to utilize some of the same spectroscopy techiques to study systems other than MOFs that involve host-guest interactions. The complexation between cucurbit[7]uril and ferrocene is investigated by Raman spectroscopy in Chapter 5. The result shows that Raman spectroscopy can provide molecular level structural information of CB7-ferrocene complex. Since Raman spectroscopy can be conveniently applied on samples in most formats, especially solid state environments, it may become quite useful when studying supramolecular devices *ex-situ* or *in-situ*.